Micromagnetic investigation of MnAs thin films on GaAs surfaces

DISSERTATION

zur Erlangung des akademischen Grades
doctor rerum naturalium
(Dr. rer. nat.)
im Fach Physik

eingereicht an der
Mathematisch-Naturwissenschaftlichen Fakultät I
Humboldt-Universität zu Berlin

von
Herr M.Tech. M.Sc. Jyoti Ranjan Mohanty
geboren am 20.03.1976 in Tirtol, Indien

Präsident der Humboldt-Universität zu Berlin:
Prof. Dr. Jürgen Mlynek

Dekan der Mathematisch-Naturwissenschaftlichen Fakultät I:
Prof. Thomas Buckhout, Ph.D.

Gutachter:

1. Prof. Dr. K. H. Ploog
2. Prof. Dr. T. Masselink
3. Prof. Dr. K. R. A. Ziebeck

eingereicht am: 18.03.2005
Tag der mündlichen Prüfung: 15.06.2005

Abstract

This work presents the study of the micromagnetic domain structure and the coupled magneto-structural phase transition of MnAs thin films on GaAs. In particular, the influence of substrate orientation, film thickness and external magnetic field on the magnetic and structural properties are investigated, employing the complementary measurement techniques atomic force microscopy-AFM / magnetic force microscopy-MFM and low energy electron microscopy-LEEM / X-ray magnetic circular dichroism photoemission electron microscopy-XMCDPEEM for the characterization of the structural / micromagnetic properties of the materials system.

MnAs exhibits a first-order phase transition from the hexagonal, ferromagnetic α-phase to the orthorhombic, paramagnetic β-phase at around 40 °C. In epitaxial MnAs films on GaAs, it is known that the ferromagnetic and the paramagnetic phases coexist over a wide temperature range of about 30 °C below the phase transition temperature. In this temperature range, MnAs films on GaAs (001) and (311)A substrates show a regular array of ferromagnetic stripes due to the involved strain. The width of the ferromagnetic stripes can be tuned by varying the temperature, whereas the periodicity of the stripe pattern is found to be a linear function of film thickness. The in part complex micromagnetic domain structure strongly depends on the width and the distance of the ferromagnetic stripes, as it directly affects the shape anisotropy and magnetic coupling, respectively. The films exhibit a strong uniaxial magnetic anisotropy, where the magnetic easy axis is the a-axis (along MnAs $[11\bar{2}0]$) and the magnetic hard axis is the c-axis (along MnAs [0001]) and both axes lie in the film plane.

For MnAs films grown on GaAs (111)B, the c-axis is normal to the surface and the $[\bar{2}110]$ and $[01\bar{1}0]$ directions of MnAs are parallel to the $[\bar{1}10]$ and $[11\bar{2}]$ directions of GaAs, respectively. The epitaxy also leads to a different strain state of the film and a higher phase transition temperature of roughly 56 °C compared to films grown on GaAs (001) and (311)A. Over a large temperature range of more than 30 °C below the phase transition temperature the α- and β-phase coexist, however, now forming polygonal ferromagnetic structures embedded in a honeycomb-like paramagnetic network.

Based on the observation of the micromagnetic domain structure of MnAs films on GaAs (001), a classification of the domain patterns was carried. Depending on the number of subdomains along the easy *a*-axis direction on a ferromagnetic stripe, up to three basic domain types can be distinguished. More complicated domain patterns are explained by the respective combinations of the three basic domain types. The measured MFM contrast is simulated based on this domain classification scheme and a good agreement was found. Moreover, XMCDPEEM measurements are able to confirm the domain classification scheme that was initially derived from MFM observations.

As the employed micromagnetic imaging techniques have a different information depth, it is possible to gain information about the domain structure in the vertical direction as well. Whereas MFM and XMCDPEEM results agree well for thinner films (< 300 nm), the observation of thicker films leads to a discrepancy of the deduced domain patterns. The apparent differences are explained by the assumption of domains in the vertical direction that reflect themselves in the MFM images, but not in the XMCDPEEM images.

MnAs films exhibit a delicate strain balance that directly affects their magnetic and structural properties. By using wet-etching techniques, α-MnAs and β-MnAs show different etch rates. Selective removal of Mn atoms from the MnAs layer destroys the strain balance of the film, which results in the formation of regularly spaced cracks running along the *c*-axis direction. Further etching leads to the formation of 2-dimensional arrays of islands. Using temperature-dependent AFM, MFM and XMCDPEEM, it is shown that the local strain relaxation in the vicinity of the cracks results in a locally increased phase transition temperature.

In order to study magnetization reversal processes on a microscopic scale, as well as the influence of the magnetic field on the micromagnetic domain structure, a variable-magnetic field set-up is added to the existing variable-temperature scanning probe microscope. By field-dependent MFM measurements, the magnetization curve is measured microscopically and a good agreement is found with integral SQUID magnetometry measurements. Furthermore, by varying the temperature in an external magnetic field a deeper insight into the coupled structural and magnetic phase transition in MnAs films is gained, as the coupling between the ferromagnetic stripes can be tuned. It was found that the ferromagnetic order is extended to higher temperatures by applying an external magnetic field.

Zusammenfassung

Die vorliegende Arbeit befaßt sich mit der Untersuchung der mikromagnetischen Domänenstruktur und des gekoppelten magneto-strukturellen Phasenübergangs dünner MnAs-Filme auf GaAs. Im Besonderen wurde der Einfluß der Substratorientierung, der Filmdicke und eines externen magnetischen Feldes auf die magnetischen und strukturellen Eigenschaften untersucht. Dabei kamen die komplementären Untersuchungsmethoden AFM (atomic force microscopy) / MFM (magnetic force microscopy) und LEEM (low energy electron microscopy) / XMCDPEEM (X-ray magnetic circular dichroism photoemission electron microscopy) für die Charakterisierung der strukturellen / mikromagnetischen Eigenschaften des Materialsystems zum Einsatz.

MnAs zeigt einen Phasenübergang erster Ordnung von der hexagonalen, ferromagnetischen α-Phase in die orthorhombische, paramagnetische β-Phase bei etwa 40 °C. Es ist bekannt, daß die ferromagnetische und die paramagnetische Phase in epitaktischen MnAs Filmen auf GaAs über einen großen Temperaturbereich von etwa 30 °C unterhalb der Phasenübergangstemperatur hinweg koexistieren. In diesem Temperaturbereich zeigen MnAs-Filme auf GaAs (001) und (311)A Substraten eine regelmäßige Anordnung von ferromagnetischen Streifen aufgrund der involvierten Verspannung. Die Breite der ferromagnetischen Streifen kann durch Variation der Temperatur eingestellt werden, wobei die Periodizität des Streifenmusters eine lineare Funktion der Filmdicke ist. Die zum Teil komplexe mikromagnetische Domänenstruktur hängt stark von der Breite bzw. dem Abstand der ferromagnetischen Streifen ab, da diese direkt die Formanisotropie bzw. die magnetische Kopplung beeinflussen. Der Film zeigt eine ausgeprägte einachsige magnetische Anisotropie, bei der die magnetische leichte Richtung die a-Achse (entlang MnAs $[11\bar{2}0]$) und die harte magnetische Richtung die c-Achse (entlang MnAs [0001]) ist; beide Achsen liegen in der Filmebene.

Bei MnAs-Filmen die auf der GaAs (111)B Oberfläche gewachsen wurden, ist die c-Achse parallel zur Wachstumsrichtung und die $[\bar{2}110]$ bzw. $[01\bar{1}0]$ Richtung von MnAs parallel zur $[\bar{1}10]$ bzw. $[11\bar{2}]$ Richtung von GaAs. Die Epitaxie führt ferner zu einem geänderten Spannungszustands des Films und einer erhöhten Phasenübergangstemperatur von 56 °C verglichen mit MnAs-Filmen auf GaAs (001) und (311)A. Über einen großen Temperaturbereich von über 30 °C unterhalb der Phasenübergangstemperatur hinweg koexistieren die α- und die β-Phase. Es bilden sich dabei polygonale ferromagnetische

Strukturen, die in einer wabenartigen paramagnetischen Matrix eingebettet sind.

Eine Klassifizierung der Domänenstrukturen wurde, beruhend auf den beobachteten mikromagnetischen Strukturen von MnAs-Filmen auf GaAs (001), durchgeführt. Abhängig von der Zahl der Subdomänen entlang der leichten a-Achse auf einem ferromagnetischen Streifen können bis zu drei elementare Domänentypen beobachtet werden. Kompliziertere Domänenstrukturen lassen sich durch eine Kombination der drei elementaren Domänentypen erklären. Der gemessene MFM-Kontrast ist auf der Basis der Domänenklassifizierung simuliert worden und es ist eine gute Übereinstimmung gefunden worden. Darüber hinaus konnte durch XMCDPEEM-Messungen das Domänenklassifizierungsschema, das auf MFM-Messungen zurückgeht, verifiziert werden.

Da die eingesetzten mikromagnetischen Untersuchungstechniken unterschiedliche Informationstiefen aufweisen, ist es auch möglich Rückschlüsse auf die Domänenstruktur in der vertikalen Richtung zu ziehen. Für dünnere Filme ($<$ 300 nm) stimmen die Ergebnisse der XMCDPEEM- und MFM-Messungen gut überein, wobei Abweichungen bei dickeren Filmen beobachtet werden. Die Abweichungen werden dadurch erklärt, daß eine vertikale Domänenstruktur angenommen wird, die sich im MFM-Kontrast, nicht aber im XMCDPEEM-Kontrast zeigt.

MnAs-Filme sind in einen mechanischen Spannungszustand, der ihre magnetischen und strukturellen Eigenschaften beeinflußt. Durch die Anwendung von naßchemischen Ätzverfahren lassen sich die beiden MnAs-Phasen mit einer unterschiedlichen Rate ätzen. Die selektive Entfernung von Mn-Atomen aus dem MnAs-Film zerstört den Spannungszustand des Films, wobei sich Risse bilden, die entlang der c-Achse ausgerichtet sind und die einen wohldefinierten Abstand zueinander aufweisen. Weiteres Ätzen führt zur Bildung einer zweidimensionalen Anordnung von Inseln. Durch temperaturabhängige XMCDPEEM-, AFM- und MFM-Messungen kann gezeigt werden, daß durch den lokalen Abbau der Verspannung in der Nähe eines Risses die Phasenübergangstemperatur lokal erhöht ist.

Um Ummagnetisierungsprozesse auf einer mikroskopischen Skala untersuchen zu können und um den Einfluß eines magnetischen Feldes auf die mikromagnetische Domänenstruktur sichtbar machen zu können, wurde das temperaturvariable Rastersondenmikroskop um einen variablen Magnetfeldaufbau ergänzt. Magnetfeldabhängige MFM-Messungen erlauben die mikroskopische Messung von Magnetisierungskurven von MnAs, wobei eine gute Übereinstimmung mit integralen SQUID-Magnetometriemessungen gefunden wurde. Zudem erlaubt die Variation der Temperatur bei angelegtem Magnetfeld einen Einblick in den gekoppelten strukturellen und magnetischen Phasenübergang von MnAs-Filmen, da die Kopplung zwischen den ferromagnetischen Streifen gezielt eingestellt werden kann. Ferner wurde gefunden, daß in einem angelegten Magnetfeld die ferromagnetische Ordnung zu höheren Temperaturen hin ausgedehnt wird.

Parts of this work have already been published

T. Plake, T. Hesjedal, **J. Mohanty**, M. Kästner, L. Däweritz, and K.H. Ploog, *Temperature-dependent magnetic force microscopy investigation of epitaxial MnAs films on GaAs (001)*, Appl. Phys. Lett. **82**, 2308-2310 (2003).

J. Mohanty, T. Hesjedal, T. Plake, M. Kästner, L. Däweritz, and K. H. Ploog, *Variable-temperature micromagnetic study of epitaxially grown MnAs films on GaAs (001)*, Appl. Phys. A **77**, 739-742 (2003).

J. Mohanty, T. Hesjedal, Y. Takagaki, R. Koch, L. Däweritz, and K. H. Ploog, *Effect of strain on the local phase transition temperature of MnAs/GaAs*, Appl. Phys. Lett. **83**, 2829-2831 (2003).

A. Ney, T. Hesjedal, C. Pampuch, **J. Mohanty**, A. K. Das, L. Däweritz, R. Koch, and K. H. Ploog, *Magnetic out-of-plane component in MnAs/GaAs (001)*, Appl. Phys. Lett. **83**, 2850-2852 (2003).

R. Engel-Herbert, **J. Mohanty**, A. Ney, T. Hesjedal, L. Däweritz, and K. H. Ploog, *Understanding the submicron domain structure of MnAs thin films on GaAs(001): Magnetic force microscopy measurements and simulations*, Appl. Phys. Lett. **84**, 1132 (2004).

Y. Takagaki, E. Wiebicke, **J. Mohanty**, T. Hesjedal, L. Däweritz, and K. H. Ploog, *Semiautomatic wet chemical etching of an array of MnAs nanodots and their magnetic properties*, Physica E **24**, 115 (2004).

L. Däweritz, L. Wan, B. Jenichen, C. Herrmann, **J. Mohanty**, A. Trampert and K. H. Ploog, *Thickness dependence of the magnetic properties of MnAs films on GaAs (001) and GaAs (311)A: Role of a natural array of ferromagnetic stripes*, J. Appl. Phys. **96**, 5056 (2004).

Submitted for publication

R. Engel-Herbert, **J. Mohanty**, A. Ney, T. Hesjedal, B. Jenichen, R. Koch, L. Däweritz, K. H. Ploog, E. Bauer, S. Cherifi, R. Belkhou, S. Heun and A. Locatelli, *Unusual magnetic domain walls in MnAs thin films*, submitted to Phys. Rev. B

J. Mohanty, R. Engel-Herbert and T. Hesjedal, *Variable field and temperature magnetic force microscopy*, submitted to Appl. Phys. A

J. Mohanty, Y. Takagaki and T. Hesjedal, L. Däweritz and K. H. Ploog, *Selective etching of epitaxial MnAs films on GaAs (001): Influence of structure and strain*, submitted to J. Appl. Phys.

Conference Contributions

J. Mohanty, T. Hesjedal, M. Kästner, L. Däweritz, and K. H. Ploog, *Temperature dependent magnetic force microscopy of epitaxial MnAs on GaAs (001)*, Poster: National Conference on Nanostructured Materials, IIT, Delhi, India, December 5-6, 2002.

L. Wan, B. Jenichen, C. Herrmann, **J. Mohanty**, L. Däweritz, and K. H. Ploog, *Comparative study of ferromagnetic MnAs films on GaAs (001) and (113) A*, Poster: Spintech-II, April 4-8, 2003.

L. Däweritz, L. Wan, B. Jenichen, C. Herrmann, **J. Mohanty**, and K. H. Ploog, *Tailoring of the structure and magnetic properties of α-MnAs spin injection layer on GaAs (001)*, Inst. Phys. Conf. Ser. No. 184, pp. 149-152, 2005.

J. Mohanty, R. Engel-Herbert, T. Hesjedal, L. Däweritz, K. H. Ploog, S. Cherifi, S. Heun, A. Locatelli and E. Bauer, *Micromagnetic properties of epitaxial MnAs films on GaAs: An in-depth investigation using MFM and XMCDPEEM*, Poster: 338th WEH seminar, Nanomagnetism: New Insights with Synchrotron Radiation, Bad Honnef, January 5-7, 2005.

L. Däweritz, C. Herrmann, **J. Mohanty**, T. Hesjedal, K. H. Ploog, E. Bauer, S. Cherifi, A. Pavlovska, R. Belkhou, S. Heun, A. Locatelli, *Tailoring of the structure and magnetic properties of MnAs films grown on GaAs*, 32nd Conference on the Physics and Chemistry of Semiconductor Interfaces, Montana, USA, January 5-7, 2005.

J. Mohanty, T. Hesjedal, L. Däweritz, K. H. Ploog, *Micromagnetic properties of MnAs films on GaAs (001) studied by variable temperature and field MFM*, Poster: 69. Jahrestagung der Deutschen Physikalischen Gesellschaft, Berlin, March 4-9, 2005.

J. Mohanty, T. Hesjedal, L. Däweritz, K. H. Ploog, S. Cherifi, S. Heun, A. Locatelli, E. Bauer, *Domain structures and their dynamics in MnAs films studied by XMCDPEEM and LEEM*, Talk: 69. Jahrestagung der Deutschen Physikalischen Gesellschaft, Berlin, March 4-9, 2005.

R. Engel-Herbert, **J. Mohanty**, T. Hesjedal, *Simulation of magnetic force microscopy of MnAs/GaAs (001)*, Poster: 69. Jahrestagung der Deutschen Physikalischen Gesellschaft, Berlin, March 4-9, 2005.

List of Acronyms

AFM	atomic force microscopy
MFM	magnetic force microscopy
VT-MFM	variable-temperature magnetic force microscopy
SQUID	superconducting quantum interference device
XMCD	X-ray magnetic circular dichroism
PEEM	photoemission electron microscopy
XMCDPEEM	X-ray magnetic circular dichroism photoemission electron microscopy
XRD	X-ray diffraction
TEM	transmission electron microscopy
HRTEM	high-resolution transmission electron microscopy
CBM	cantilever beam magnetometry
MBE	molecular beam epitaxy
SEM	scanning electron microscopy
SFM	scanning force microscopy
FMR	ferromagnetic resonance
C/NC	contact mode/ non-contact mode
LEEM	low energy electron microscopy
LEED	low energy electron diffraction
STM	scanning tunneling microscopy

Contents

List of Figures

List of Tables

Chapter 1

Introduction

The rapid progress in the miniaturization of semiconductor electronic devices leads towards features smaller than 100 nanometers in size. The remarkable developments in the field of electronics and information technology have been made possible by exploiting the charge of the electron. New concepts envision the use of both the charge and the spin state of the electron, giving birth to the new field of spin electronics (or spintronics) [Pri90]. Integrated circuits for data processing make use of the charge of the electron in semiconductors, while data storage media, such as hard disks, make use of the spin property of the electron in magnetic materials. The advantages of magnetic logic devices would be non-volatility, increased data processing speed, decreased electric power consumption, and increased integration densities compared to semiconductor devices. Historically, the search for magnetic semiconductors was motivated by the perspective to incorporate magnetic functions into semiconductors [Pri90, Pri95, Tan02].

For the realization of spintronics devices efficient sources for spin-polarized electrons have to be developed. The combination of a III-V semiconductor like GaAs and a ferromagnetic metal like MnAs is a promising material system showing potential for spin injection [RHK$^+$02], as well as magneto-logic applications [PDN$^+$03, NPKP03]. Epitaxial MnAs films of high quality can be grown by molecular beam epitaxy (MBE) on GaAs [STDP99, THP$^+$94, STD$^+$99, STDP00]. MnAs shows a first-order phase transition from the ferromagnetic, hexagonal α-phase to the paramagnetic, orthorhombic β-phase at about 40 °C. In epitaxial MnAs films, due to the involved strain, both phases coexist over a wide temperature range (10-40 °C) [DSK$^+$02, KJS$^+$00, KJS$^+$02, PRK$^+$02].

MnAs films on GaAs (001) and (311)A are known to exhibit a well-ordered periodic α-β-stripe structure, which resembles a naturally structured uniaxial magnetic system. In this system, the ferromagnetic stripe width can be tuned by the temperature and the stripe period is determined by the film thickness. As the ferromagnetic stripe width directly alters the magnetic properties of the wires via the shape anisotropy, a detailed study of the domain statistics as a function of temperature and film thickness will be presented. For this purpose, a domain classification scheme was developed. Contrary to MnAs on GaAs (001) and (311)A, MnAs on GaAs (111)B shows surprisingly different magnetic and structural properties. Among them is an enhanced phase transition temperature which will be presented in this work.

Due to the first-order nature of the coupled magneto-structural phase transition of MnAs on GaAs, it is possible to shift the phase transition temperature by, e.g., applying external pressure [GK69]. By structurally modifying the thin films, strain was locally relieved. The effect on the local phase transition temperature is made visible by micromagnetic imaging techniques.

The micromagnetic characterization is at the heart of efforts to systematically develop and characterize magnetoelectronic materials and devices. An ideal magnetic imaging technique should allow high-resolution imaging, both laterally and as a function of depth, fast imaging to follow magnetization dynamics, imaging in an external field environment, imaging magnetic devices where magnetic structures are buried under non-magnetic overlayers and imaging without disturbing the magnetic structure. Magnetic force microscopy (MFM), a technique sensitive to the out-of-plane component of the magnetic stray field, is used as a standard method to image the magnetic domain structure with sub-μm resolution [MW87]. In this work, surface-sensitive and element-sensitive X-ray magnetic circular dichroism photoemission electron microscopy (XMCDPEEM), together with low energy electron microscopy (LEEM) [SHS$^+$98], serve as complementary techniques to atomic force microscopy (AFM) and MFM.

The thesis is organized as follows: first, a brief introduction to the material system is given (Chapter 2) and the employed measurement techniques are described (Chapter 3). Chapter 4 deals with the magnetic domain structures, the MFM contrast formation, and the influence of the film thickness and substrate orientation on the magnetic properties of the film. Details about the first-order magneto-structural phase transition are discussed in Chapter 5. Chapter 6 presents the investigation of the influence of an external magnetic field on the magnetic domain structure. Nucleation and growth of domains are also discussed in this Chapter. Finally, possible patterning techniques for MnAs films are presented in Chapter 7 and a brief summary of this work is given in Chapter 8.

Chapter 2

The Material System MnAs-on-GaAs

MnAs-on-GaAs is an interesting hybrid material system as it combines ferromagnetic and semiconducting properties. MnAs, as a bulk material, was studied extensively in the 1960's [Gui51, BR62, WK64, WR54]. Recently, MnAs thin films were grown on standard semiconductors like GaAs and Si using molecular beam epitaxy (MBE) [ATUN95, THP$^+$94, STDP99]. In this Chapter, a brief overview of the material system starting from the bulk properties to the thin films will presented.

2.1 Structural and magnetic properties

Below 40 °C, bulk MnAs shows a hexagonal NiAs structure ($B8_1$) which is ferromagnetic (α-MnAs). Above 40 °C, MnAs undergoes a magneto-structural phase transition with a volume change of $\approx$ 2% to a distorted orthorhombic MnP-type structure (B31) which is paramagnetic (β-MnAs) [Gui51, BR62, WK64, WR54]. The first-order nature of the phase transition is characterized by an abrupt change in the order parameter, e.g. magnetization (shown in Fig. 2.1), as a function of temperature. Furthermore, the discontinuous change of the lattice parameters [WR54], the appearance of latent heat and the temperature hysteresis [BR63] at the transition holds a strong point for the first-order nature of the phase transition in MnAs. Above a temperature of 125 °C, the orthorhombic distortion relaxes and the material undergoes a second-order phase transition (purely structural) which reverts back to its hexagonal structure as before, however, now showing paramagnetic properties (γ-phase).

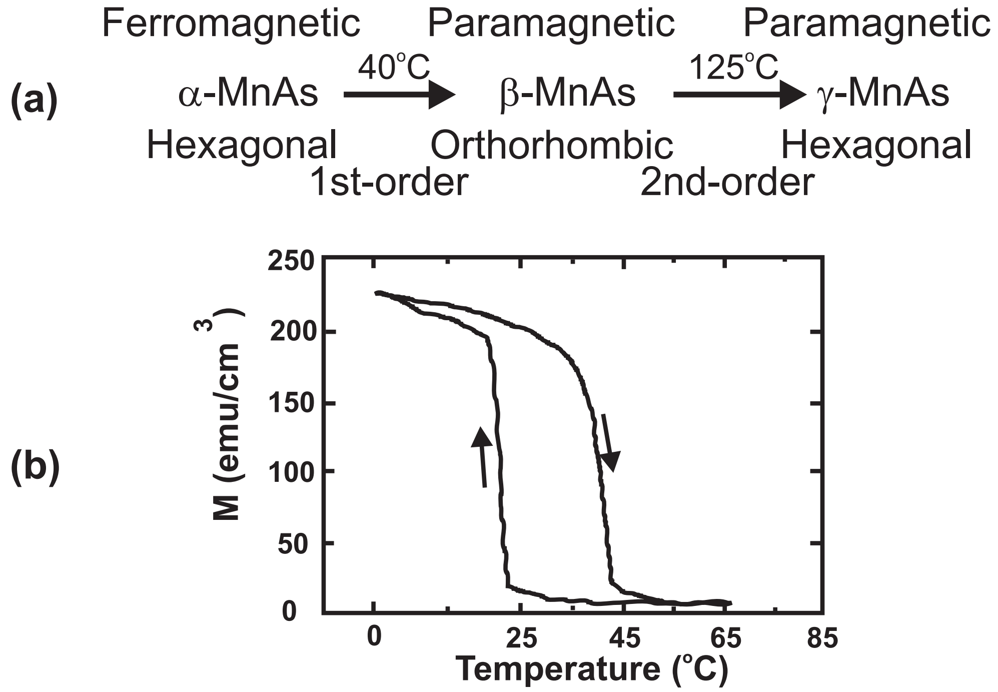

Figure 2.1: (a) Overview of the MnAs phases and crystal structure as a function of temperature. (b) Variation of the magnetization as a function of temperature for increasing and decreasing temperatures. The magnetization drops suddenly at about 40 °C following the first-order phase transition [CWMS99].

2.2 Phase coexistence

Compared to the bulk, MnAs thin films grown on GaAs substrates exhibit altered physical properties. A major difference is the continuous transition of the film from the α-phase to the β-phase over a wide temperature range of 10–40 °C. At first sight, this seems to be a violation of Gibbs's phase rule. However, this continuous transition is the result of the strain-stabilized coexistence of both phases in the defined temperature range [DSK+02, KJS+00, KJS+02, PRK+02].

The thermal expansion mismatch (as shown in Tab. 2.1) and the lattice mismatch of the MnAs–GaAs system is different along the crystallographic directions. The lattice mismatch along the c-axis of the hetero-epitaxial system was reduced from its initial value to 5% by the coincidence plane matching [TSDP01, Tra02, TSDP99]. The tightly bonded film/substrate geometry imposes strain on the film. This is due to the hinderance in the expansion or contraction as a result of the volume change in the course of the phase transition. The strain is relieved by forming a periodic stripe structure of the two different MnAs-phases. The resulting modulation of the topography of the α-β-stripe structure is about 1.7% (studied by AFM, cf. Fig. 2.2) and compares well with the 1.9% calculated for bulk MnAs [GSEFW70]. The alternating stripes are orientated along the c-axis direction. Hence, the strain along the a-axis has been relaxed, however, the smaller residual strain along the c-axis remains intact. The in-plane a- and c-axes are known to be the magnetic easy and hard axis of MnAs, respectively, as measured by superconducting quantum interference device (SQUID) magnetometry (Sect. 3.2.1)[1].

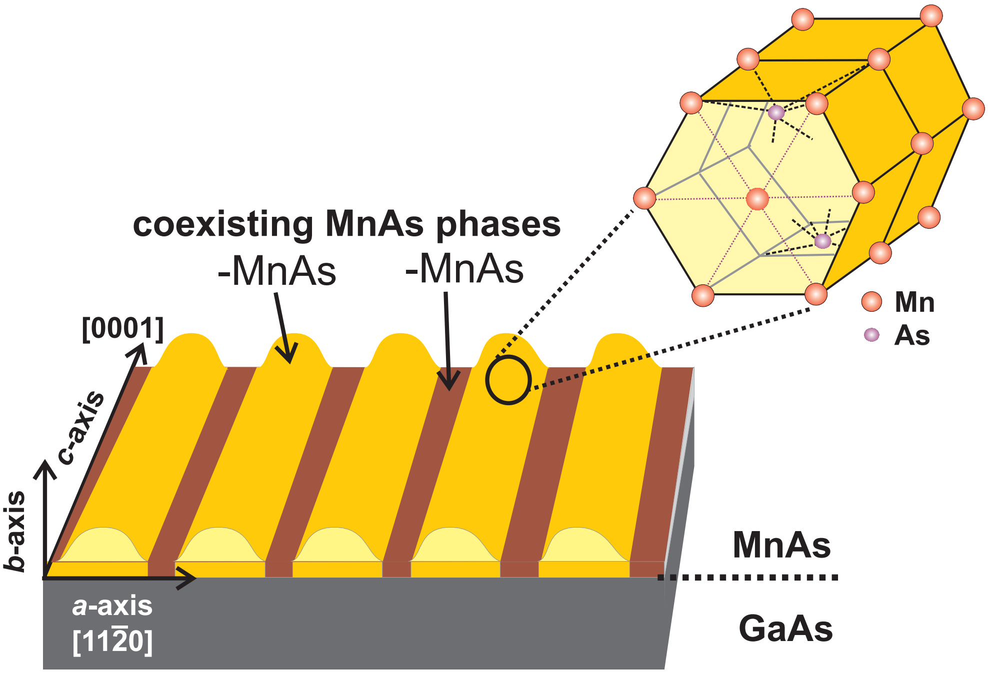

Figure 2.2: Sketch shows MnAs coexisting α- and β-phases. Top right of the sketch shows MnAs hexagonal planes with Mn and As atom and their bonding configuration.

---

[1] In hexagonal magnetic system the c-axis is usually the magnetic easy axis e.g. Co. In MnAs bulk crystals, the hexagonal plane is the easy plane of magnetization, whereas in MnAs films this degeneracy is lifted and the in-plane a-axis becomes the easy axis of magnetization.

Table 2.1: Linear thermal expansion coefficients κ [in $(^\circ\mathrm{C})^{-1}$] of the MnAs–GaAs system [DPN+03].

MnAs	GaAs
[along a-axis] α-MnAs = -1.1×10^{-4} β-MnAs = 6.3×10^{-5} **[along c-axis]** $\alpha(\beta)$-MnAs = 2.8×10^{-5}	6.0×10^{-6}

2.3 Epitaxial growth of MnAs on GaAs

MnAs thin films were grown on GaAs substrates using solid source MBE [STDP99, THP+94, STD+99, STDP00]. Prior to the MnAs film growth, a 100 μm thick epi-ready GaAs (001) wafer was coated with a 100 nm thick GaAs buffer layer at a substrate temperature of 550 °C after the oxide desorption. The buffer layer ensures atomically smooth surfaces for the growth of high quality MnAs films with a sharp interface. The substrate is then cooled down to 250 °C and the MnAs film of desired thickness is grown on GaAs at an As_4/Mn beam equivalent pressure ratio of 250 with a growth rate of 20 nm/hour [Sch00].

Epitaxial films are grown on very As rich GaAs (001) templates, obtaining the following epitaxial relationship (also shown in Fig. 2.3):

$$\text{MnAs } (1\bar{1}00) \parallel \text{GaAs } (001) \text{ and}$$
$$\text{MnAs } [0001] \parallel \text{GaAs } [1\bar{1}0] \quad .$$

The lattice mismatch[2] between MnAs and GaAs along the c-axis is reduced from its actual value to -4.8% by the coincidence lattice matching, where every 4^{th} MnAs {0002} plane matches with every 6^{th} GaAs {220} plane [TSDP01]. From transmission electron microscopy (TEM) studies it is known that, besides the above mentioned 4:6 matching, there is also a 6:8 matching leading to a further reduction of the misfit. This misfit is still comparably large, but small enough to allow epitaxial growth. The lattice misfit along the other in-plane direction (perpendicular to the c-axis) is -6.9%. This misfit is accommodated by regularly arranged misfit dislocations [TSDP01, Tra02].

---

[2] along the c- and the a-axis the lattice mismatch is -28.58% and -6.94%, respectively [TSDP01, Tra02].

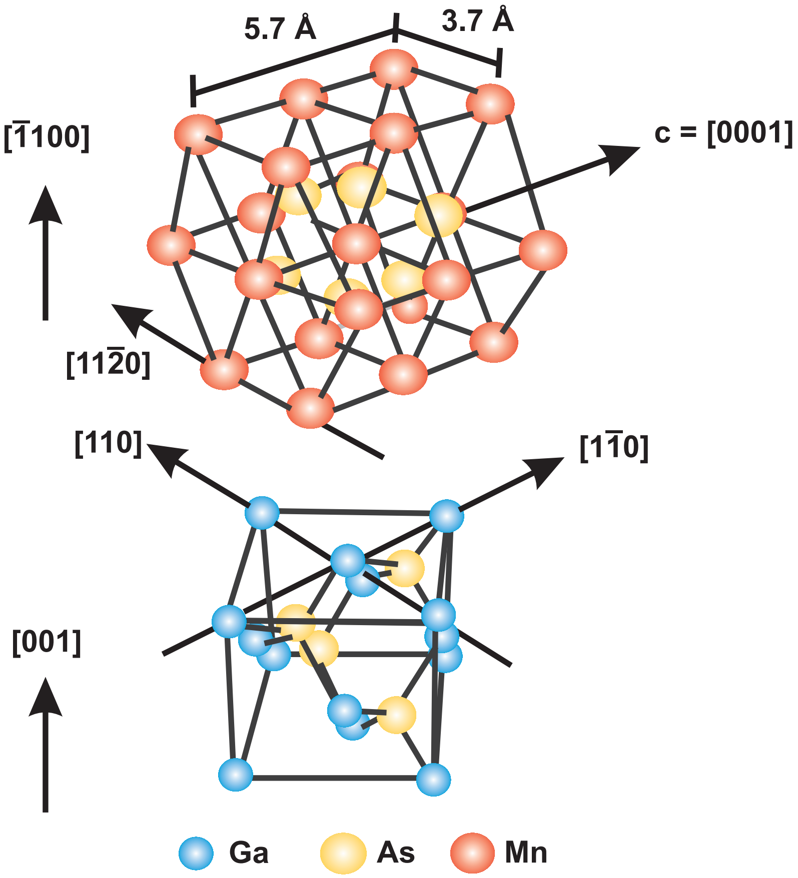

Figure 2.3: Epitaxial relationship for MnAs growth on an As-rich GaAs (001) template.

For our studies, MnAs films of various thicknesses ranging from 20 nm to 500 nm (Sect. 4.3) were grown on different substrate orientations (Sect. 4.2), namely GaAs (001), (311)A, as well as (111)B.

Chapter 3

Magnetic Measurement Techniques

Various measurement techniques were employed to characterize the magnetic properties of the epitaxial MnAs films. The micromagnetic properties were studied using MFM and XMCDPEEM. The magnetic interaction mechanism as well as the information depth of both methods is different, delivering complementary information about the magnetic system. The macroscopic magnetic properties (integral properties) were measured using SQUID magnetometry. A brief overview of the experimental methods will be presented in this Chapter.

3.1 Magnetic force microscopy (MFM)

MFM [ASBW87, SGG$^+$87, SGS88, MW87, GMH$^+$88, MRW88, MRS$^+$88, RME$^+$88, AWW88] serves as an experimental tool for mapping the magnetic domain structure using a ferromagnetically coated cantilever. In this Section, a detailed overview of the technique as well as model simulations will be presented in order to understand the nature of the contrast formation. Furthermore, the extension of the conventional MFM technique by an external magnetic field set-up and a variable-temperature stage will be highlighted.

3.1.1 Principle

MFM is based on non-contact atomic force microscopy (NC–AFM) and images the spatial variation of the out-of-plane component of the magnetic stray field of the sample surface. This is achieved by detecting changes in the reso-

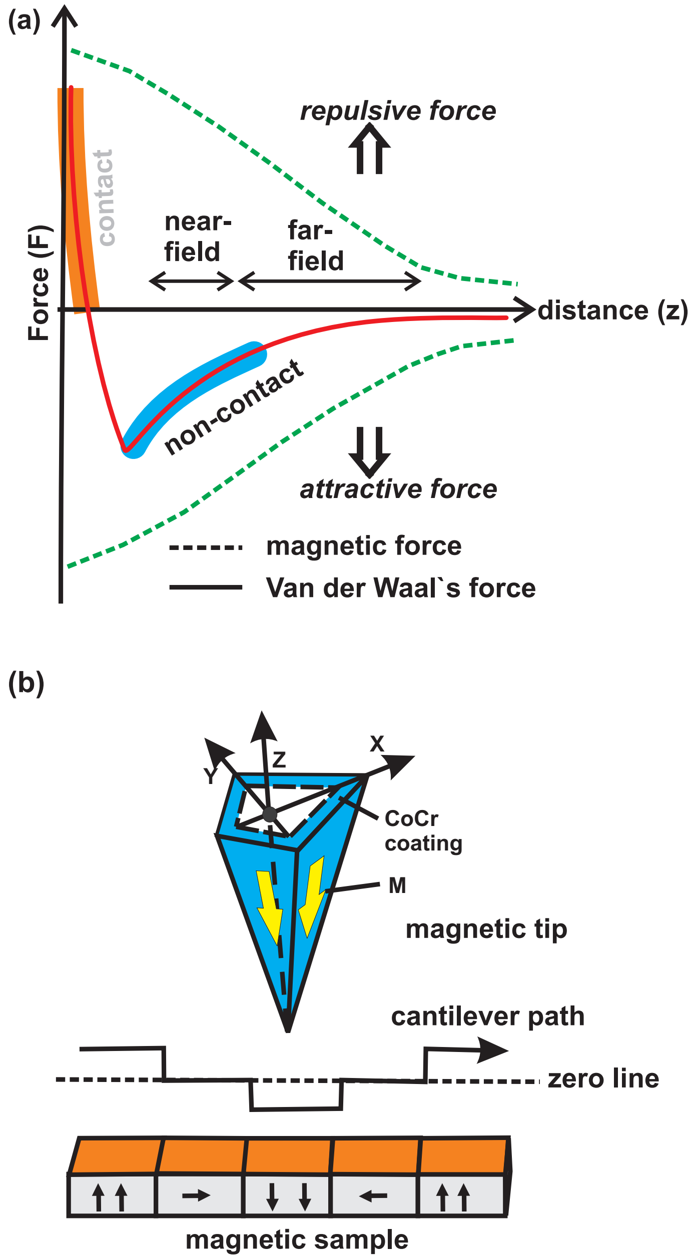

Figure 3.1: Basic MFM operation principle: (a) Shows the force-distance curve for both van der Waals force and magnetic force in both attractive and repulsive force regimes. (b) MFM working principle, where the path of the cantilever changes depending on the nature of the interaction between tip and sample magnetizations. Figure inspired by Ref. [PAR].

nant frequency of the cantilever induced by the magnetic field dependence of the tip-to-sample separation. Therefore, the forces between the magnetic tip and the magnetization of the sample must be included in the force-distance curve (Fig. 3.1), which is modeled in a simplified way by a Lennard-Jones potential[1]. For MFM operation, the non-contact AFM tip is coated with a ferromagnetic thin film (20 nm Cr and 60 nm Co [Tip]), where Cr is used as an oxidation protection layer. Usually, the tip is magnetized along its axis. Hence, MFM is primarily sensitive to the out-of-plane magnetization component of the magnetic stray field of the sample. The magnetic moments in the interacting volume of the magnetic film, together with the magnetic properties of the ferromagnetic tip, determine the interaction between the tip and sample and thus the resulting MFM signal.

The resonant frequency of a cantilever varies proportionally to the square root of its spring constant. In addition, the spring constant of the cantilever varies with the force gradient experienced by the cantilever. Finally, the force gradient, which is the derivative of the force-distance curve (shown in Fig. 3.1), changes with the tip-to-sample separation. Thus, changes in the resonant frequency of the cantilever can be used as a measure of changes in the force gradient, which reflect the changes in the tip-to-sample distance.

Measuring the sample's stray field from greater distances effectively decreases the sensitivity of the measured magnetization, as it varies inversely proportional to the distance. Therefore, the highest spatial resolution is obtained for the smallest tip-to-sample distances. Experimentally, however, the minimum tip-to-sample distance is limited by the relative strength of the magnetic interaction force with respect to the van der Waals and also to short range forces that play a role at distances closer to the sample.

A typical image recorded with a MFM contains information about both the topography and the magnetic properties of a surface. Which effect dominates in the image depends upon the distance of the tip from the surface, because the magnetic force persists for greater tip-to-sample separations (far-field regime) than the van der Waals force. If the tip is close to the surface (near-field regime), where standard NC–AFM is operated, the image will be predominantly show topographic features. By increasing the separation between the tip and the sample, magnetic effects become visible. Hence the

---

[1] $V(r) = -(A/r^6) + (B/r^{12})$, where the first term describes the repulsive interaction of the atomic potential and the second term the attractive van der Waals interaction, respectively.

key to understand MFM is to identify the force or force gradient term that is dominant in a given tip-to-sample distance regime.

3.1.2 Variable-temperature MFM

MFM equipped with a temperature stage is essential for studying the magnetic phase transition, as well as temperature-induced domain dynamics, in magnetic systems. We combined the MFM set-up with a variable-temperature sample stage, consisting of a programmable temperature controller with a micro miniature refrigerator and a sample heater [MMR].

In principle, this set-up allows controlled temperature measurements from 20 K to 400 K with a temperature stability of ± 0.05 K (in a controlled atmosphere or in vacuum) [MMR]. It consists of a ceramic pad (14×13 mm^2) with a temperature sensor and a resistive heater, where the sample is mounted on top using a heat-conductive paste to ensure uniform distribution of the heat. The set-up is optimized for low thermal drift operation. For measurements at temperature above 278 K in ambient atmosphere, we employed a Peltier cooling element. Silicone grease is used for mounting the Peltier cooler to the heat sink in order to distribute the heat effectively.

3.1.3 Variable-field MFM

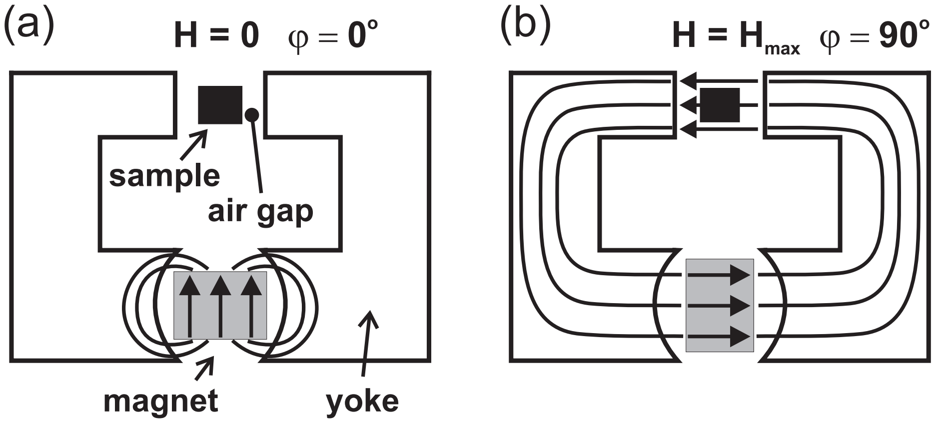

Figure 3.2: Principle of the variable-field magnet set-up: Depending on the rotation angle of the magnet, a variable amount of flux which is guided by the yoke passes through the sample. The minimum and maximum flux configurations are shown in (a) and (b), respectively.

Magnetic field-dependent MFM is essential for studying magnetization reversal processes. Compared to standard MFM measurements (zero field and room temperature), variable-field combined with variable-temperature MFM opens the door for studying magnetic phase transitions, magnetization reversal processes, as well as the field-dependent domain evolution.

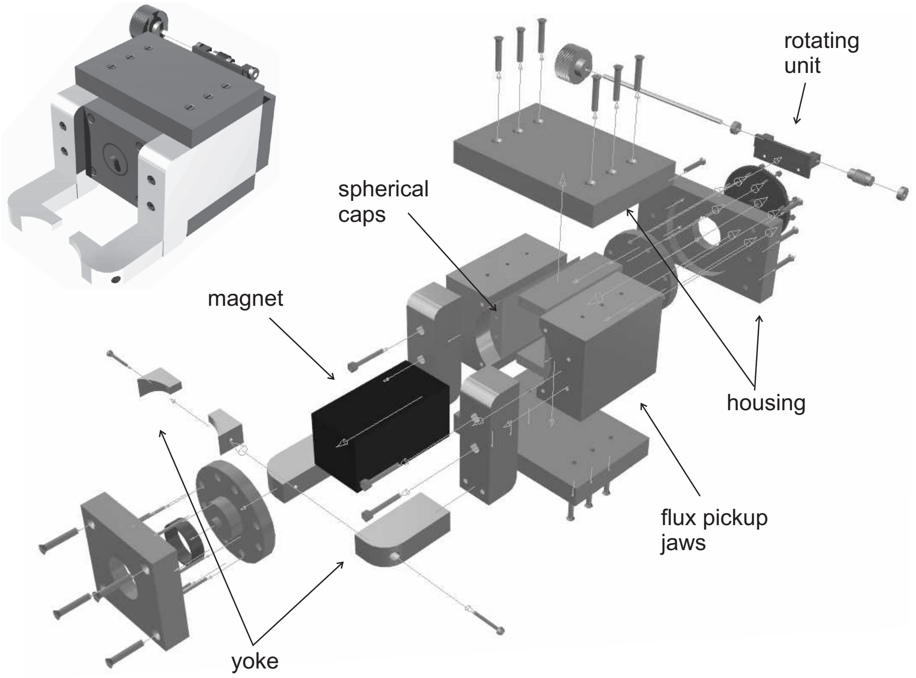

Figure 3.3: Explosion sketch showing the variable-magnetic field assembly consisting of the permanent magnet, its rotating unit, as well as the yoke which serves as a flux guide. On the top left of the figure, a 3-dimensional sketch of the assembled rotating permanent magnet is shown. Drawing by R. Engel-Herbert.

We have combined our existing variable-temperature MFM set-up with an external variable-magnetic field capability. The heart of the set-up is a NdFeB permanent magnet ($10\times5\times5$ cm^3)[Mag], which is placed inside the spherical cap and can be rotated with the help of a handle. The magnet, together with the spherical caps, is placed inside a flux pick-up assembly. The defined rotation of the magnet allows for a selective amount of flux to be guided through the yoke to the sample space. The yoke is made of soft iron and it is annealed in an hydrogen atmosphere in order to reduce the remanent magnetization [Fe]. The two extreme conditions of the rotation angle (φ) along with the corresponding amount of flux are shown in Fig. 3.2.

The design of the magnet and the sample space (3×1.2 cm^2) is limited by the space required by the temperature stage. Excluding the two side walls that are used as the part of the yoke, the other sides of the magnet assembly are covered by an aluminum housing. Details of the variable-magnetic field assembly are shown in Fig. 3.3.

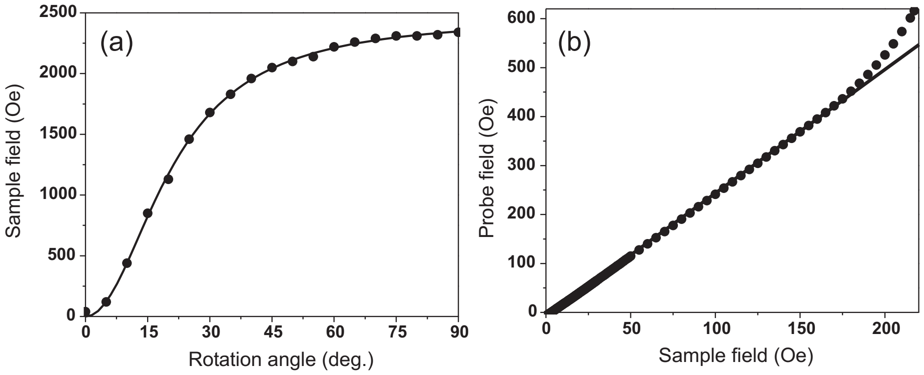

Figure 3.4: Calibration of the magnet: (a) Shows the variation of the sample field with respect to the rotation angle of the magnet and (b) the variation of the sample field with respect to the probe field at the sample position.

The field at the sample position (sample field) is calibrated with respect to the rotation angle. The maximum field in this geometry is 2360 Oe. If desired, higher values can be achieved by shrinking the sample space. In order to precisely vary the magnetic field at the sample position, a Hall probe [Tes] is attached to one of the yokes in order to pick up a proportional probe field. Both fields are consequently calibrated with respect to each other, which also gives the opportunity to monitor the field at the sample position during the measurements. Details of the calibration are shown in Fig. 3.4. It can be seen that the *probe field* varies almost linearly with the *sample field*, except for a very small non-linearity at high field values. With this set-up, many interesting micromagnetic properties of the material system are studied. Details of the variable-field measurements can be found in Sect. 5.4 and Chapter 6.

3.1.4 MFM contrast simulation

MFM has been widely used as a magnetic imaging technique with high resolution without the need for any sample preparation. However, complications arise in interpreting the contrast in a quantitative way. In MFM, the cantilever with the magnetic tip is deflected due to the interactions between tip and sample as a function of the tip-to-sample distance. A particular MFM contrast has not a one-to-one correspondence in the magnetization of the sample, as there are a number of magnetization patterns leading to the same magnetic stray field. In practice, the MFM measures the force (force gradient) derived from the tip-sample interaction, which is dependent on the deflection (change in resonant frequency) of the cantilever. Further complications arise if we take the perturbing interactions between the tip and the sample into account, which depend on a number of parameters, e.g. tip and sample material, tip geometry and magnetization, sample magnetization and tip-to-sample working distance.

In order to understand the domain structures of our material system that leads to the observed images, R. Engel-Herbert performed simulations of the MFM contrast [EHon]. The simulation consists of an analysis of the MFM response, followed by calculating the stray field of the assumed micromagnetic structure of the sample and the magnetized tip. The resulting MFM image is a convolution of the sample stray field with the tip function at specific working distances. Furthermore, to make a simple simulation, we assume no perturbation effect of the tip on the sample and *vice versa*. We assume a dipole-dipole interaction between the tip and the sample. Hence, the total force $\vec{F}_{tot}\left(\vec{r}\right)$ acting on the tip due to the magnetic stray field of the sample is given by [Har88, Har90, SGG$^+$87]:

$$\vec{F}_{tot}\left(\vec{r}\right) = \int_{tip} \left(\vec{M}_{tip}\left(\vec{r}\,'\right) \cdot \vec{\nabla}_{\vec{r}}\right) \vec{H}_{sample}\left(\vec{r} - \vec{r}\,'\right) d^3\vec{r}\,' \,, \tag{3.1}$$

where ($\vec{r}$-$\vec{r}\,'$) represents the distance between the two dipoles, namely the tip and the sample, $\vec{H}_{sample}(\vec{r})$ is the magnetic field of the sample and $\vec{M}_{tip}(\vec{r})$ is the tip magnetization.

The tip is magnetized along its axis and, due to the geometry of the tip and coating layer, all the magnetic moments align along the tip axis, i.e. $M_{tip} = (0, 0, M_z)$, as shown in Fig. 3.1. The effective force $\vec{F}_z(\vec{r})$ that the tip experiences can be written as:

$$\vec{F}_z'\left(\vec{r}\right) = \int\limits_{tip} \left(\vec{M}_z\left(\vec{r}\,'\right) \cdot \frac{\partial^2}{\partial z^2} \vec{H}_z\left(\vec{r} - \vec{r}\,'\right) d^3\vec{r}\,'\right) \,, \tag{3.2}$$

where the subscript "z" stands for the normal component of the respective parameters.

For the simulation, various possible distributions of the magnetization of the film are assumed, based on the information obtained from SQUID magnetometry measurements. The stray fields of the assumed structures are then calculated with the help of the magnetostatic potential. Finally, the volume integration over the total sample gives the resulting stray fields. The stray field contributions are divided into two parts: one is due to the in-plane component of the magnetization vector along the easy magnetization axis and the other is due to the out-of-plane contribution of the 180° Bloch walls between two oppositely aligned in-plane magnetizations. The contribution of the two stray fields at the tip position show different distance dependencies. Finally, the convolution gives the simulated MFM contrast [EHon].

3.2 Complementary magnetic measurement techniques

In order to understand the magnetic properties of the system under investigation MFM measurements alone are not sufficient. For performing a complete magnetic characterization, complementary techniques are employed that allow for a detailed and in-depth understanding of the integral and microscopic magnetic properties, measured by SQUID magnetometry and XMCDPEEM, respectively.

3.2.1 Super conducting quantum interference device (SQUID) magnetometry

After the discovery of superconductivity and quantum phenomena, like the Josephson effect and flux quantization, SQUID magnetometry based on these effects came entered the research area. It allows for the measurement of the integral properties of the magnetic material. SQUID magnetometry is based on a field probe that consists of two Josephson junctions forming a superconducting ring. Applying a current to the SQUID activates Cooper pair tunneling across the junctions. A magnetic field applied to the ring, however, alters the flow. It changes the quantum-mechanical phase difference across each of the two junctions. These phase changes, in turn, affect the critical current of the SQUID. A progressive increase or decrease in the magnetic field causes the critical current to oscillate between a maximum and a minimum value. The maximum occurs when the flux administered to the SQUID equals an integral number of flux quanta through the ring. The minimum value corresponds to a half-integral number of quanta. In practice, we do not measure the current but rather the voltage across the SQUID, which also swings back and forth under a steadily changing magnetic field, shown in Fig. 3.5(b). This quantum interference effect provides us with a digital magnetometer, where each digit represents a flux quantum. In essence, the SQUID is a flux-to-voltage transducer, converting a tiny change in magnetic flux into a voltage. A schematic of the SQUID is shown in Fig. 3.5.

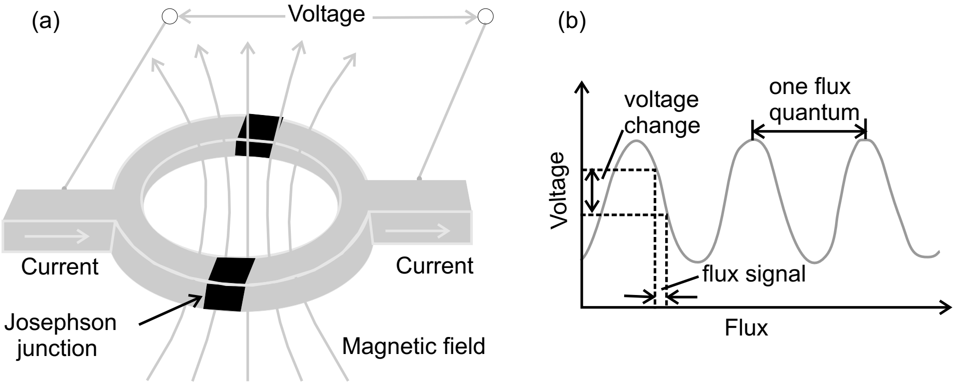

Figure 3.5: Schematic of the SQUID measurement principle: (a) Shows the two Josephson junctions forming a superconducting ring, which provides the information about the change in flux. (b) Shows the output voltage as a function of flux. Figure inspired by Ref. [Cla94].

The SQUID system [SQU] is composed of several units: the dewar, the probe and SQUID assembly, and the electronic control system. The probe contains a high precision temperature control system, allowing measurements between 1.9–400 K and with an accuracy of 0.01 K (according to the data sheet), and a superconducting electromagnet, delivering a field of up to 5×10^4 G with a field accuracy of 0.1 G. The dewar consists of an inner liquid helium reservoir and an outer liquid nitrogen jacket, to reduce excessive liquid helium boil-off. The liquid helium is used both for maintaining the electromagnet in a superconducting state and for cooling the sample space. The samples are mounted within a plastic straw and connected to one end of a sample rod which is inserted into the dewar/probe. The other end is attached to a stepper motor which is used to position the sample within the center of the SQUID pickup coils. The generated magnetic field is well-shielded from the surroundings.

3.2.2 X-ray magnetic circular dichroism photoemission electron microscopy (XMCDPEEM)

XMCDPEEM combines two techniques, namely X-ray magnetic circular dichroism (XMCD) and photoemission electron microscopy (PEEM). The absorption intensity of circularly polarized X-rays by a ferromagnetic material is different for parallel and antiparallel alignment of the magnetization direction and the polarity of the incident photon spin. This phenomenon is known as XMCD [ISKK02]. As a result of the X-ray absorption, secondary electrons are emitted from the sample. An electron microscope (a so-called PEEM) is used to analyze the secondary electrons. The combination of the two techniques results in the formation of a micromagnetic image of the ferromagnetic material. As high-intensity X-rays utilize absorption edges due to the electronic excitation from core levels to the empty levels, XMCD results in the detection of spin and orbital moments in an element-specific way. Details of the principle are shown in Fig. 3.6.

In order to understand the XMCD principle a model case has been taken into consideration, where circular polarized X-rays with a photon spin ($\mu = 1$, i.e. μ_+) are incident onto the sample along the easy magnetization direction causing an excitation of 2p core level electrons to the 3d conduction band. We choose two distinguished regions, namely region I [majority spin upward (↑)] and region II [majority spin downward (↓)] with the magnetization parallel and antiparallel to the incident photon spin, respectively. Spin-orbit interaction is taken into account leading to a splitting of the 2p core level to $2p_{3/2}$ and $2p_{1/2}$ states, where spin and orbital angular momenta couple parallel and antiparallel to each other, respectively.

For simplicity, the occupation for majority and minority spins is selected to be 4/5 and 1/5, respectively. The transition probability of the spin up (↑) and spin down (↓) electrons for $2p_{3/2}$ is 100 and 60, whereas for $2p_{1/2}$ it has the values of 20 and 60, respectively. The product of the transition probability and occupation of the spin states gives the allowed transition, which is proportional to the photo-absorption intensity of the ferromagnet. Therefore, the absorption is stronger for the parallel alignment of the sample magnetization and photon spin, which leads to brighter contrast, as it is shown in region I and region II of the $2p_{3/2}$ and $2p_{1/2}$ states, respectively.

For our measurements we used the nanospectroscopy beamline of the ELETTRA synchrotron in Trieste [Ele]. The set-up combines a low energy electron

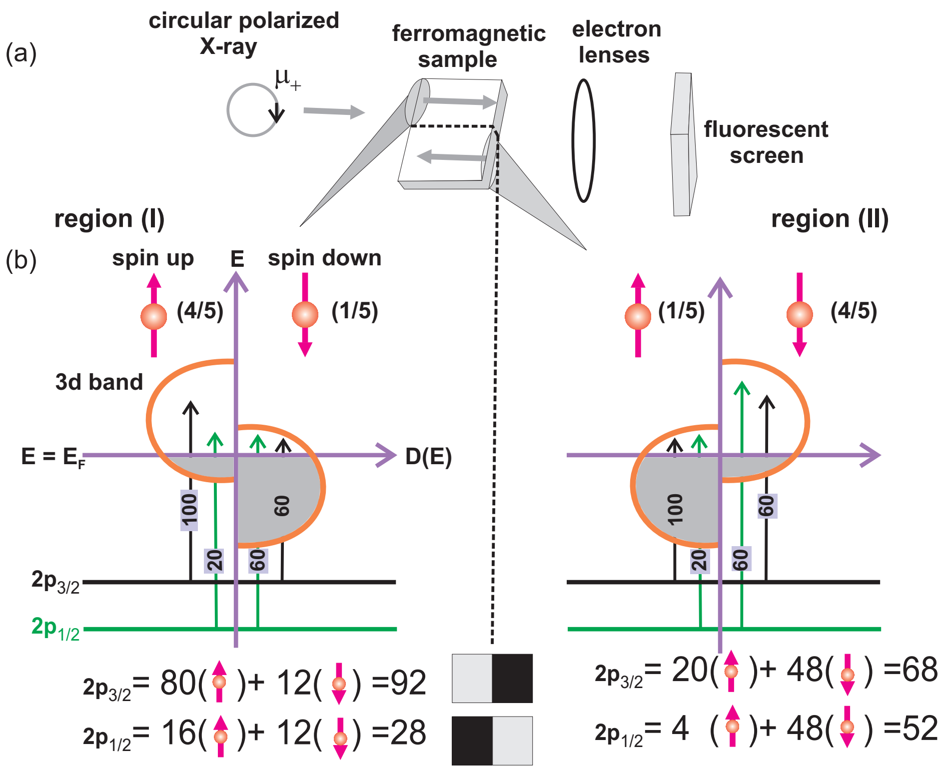

Figure 3.6: (a) Sketch of the XMCDPEEM principle: Circular polarized X-rays of one polarization hit the ferromagnetic sample. The secondary electrons emitted from the sample pass through the electron lenses and are projected onto the fluorescent screen to produce an image. (b) Sketch illustrating the XMCD contrast formation in a ferromagnetic sample [ISKK02]. The transition probabilities from 2p to 3d bands for the spin-up and spin-down electrons for the two differently magnetized regions of the sample are shown. The observed contrasts are presented at the bottom of (b) and the total numbers are obtained by considering the occupations and transition probabilities of spin-up and spin-down electrons.

microscopy (LEEM) facility together with XMCDPEEM [SHS$^+$98, BCD$^+$02]. LEEM images the topography, whereas XMCDPEEM gives the in-plane magnetic contrast of the same area. The combination of these two techniques serves as complementary techniques to AFM and MFM. After taking the LEEM image, e.g. left circular polarized X-rays are focussed onto the sample surface along the easy magnetization axis (a-axis, as shown in Fig. 3.7). It takes about 30 seconds to reverse the polarity [to right circular polarization of the incident photon beam and then the second image is recorded. The difference image between the left and right circular polarized light images is the XMCDPEEM image.

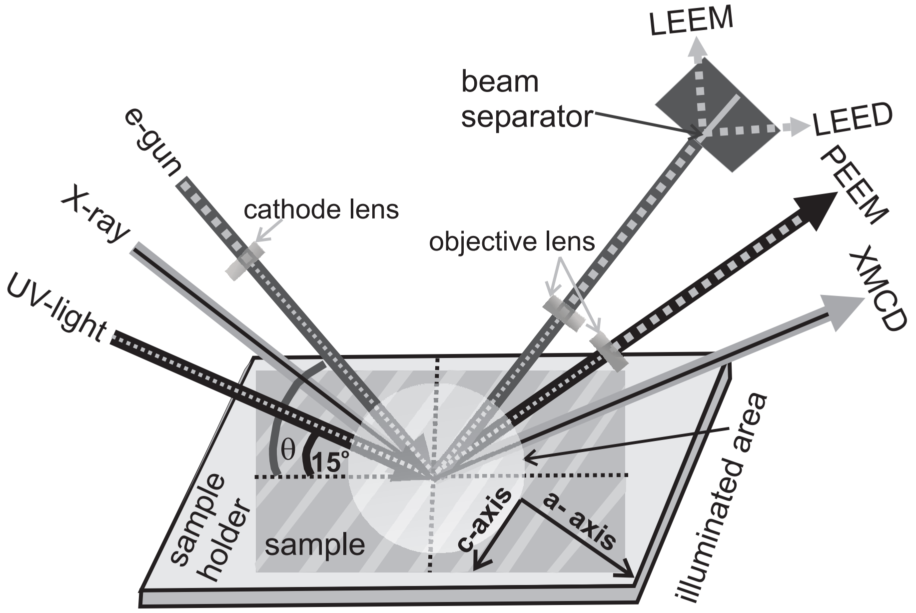

Figure 3.7: XMCDPEEM together with LEEM and LEED principle: Microprobe sample analysis at the nanospectroscopy beamline allowing for XMCDPEEM, LEEM, LEED on the same sample spot. For standard PEEM imaging, UV-light is used at an incident angle of 15°.

The geometry of the measurements, as well as the beamline facility, is shown in Fig. 3.7 and Fig. 3.8, respectively. For PEEM, low photon energy light is incident on the sample to excite only those electrons from the valence band which are able to overcome the work function barrier with a kinetic energy of typically 0–2 eV. These photoemitted electrons are then accelerated to about 18 keV in the objective lens placed in front of the sample. Finally, the image formed by the objective lens is transformed to the phosphor screen with the help of a video or CCD camera. PEEM images photoemitted electrons and thus generates a spatial map of the absorption of the sample [SPA$^+$98, Bau01, SS02, ZNG99]. For XMCD-PEEM, a polarized X-ray source is used and the emitted secondary electrons are mapped with the PEEM microscope as explained in this Section. In LEEM mode, electrons from the source are first collimated and then, by using the cathode lens, decelerated. The low energy electrons that hit the

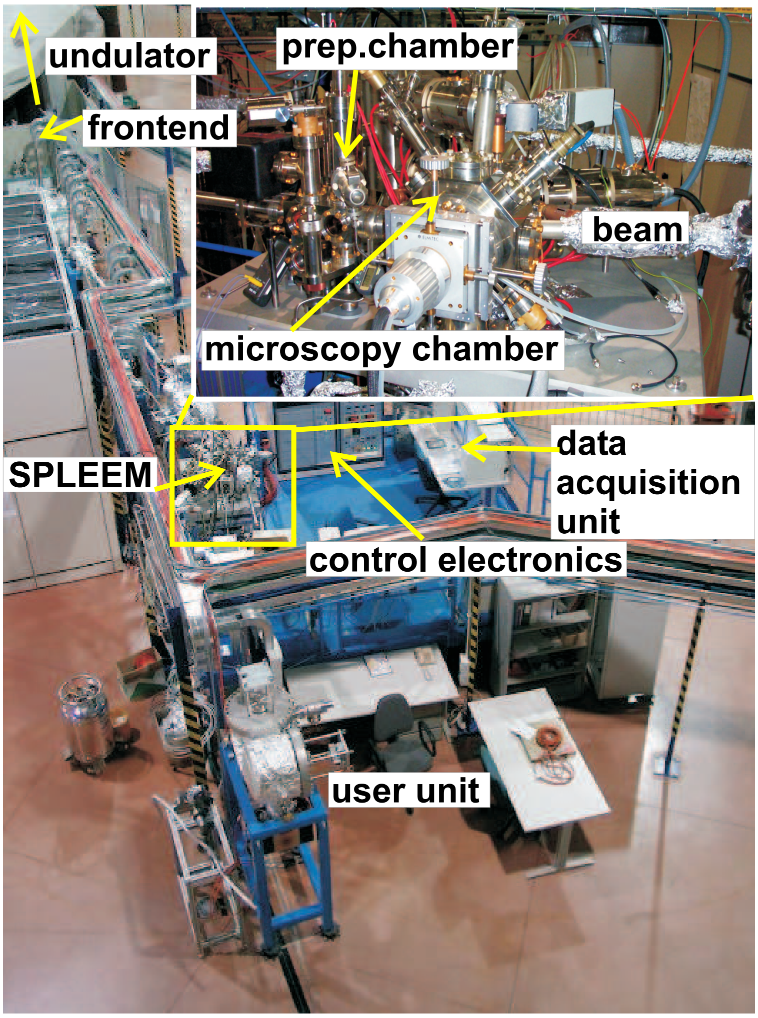

Figure 3.8: Picture of the Elettra nanospectroscopy beamline.

sample surface are finally accelerated again to 18 keV in the objective lens [Bau98, Bau94, PS03, TMR$^+$98, GB96, Tro00, SKM$^+$98].

For LEEM the electrons are in most cases incident normal to the surface (θ = 90°) in order to have a high intensity of the back scattered electrons which give the contrast [Bau98, PS03]. For the best resolution, the illuminating beam and the imaging beam have the same optical axis which is normal to the sample surface. Therefore, the illuminating beam must be separated from the imaging beam in order to see the image, otherwise only diffraction can be seen. This is done by a beam splitter, where the accelerated electrons are deflected into the image column and finally transferred to the camera. The LEED pattern due to the reflection of the electrons from the surface is imaged by the objective lens. The contrast mechanism in LEEM originates from the local differences in the reflectivity given by the differences in intensity of the specular reflected beam due to the surface topography, the crystal structure, adsorbates and others [Bau98, Bau94, PS03, ACL98, REM$^+$98]. In addition to the specular beam also other beams, corresponding to so-called *bright field* and *dark field* imaging, are used. LEEM also detects interferences due to atomic steps on the surface by detecting the optical path differences [CA98, Bau98]. All these electron microscopy techniques use direct imaging, meaning a parallel image acquisition with faster image recording compared to the standard scanning techniques, where a sequential image acquisition technique is used for imaging with longer acquisition time.

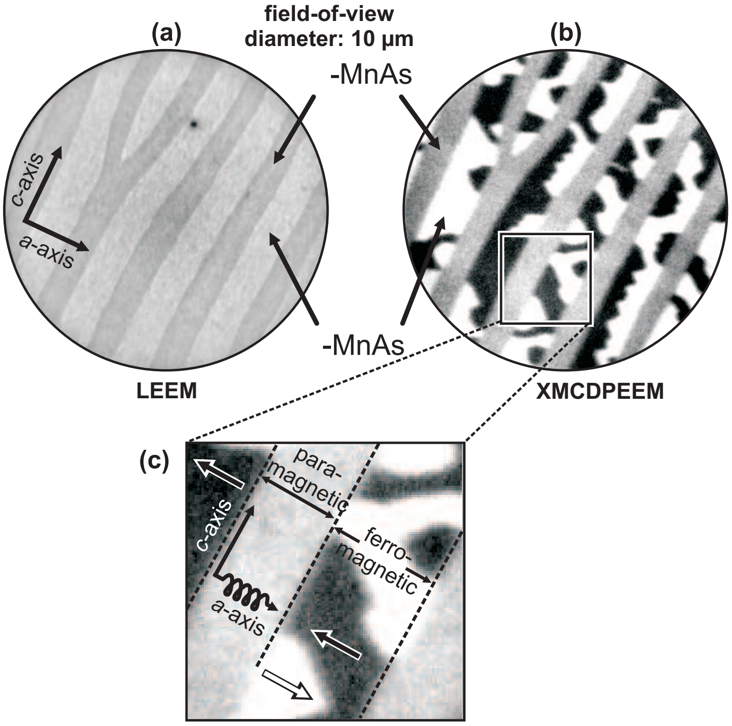

Figure 3.9: 500 nm thick MnAs film on GaAs (001) imaged with LEEM (a) and XMCDPEEM (b) showing the topography and magnetic contrast, respectively. The magnified domain pattern (c) shows the two antiparallel magnetization directions in α-MnAs giving rise to black and white contrast. The arrows and the wavy line indicate the direction of the magnetization axes and photon wave vector (along the magnetic easy axis [a-axis] direction of MnAs).

Figure 3.9 shows an example of the topographic (LEEM) and the corresponding magnetic contrast of a 500 nm thick MnAs film on GaAs (001). For the XMCDPEEM measurements, an As cap is grown on the MnAs films before transferring them from the MBE system to the experiment at ELETTRA. The samples are mounted in such a manner that the easy magnetic axis of MnAs is in the plane of incidence of the light. After complete desorption of the arsenic cap, low energy electron diffraction (LEED) patterns of MnAs $(\bar{1}100)(1\times2)$ are obtained. For XMCDPEEM imaging, the secondary electrons resulting from the photo-ionization of the Mn L_3 level with a photon energy of 639.5 eV are used. The LEEM image is obtained with 4.5 eV electrons. Depending on the relative orientation of the sample magnetization and photon wave vector either black or white contrast can be seen, which is shown in the magnified domain pattern in Fig. 3.9 (c). The gray contrast is due to the paramagnetic β-MnAs. The topographic LEEM contrast is a result of the height difference between the stripes of different MnAs phase composition.

Chapter 4

Magnetic Properties of MnAs

In this Chapter, the magnetic properties of MnAs films will be discussed. The typical domain structures of MnAs will be presented, as observed by MFM and XMCDPEEM. The MFM contrast simulation for the measured domain patterns will be discussed. Finally, the influence of the substrate orientation and the effect of the film thickness on the magnetic domain structure will be addressed.

4.1 Domain structure of α-MnAs films

MnAs films grown on GaAs (001) show a periodic array of stripes (stretched along the a-axis direction) of ferromagnetic α-phase and paramagnetic β-phase in an alternating arrangement. Figure 4.1 shows the topographic contrast measured by AFM [Fig. 4.1(a)]. The periodic stripe structure exhibits a height modulation of about 1.7% that is visible in the topography. The corresponding MFM image of the same scan area [Fig. 4.1(b)] shows magnetic contrast on the ferromagnetic stripes that appear as ridges in the topographic image [SBD$^+$00].

A number of different domain structures are visible on the ferromagnetic stripes. In order to understand the typical MFM contrast for simple domain structures, we consider bar magnet-like domains. Figure 4.2(a) shows sketches to explain the contrast mechanism resulting from the interaction of the tip magnetization with the stray field of the domains. The ferromagnetic stripe is assumed to be divided into oppositely oriented bar magnets along the total width of the ferromagnetic stripe [see Fig. 4.2(a)]. This assumption is justified as this material has one easy magnetization direction along the width of the stripe. The magnetic stray field of the bar magnet-like do-

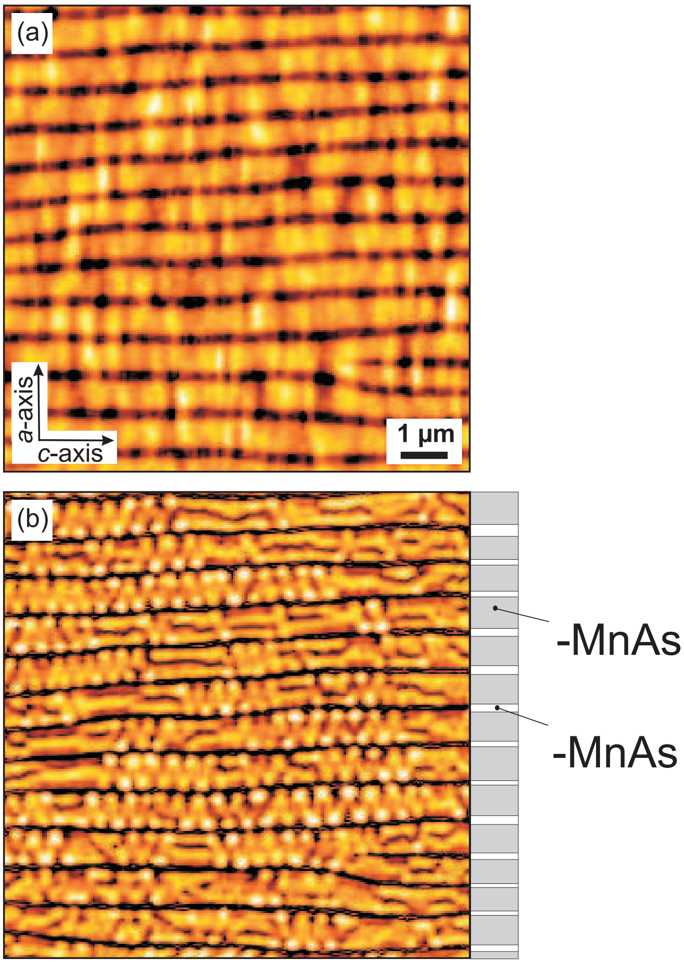

Figure 4.1: (a) AFM and (b) MFM picture of a 180 nm thick MnAs film on GaAs (001) at room temperature.

mains will either point up (out-of the plane) or point down (back into the plane) at the end of the ferromagnetic stripe, as shown by arrows in the top left sketch in Fig. 4.2(a). The MFM is sensitive to these out-of-plane components which interact with the tip magnetization [cf. downward pointing arrow in Fig. 4.2(a)]. The interaction between the tip and the stray field of the sample depends on the relative orientation of these two vectors. The parallel (antiparallel) orientation of the two magnetization vectors results in an attractive (repulsive) interaction, giving a bright (dark) contrast as shown in the bottom left of Fig. 4.2(a).

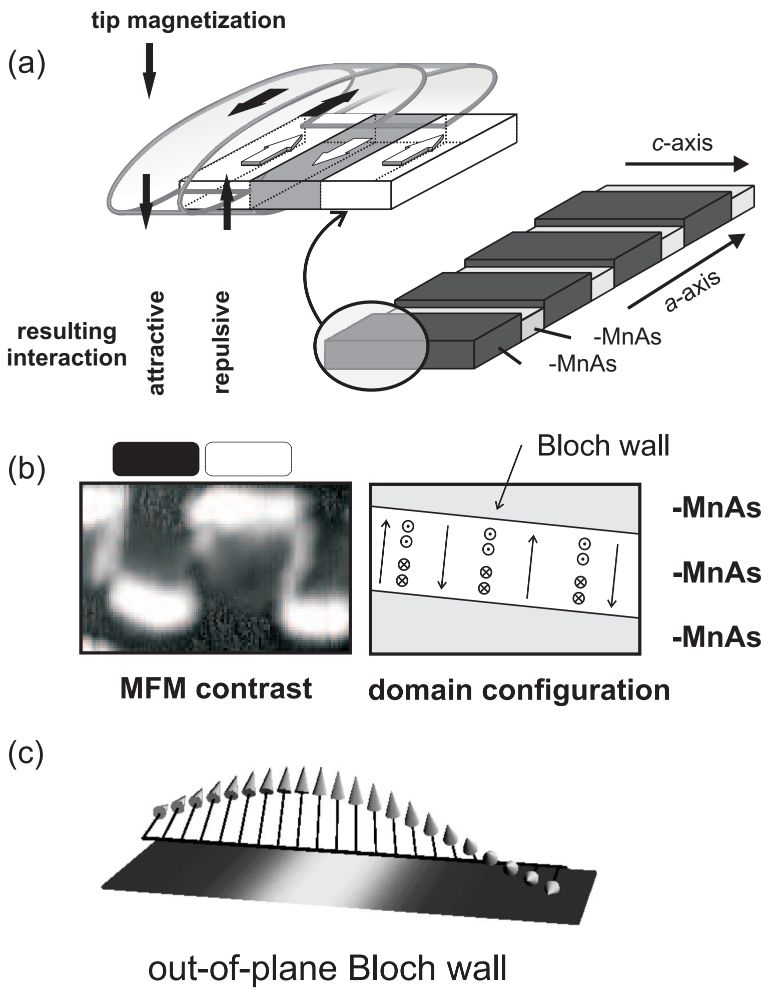

Figure 4.2: (a) Sketch of the periodic arrangement of the MnAs α- and β-phase. A small section of the α-MnAs is highlighted in the top left corner showing oppositely arranged bar magnets and their stray fields as indicated by arrows. (b) Resulting interaction between the tip and the sample magnetization orientation. The MFM scan below shows the alternatingly arranged in-plane bar magnet-like domains, separated by 180° Bloch walls. (c) Shows a typical sketch of the 180° out-of-plane Bloch wall, where the moment changes its in-plane direction by rotating out-of-plane (either pointing out-of or into the sample plane).

Besides this magnetic contrast, a thin line-like, black and white contrast is also seen between two oppositely oriented domains, which is shown in Fig. 4.2(b). This contrast is due to 180° Bloch walls where the magnetization vector rotates out-of-plane to reverse its direction between two oppositely magnetized in-plane domains. On the right hand side of Fig. 4.2(b), the most likely domain configuration (including Bloch walls) is sketched that corresponds to the experimental image on its left.

In order to quantify the observed micromagnetic configurations, we introduce a domain classification scheme that is based on the results obtained by MFM and XMCDPEEM. The major difference between the two micromagnetic techniques is that MFM maps the sample's stray field convoluted with the tip magnetization at some distance from the surface, whereas XMCDPEEM directly maps the orientation of the magnetization vector in the sample with respect to the incident photon beam.

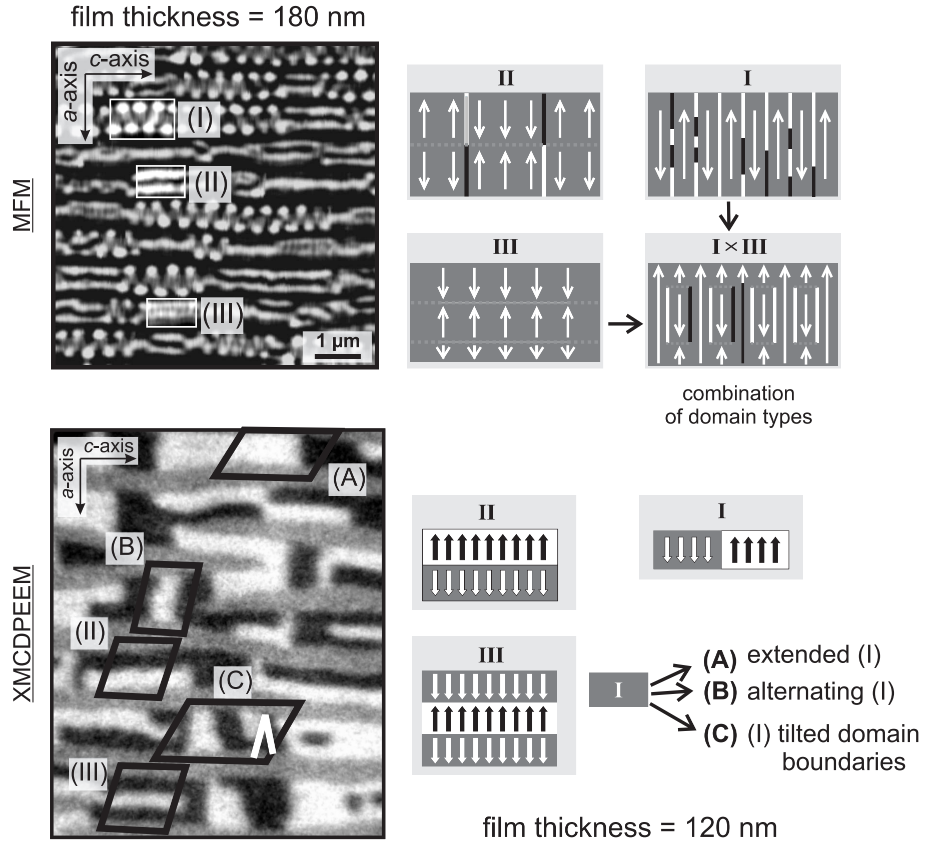

Figure 4.3: Classification of domain structures as observed by MFM and XMCDPEEM.

Figure 4.3 shows the classification of the magnetic domains as observed by MFM and XMCDPEEM. The classification of the domains is based on the number of subdomains along the easy axis direction within one stripe. The special case that the domain stretches across the whole ferromagnetic stripe [type(I)] is also discussed in this Section. The common case of two or three subdomains is termed type (II) and type (III) domain, respectively. The remainder of the observed domain types can be explained as combinations of the three basic domain types. Details of the classification based on MFM are shown on the top of Fig. 4.3. For a better understanding, the figure shows a MFM picture where the three domain types are marked with white rectangles. A sketch of the classification for all three types of domains and the combination of domains [type (I) and type (III)] are shown in the figure. The white and black lines between the oppositely-magnetized domains are due to the 180° Bloch walls as explained before. The classification scheme is strongly backed by MFM contrast simulations, which will be discussed in Sect. 4.4, and also by XMCDPEEM measurements. Figure 4.3 shows the domain pattern typically observed in XMCDPEEM measurements. For type (I) domains, we specify three different appearances: extended domains (marked A), alternating domains (marked B) and tilted domain boundaries (marked C). Extended domains are domains with one particular magnetization extending over the length of the stripe. In alternating domains, sequences of oppositely magnetized domains line up next to each other. We also observe unusual tilted domain boundaries at an angle of 38°, both in MFM and XMCDPEEM. For thicker films (300–500 nm), besides the discussed domain structures, more complicated domains are also seen, which will be discussed in Chapters 5 and 6. It has to be noted that the existence of the commonly observed type (II) and type (III) domains is quite surprising. In an uniaxial system such as MnAs on GaAs (001) or GaAs (311)A, one would only expect the presence of domains where the magnetization extends over the whole width of the ferromagnetic stripe.

4.2 Dependence of the magnetic properties on the substrate orientation

In epitaxial MnAs films, the interface between the film and the substrate plays an important role for the magnetic properties of the film. On the other hand, the strain in the film also changes if the film is grown on different substrate orientations. Therefore, MnAs films grown on three different substrate orientations of GaAs, namely (001), (311)A and (111)B are studied, which will be the subject of this Section.

4.2.1 MnAs on GaAs (001) and (311)A

For a comparative study, MnAs films have been grown on GaAs (001) and (311)A substrates under the same growth conditions by mounting two half wafers on one sample holder [DWJ$^+$04]. The growth conditions are the same as explained in Sect. 2.3. The epitaxial relationships for these two substrate orientations are shown in Tab. 4.1 [DST$^+$01, DKH$^+$03].

Table 4.1: Epitaxial relationships for MnAs growth of As-rich conditions on GaAs (001) and (311)A.

(001)	**(311)A**
very As rich	
MnAs $(1\bar{1}00)$ $\parallel$ GaAs (001)	MnAs $(1\bar{1}00)$ $\parallel$ GaAs (311)A
MnAs [0001] $\parallel$ GaAs $[1\bar{1}0]$	MnAs [0001] $\parallel$ GaAs $[\bar{2}33]$
MnAs $[11\bar{2}0]$ $\parallel$ GaAs [110]	MnAs $[11\bar{2}0]$ $\parallel$ GaAs $[1\bar{1}0]$

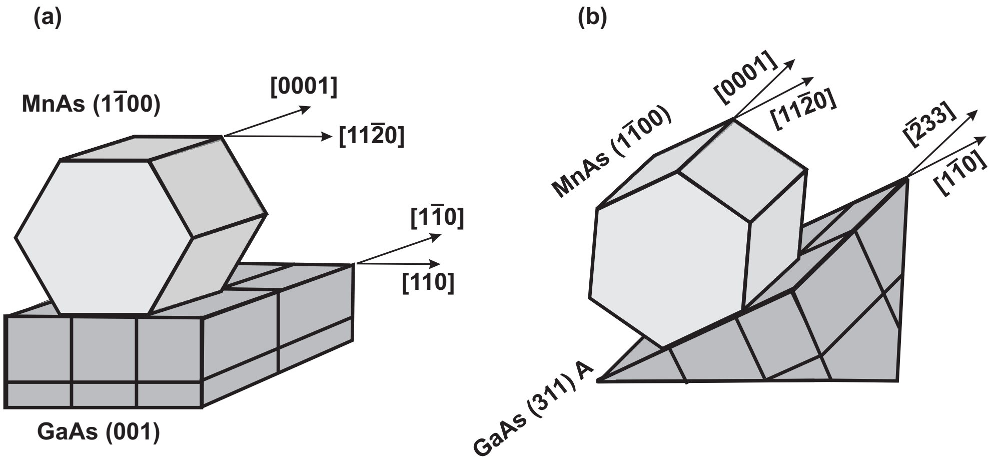

Figure 4.4: Sketch of the crystallographic orientations of epitaxial MnAs films on (a) GaAs (001) and (b) (311)A, respectively.

The (311)A surface results by tilting the surface plane from the (001) surface towards the (111)A surface by 25.2° (see Fig. 4.4) [DST$^+$01]. The misfit strain along the MnAs $[11\bar{2}0]$ direction is relieved by the formation of regularly arranged misfit dislocations. Along the MnAs [0001] direction, the misfit and relaxation mechanism for the [001] orientation as a result of coincidence lattice matching is explained in Sect. 2.3. In case of the GaAs

(311)A surface, the misfit is reduced by the formation of asymmetric tilt boundaries with respect to the interface plane as measured by TEM [Tra02].

High-resolution TEM shows that the MnAs $[1\bar{1}00]$ direction is tilted a few degrees out of the GaAs (311)A surface [DWJ+04]. Using a technique [PHRL91] based on high-resolution X-ray diffraction (HRXRD) measurements, it is found that the $(1\bar{1}00)$ MnAs planes are tilted [DWJ+04], and the observed tilt angle is 4° around the MnAs $[11\bar{2}0]$ axis. A minor tilt angle between the α- and β-MnAs domains of 0.05° is obtained [DWJ+04]. In contrast to this behavior, in the MnAs/GaAs (001) samples, the orientations of both phases are parallel. Along the perpendicular MnAs [0001] in-plane direction, i.e. along the c-axis, the interface configurations are different as the c-axis is tilted out of the interface plane in the MnAs/GaAs (311)A layer, whereas in the MnAs/GaAs (001) layer, the c-axis remains in the interface plane. This gives evidence for different strain relaxation mechanisms along this direction.

Considering the interface configurations of MnAs/GaAs (311)A and MnAs /GaAs (001) along MnAs $[11\bar{2}0]$, the crystal directions in both the epi-layers and the substrates are the same if we do not distinguish between the [110] and $[1\bar{1}0]$ directions of GaAs (001). Hence, the strain relaxation mechanism for both types of samples along this direction should be the same, and therefore, the characteristic stripe pattern discussed before is observed in both cases.

We are now looking into the magnetic properties of these films. The saturation magnetization increases for films up to a thickness of 70 nm and then decreases for both orientations, which suggests that at a thickness of 70 nm the inter- and intra magnetic coupling of the stripes is stronger. The saturation magnetization decreases for thicker films as the stripe period and the separation increases as a function of film thickness [DWJ+04]. A slight, but not significant tendency to lower magnetization values and stronger scattering of the observed data is a hint that the formation of the coupled ferromagnetic MnAs stripes is less perfect on GaAs (311)A compared to GaAs (001), which is a consequence of the differences in the interface structure.

We have studied the influence of the substrate orientation on the magnetic properties for 50-200 nm thick films. Figure 4.5 shows MFM, as well as AFM scans (only for the thicker films), of films grown on both orientations. For thinner films ($\approx$ 50 nm), the stripes are not clearly seen and the MFM contrast only shows patches of magnetic contrast. For thicker films

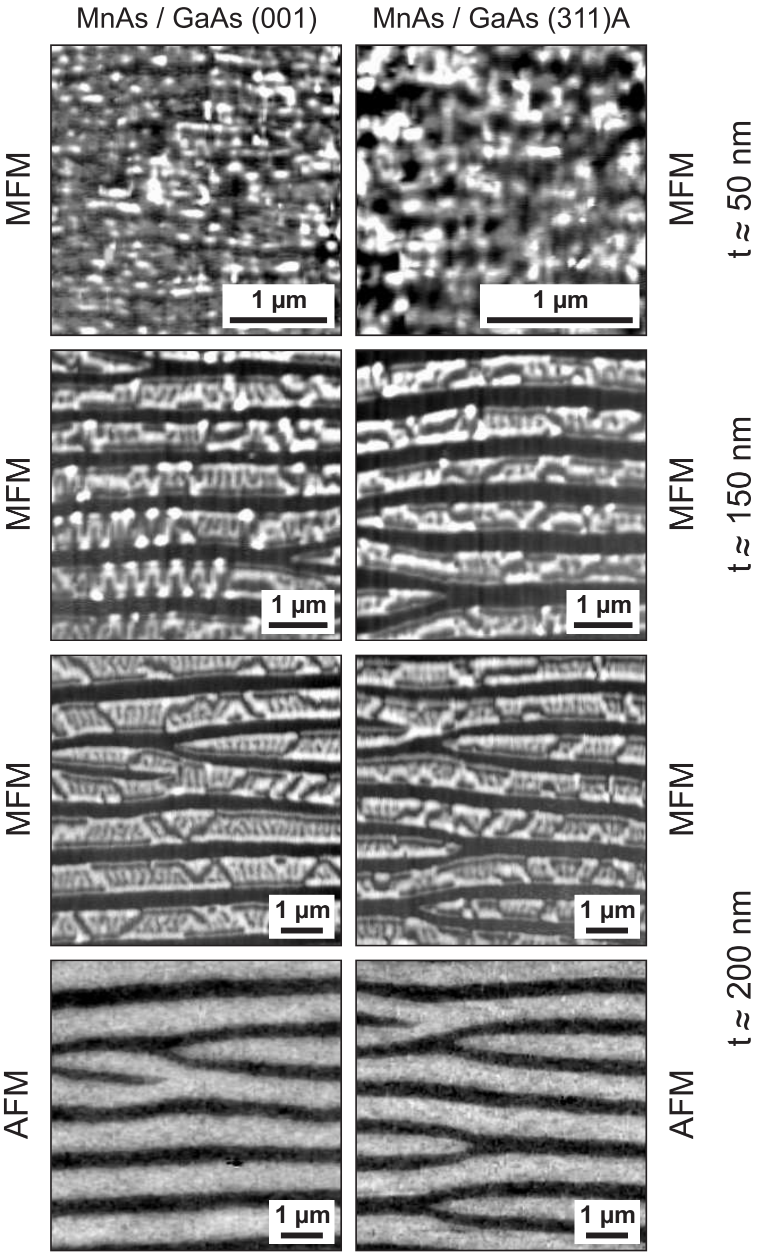

Figure 4.5: Substrate orientation dependence of the magnetic domain structure of MnAs grown on GaAs (001) (left hand side) and (311)A (right hand side). For comparison, the topography (AFM) of a 200 nm thick film is shown in the bottom row.

(100–200 nm), the α-β-stripe structure is clearly seen in the topographic contrast (bottom row). The typical type (I) domains, that are usually seen for MnAs/GaAs (001), are not so common for MnAs/GaAs (311)A (compare the MFM scans for 150 nm thick films in Fig. 4.5).

4.2.2 MnAs on GaAs (111)B

Due to the high technological relevance of the GaAs (001) surface, many studies focus on the growth on this surface. Here, the hexagonal MnAs crystal is growing with the *c*-axis in-plane, i.e. the growth plane is the prismatic MnAs $(1\bar{1}00)$ lattice plane, as shown in Tab. 4.1 and Fig. 2.3. This introduces a high degree of in-plane anisotropy of the physical properties of the film, reflected in a highly uniaxial magnetic anisotropy (*a*-axis is the in-plane easy axis) and an elastic anisotropy. During cooling from the growth temperature to room temperature, the MnAs lattice constant decreases more strongly than the GaAs lattice constant. Thus, the film may crack above a certain critical thickness of 500 nm [DST+01]. If the *c*-axis of the MnAs lattice is free to relax, it can be expected that crack formation can be avoided, or at least occurs at a much larger thickness. This can be accomplished by growing MnAs under As-rich growth conditions on GaAs (111)B, where the *c*-axis is normal to the surface [KDP02, OME+03, EEDDO02, SKIJ00]. The hexagonal plane of MnAs is parallel to the surface of the substrate with MnAs $[11\bar{2}0]$ (*a*-axis) parallel to GaAs $[1\bar{1}0]$ as illustrated in Fig. 4.6. This way, a planar magnetic anisotropy can be expected. The altered strain state of the film has an impact on the formation of the α-β-stripe structure observed for GaAs (001) and (311)A substrates and also on the phase transition. The different interface morphology also affects the magnetoresistance [ST01], as well as the transport properties [FKD03].

XMCDPEEM is employed to image the magnetic domain structure of the film. In the present orientation of MnAs, the surface is a magnetic easy plane, i.e. no direction is initially preferred. For XMCDPEEM imaging, the photon beam is incident along MnAs $[10\bar{1}0]$ or an equivalent direction. The magnetic image (Fig. 4.7) shows black, white and grey patches which are due to the ferromagnetic α-MnAs, where the magnetization aligns parallel and antiparallel to the incident photon beam, respectively. Gray contrasts are due to the paramagnetic β-MnAs. Besides these three main contrasts there are also mixed contrasts, i.e. black-gray and white-gray (see Fig. 4.7). These mixed contrasts make the system very complicated for evaluating the ferromagnetic phase content of the film as a function of temperature. However, it has to be pointed out that the strain in the system lifts the degeneracy of

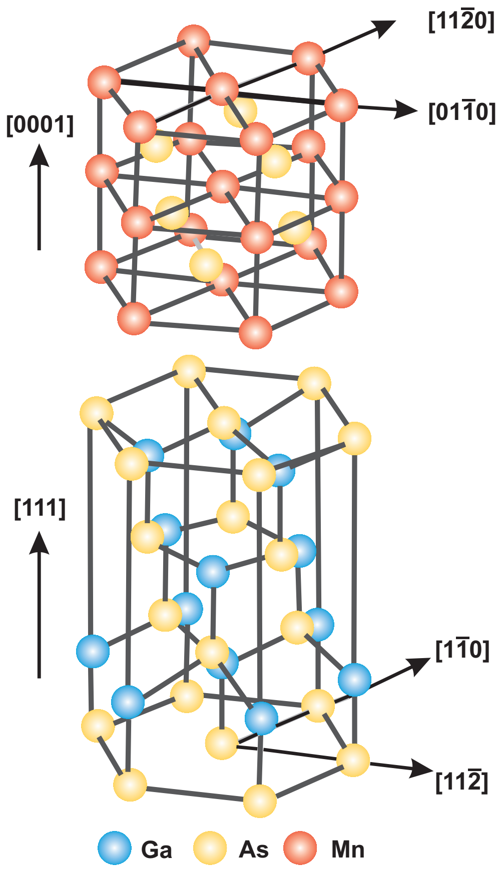

Figure 4.6: Epitaxial relationship for an epitaxial MnAs film on GaAs (111)B.

the in-plane directions, as preferred magnetization directions are observed in the XMCDPEEM images.

We have done temperature-dependent XMCDPEEM measurements from below 18 °C to above 60 °C to get further information about the magnetic ordering of the system, which is shown in Fig. 4.7. At 42 °C the amount of ferromagnetic MnAs is much larger compared to MnAs films on GaAs (001). Even at 50 °C, magnetic contrast is still visible. We found that the phase transition from α- to β-MnAs is completed at 56 °C, i.e. that the transition temperature is increased in these films. Furthermore, X-ray diffraction measurements [JKK^{+}03] show that the temperature range for the phase coexistence is shifted to higher temperatures with a small coexistence regime of 10 °C (40–50 °C). The reported coexistence regime of 10 °C is considerably smaller than the values observed by XMCDPEEM, which shows

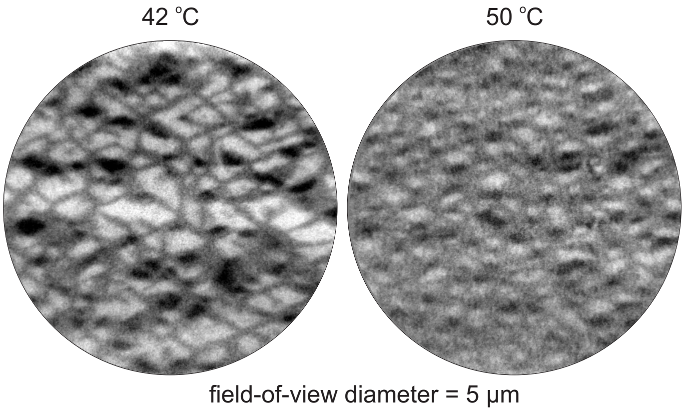

Figure 4.7: Temperature-dependent XMCDPEEM measurement of a 300 nm thick MnAs film on GaAs (111)B. Selected scans for the respective temperatures as measured for a complete heating cycle. For these measurements the photon beam is incident along the MnAs $[10\bar{1}0]$ or an equivalent direction.

a coexistence for the entire measured temperature range of 18 °C to 56 °C. Because of the shift of the phase transition temperature to higher values, it can be concluded that MnAs films on GaAs (111)B are not tensilely strained as in the case of MnAs/GaAs (001). From pressure-dependent studies in the bulk [MKDG69] it is known that high pressures, which are equivalent to compressive strain, lead to lower transition temperatures. The smaller range for the coexistence regime indicates that these films are less strained as compared to films on (001) substrates, which has been concluded from wet-etching experiments [TWDP04] too.

4.3 Influence of the film thickness on the magnetic properties

The film thickness plays an important role for the magnetic properties of MnAs. In case of Fe films it has been observed that, depending on film thickness, the film can have in-plane or out-of-plane magnetic anisotropy [HBvS$^+$02]. Furthermore, the coercive field [DWJ$^+$04], the saturation magnetization [DWJ$^+$04] and the domain size [HBvS$^+$02] also depend on the film thickness. In this Section, the details about the influence of the MnAs film thickness on the magnetic domain structure will be discussed. As it was pointed out in Sect. 4.2, the magnetic domain structure of MnAs/GaAs (001) is more simple compared to the other two orientations, (311)A and (111)B, so we will restrict ourselves to the discussion of films on GaAs (001).

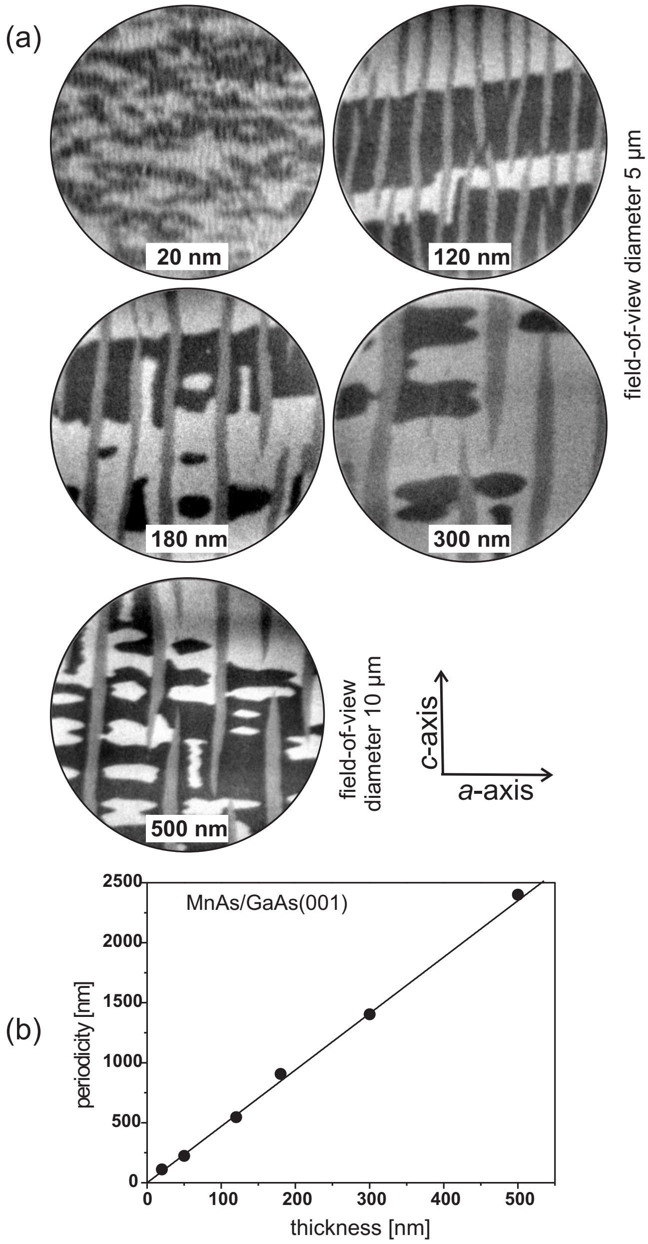

Figure 4.8: Thickness dependence of the domain structure: (a) XMCDPEEM images of MnAs films on GaAs (001) taken at 24 °C, (b) shows the variation of the stripe phase periodicity as a function of film thickness as calculated from the LEEM images.

The investigated films have a thickness of 20–500 nm. Figure 4.8(a) shows XMCDPEEM images at 24 °C for films of various thicknesses, as indicated in the image. For 20 nm thick films, the stripes are quite narrow and in fact this is the thickness for the onset of the ordered stripe phase. Thin gray lines indicating paramagnetic contrast separate two neighboring ferromagnetic stripes. The domains are mostly extended type (I) domains of both parallel and antiparallel magnetization. As the film thickness increases, the stripes get wider.

Figure 4.8(b) shows a linear dependence of the stripe phase periodicity as a function of film thickness as extracted from LEEM images. This observation is consistent with previously performed AFM analysis of MnAs films [KHDP02]. By analyzing a multitude of samples, an empirical expression for the period p [nm] is found as $p = 4.8 \times t$ with t [nm] being the thickness. Consequently, the width of the ferromagnetic as well as paramagnetic stripes increases linearly as the thickness increases for a given temperature. For a thickness of 120 nm, type (I) domains are dominant, but there are also type (II) domains visible. As the stripe width increases further, all three types of domains appear (180 nm thick film). For much larger thicknesses of 300 and 500 nm, more complicated domains are observed. Details on these domains will be presented in Sect. 6.2.

For a 500 nm thick film, the MFM image [Fig. 4.9(a)] shows quite complicated domains. At this thickness, the film cracks because of the build-up strain [DST^{+}01]. The details about the crack formation will be discussed in Sect. 5.3 and Chapter 7. MFM and XMCDPEEM measurements on the very same film with a similar magnetic history revealed differences in the micromagnetic domain configuration. The differences could arise from the different depth sensitivities of the two techniques. XMCDPEEM is a surface sensitive technique (typically some monolayers), whereas a typical MFM depth resolution is of the order of 100 nm [EHon]. Figure 4.9(b) and (c) show MFM scans for a 300 nm thick film where two different domains are highlighted. In the scan (c), the selected domain looks different as compared to the standard type (I) domains shown in (b). The white bar-like contrast in the middle of the stripe is unusual. If we take the existence of two types of domains along the vertical direction into account, e.g. a type (I) domain on top with a thickness of d_1 and a type (II) domain below with a thickness of d_2 [as shown in the sketch (d)], the simulated contrast agrees well with the observed contrast. The details about the contrast simulation will be discussed in the next Section.

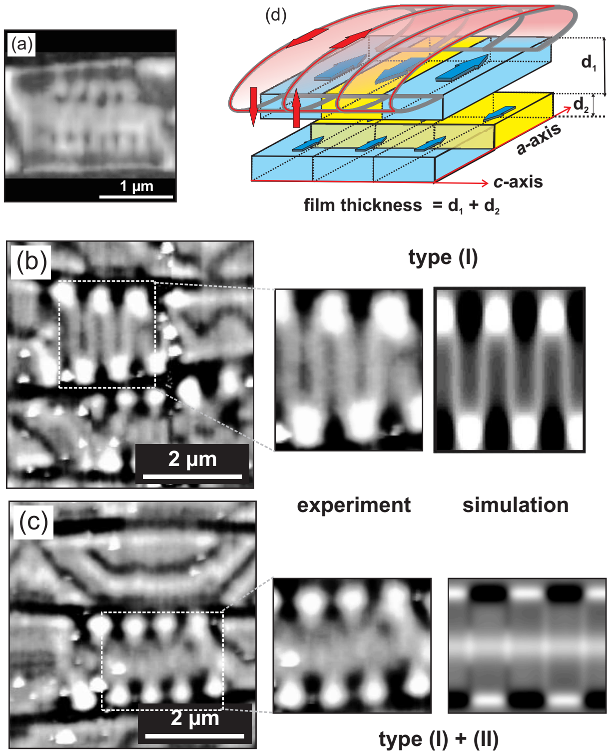

Figure 4.9: Existence of in-depth domains, i.e. in the vertical direction, along with the lateral domains in MnAs films on GaAs (001). (a) MFM image of a 500 nm thick MnAs film, whereas (b) and (c) represent images for 300 nm film thickness. On the right, simulations of selected parts of the MFM measurements on 300 nm thick films are shown. A good agreement is obtained for the measurement shown in (c) when a magnetization distribution with type (I) domains on the surface and type (II) domains below is assumed.

4.4 Comparison of the measured and the simulated MFM contrast

In order to understand the observed domain structure, MFM contrast simulations are carried out. R. Engel-Herbert has simulated the interaction between the tip and the stray field of the sample originating from a given distribution of the magnetic moments [EHon]. Reasonable magnetization distributions are assumed, based on the information from SQUID magnetometry measurements. The stray field is derived with the help of the magnetostatic potential, taking only magnetic dipoles into account and by integrating the elementary dipoles over the sample volume [NPFB00]. It is further assumed that the magnetic dipole strength is constant and uniformly distributed. The direction of the magnetic dipoles is variable, because the total stray field consists of two different contributions — domains with an in-plane magnetization along the easy axis and 180° Bloch walls [cf. Fig. 4.2(b)] exhibiting an out-of-plane magnetization. This results in different distance dependencies of the in-plane and out-of-plane magnetic stray field components in the z-direction (normal to the surface).

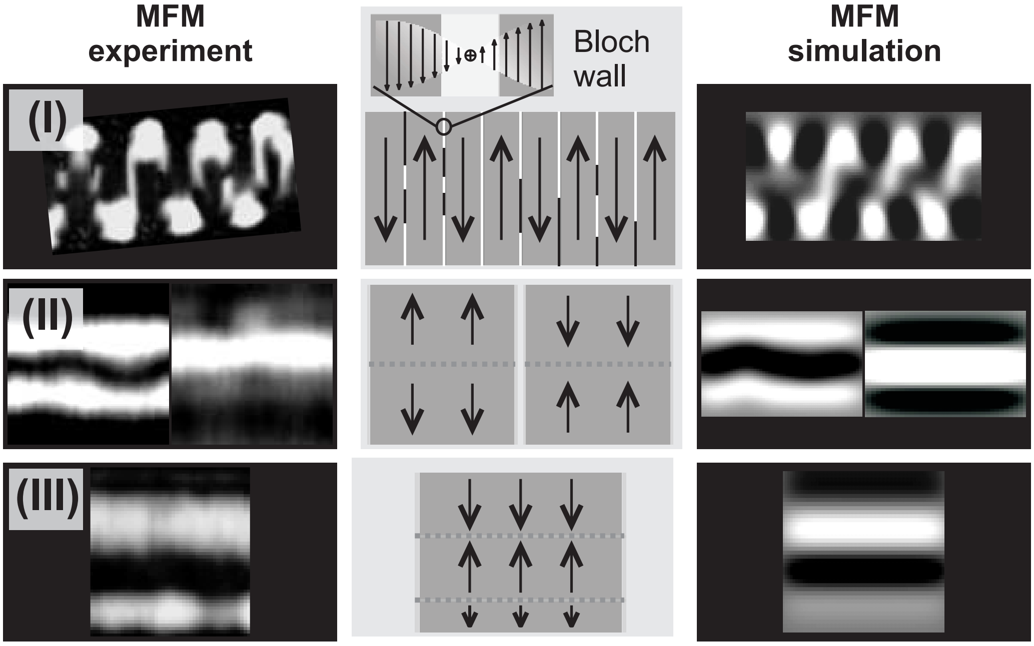

Figure 4.10: Comparison of the measured domain patterns (left column), the most probable domain configurations (middle column), and the simulated MFM contrast (right column) for the common domain types (I), (II), and (III). Black and white lines in the domain configuration pictures indicate 180° Bloch domain walls pointing out-of and into the surface plane, respectively. The dotted lines mark the domain walls between subdomains.

From MFM measurements, it is found that the average width of the domain in the MnAs [0001] direction is 190 nm [MHP$^+$03]. The thickness of the Bloch wall is estimated from MFM measurements and simulations to be roughly 10 nm, as the exchange stiffness A of MnAs is presently not known. Figure 4.10 shows the comparison of the measured MFM contrast and the simulated contrast for the proposed domain configurations (I), (II), and (III). Type (I) domains, where the ferromagnetic stripes are single domain across their width, are typical for the upper and lower limit of the temperature coexistence region of α- and β-MnAs. Very narrow stripes also tend to be single domain along their whole length (in the [0001] direction) of some μm. The alternating type (I) domains presented in Fig. 4.10 are appearing as zig-zag-shaped structure at lower resolution (i.e. higher working distance). At higher resolution, bright areas are visible at the ends of the antiparallelly magnetized areas. In-between the domains, the contrast is due to differently oriented Bloch walls, either rotating the moments through the direction pointing out of or into the surface plane, respectively. This contrast is modeled correctly, as shown on the right hand side of Fig. 4.10 (I), assuming the sketched distribution of magnetic moments. The type (II) domains exist in two variations, as shown in Fig. 4.10 (II), with the in-plane moments pointing towards or away from each other. Interestingly, the addition of a third subdomain during the expansion of the ferromagnetic wire (upon cooling) occurs gradually, and not necessarily abruptly, by rearrangement of the magnetic subdivisions. Therefore, it is reasonable that the proposed type (III) domain configuration, shown in Fig. 4.10 (bottom), has an uneven ratio of the subdomains. It has to be noted that for domain types (II) and (III), no domain wall along the length of the wire is included in the simulations.

Next, we take a closer look at more complex domain configurations, that is, between two type (II), termed (II×II), and between type (I) and (III) domains, termed (I×III). In Figure 4.11, the MFM overview scan shows some of the most prominent domain boundaries. First, the domain boundaries between type (I) domains of antiparallel alignment of the magnetic moments are well resolved in this image. With less lateral resolution, these domains appear as zig-zag-shaped, as explained above. The domain boundaries of type (II×II) and (I×III) are highlighted and marked in the image. Below, two prominent domain boundaries of this type are shown in experiment and simulation. A domain boundary between two evenly divided type (II) domains is quite simple, as only two configurations exist [cf. Fig. 4.10(II)]. The asymmetry in the MFM picture is, however, not due to the tip shape, but due to Bloch walls between the two subdomains as indicated by black and white lines in the domain configuration images of Fig. 4.11. The orientation of the magnetic moments in the 180° Bloch wall, i.e. whether the magnetization is rotating through the out-of-plane or the opposite direction, is obtained by finding the best agreement with the simulated image. Similarly, the Bloch wall orientation is most likely responsible for the tilted appearance of the domain pattern in case of the (I×III) domain boundary [cf. arrow

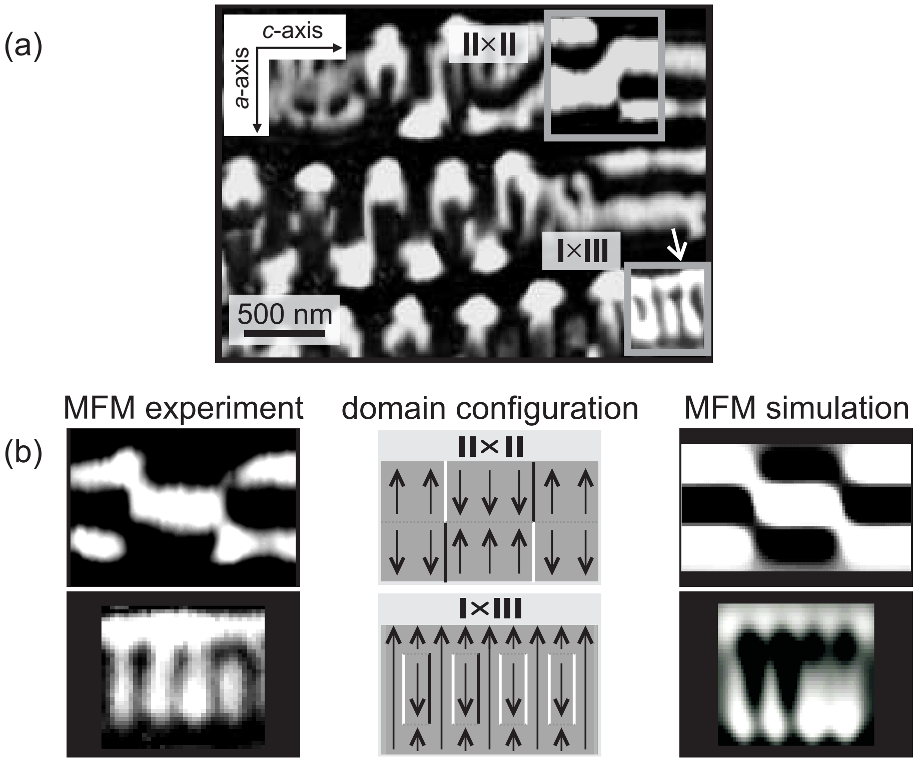

Figure 4.11: MFM overview scan of a sample area with more complex domain boundaries (a). The highlighted areas denote boundaries between two type (II), termed (II×II) and type (I) and (III) domains, termed (I×III), respectively. The comparison between experiment and simulation for the assumed domain configurations is shown below (b).

in Fig. 4.11(a)], contrary to the appearance in the MFM scan as shown in Fig. 4.3. Again, the simulation allows for the extraction of the Bloch wall orientation. Basically, the (I×III) domain boundary is due to a sequence of type (I) and (III) domains with variable-width and length of the subdivisions. The width and length of the individual domains is used as a fitting parameter for the simulation. We are well aware that this magnetic system is quite complex and that the present model is rather limited. However, it allows for the extraction of the most likely domain configurations as a good agreement between the modeled and measured MFM contrast is obtained [EHMN^{+}04].

Chapter 5

Magnetic and Structural Phase Transition

MnAs films on GaAs (001) show a coupled magneto-structural phase transition. Details of this transition were studied by temperature- and field-dependent AFM and MFM. The effect of strain relaxation on the phase transition temperature was studied locally in the vicinity of cracks. Finally, we investigated a metastable state of MnAs that was identified through peculiar domain patterns. All the experimental results that will be presented in this Chapter were performed on MnAs/GaAs (001).

5.1 First-order magnetic and structural phase transition in MnAs films

MnAs films on GaAs (001) exhibit a periodic ridge-groove structure of α- and β-MnAs, respectively. Temperature-dependent X-ray diffraction [KJS$^+$02] and scanning probe microscopy measurements [PRK$^+$02] gave direct evidence for the formation of the ridge-groove structure in a temperature range defined by the temperature where the β-phase starts nucleating in the homogeneous α-phase (on the low temperature side) and the phase transition temperature on the high temperature side. The phase transition temperature is defined as the temperature where the film has completely transformed from the α-phase to the β-phase. It has to be noted that the phase transition temperature in MnAs films is generally not identical with the Curie temperature of the magnetic phase transition. One reason is that strain influences the first-order magneto-structural phase transition. Furthermore, there has been speculation that the true Curie temperature of MnAs is indeed higher than the commonly accepted bulk phase transition temperature of 40 °C

[NHD+05, BR62]. The micromagnetic structure of the ferromagnetic stripes was investigated by temperature-dependent MFM [PHM+03, MHP+03] and recently by XMCDPEEM [BCD+02]. Furthermore, cantilever beam magnetometry (CBM) measurements have revealed the evolution of stress and magnetic properties in the coexistence regime [DPN+03].

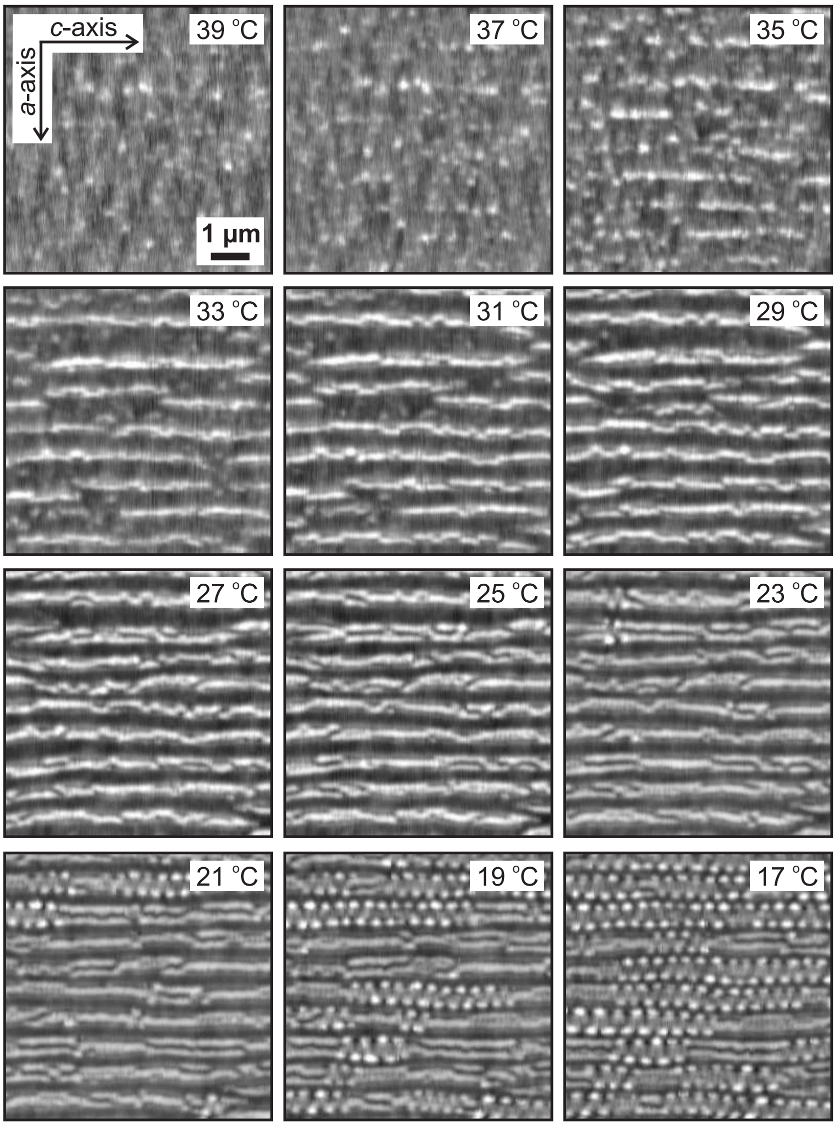

Figure 5.1: Variable-temperature MFM images of a 180 nm thick MnAs film on GaAs (001): Sequence of images taken during the cooling cycle from above transition temperature (45 °C) to room temperature (20 °C) in steps of 2 °C.

Variable-temperature MFM (VT–MFM) is especially useful for studying the evolution and transformation of domains [PHM+03] and, for this particular system, the interplay between structural and magnetic properties. The following measurements (7×7 μm^2 scans) were performed on the same sample spot [cf. Fig. 5.1]. For preparing identical starting conditions for the temperature cycling experiments, the sample was first heated well above the transition temperature in order to erase ferromagnetism. Then, it was gradually cooled down to below room temperature in steps of 2 °C. No difference was found when the heating and cooling steps were performed at different rates (with the employed temperature stage [MMR]). At every temperature step, the system was allowed to stabilize thermally for some minutes and then two MFM and two topography scans were taken. The time difference between two successive temperature points was $\approx$ 14 minutes. Figure 5.1 shows MFM images, taken during a cooling sequence spanning from 39 °C down to 17 °C. In general, for a 180 nm thick film for temperatures around room temperature and below, primarily type (I) domains are found. The width of the domains (in the [0001] direction) is 190 nm, independent of the temperature [MHP+03]. With decreasing β-MnAs content, i.e. vanishing grooves, the interaction of the domains across the ridges increases and the magnetic areas align in a dipolar fashion. Above room temperature, i.e. when the ferromagnetic ridges are narrowing, the number of type (I) domains decreases and type (II) (elongated) domains dominate. Above $\approx$ 32 °C, another elongated domain type completely takes over, that condenses into ferromagnetic dots which finally disappear at the phase transition temperature.

At 39 °C, a dot-like magnetic contrast is found, presumably due to α-MnAs enclosures. As the sample is cooled down, the number of these dot-like contrast features increases. Below 35 °C, chain-like elongated structures begin to form. Between 33 °C and 32 °C, these elongated chain structures transform into ordered ferromagnetic stripes along MnAs [0001]. Upon further cooling, the stripe width increases and the structural pattern gets more ordered [MHP+03]. At 17 °C, no defects are visible in the ridge-groove structure (on this scale). The magnetic contrast shows distinct types of magnetic domains that dominate in certain temperatures ranges. At higher temperatures, elongated type (II) domains are visible, whereas below 27 °C, elongated type (III) domains are more common. Below 23 °C, the above mentioned type (I) domains start appearing, and grow at the cost of the elongated domains upon further cooling.

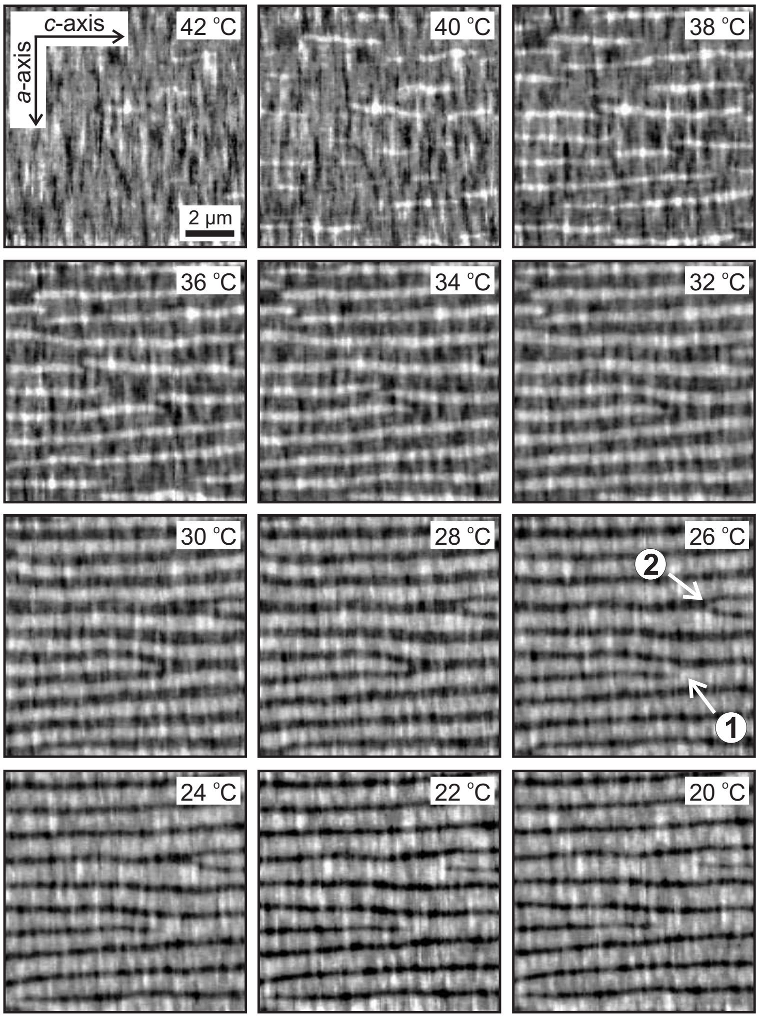

Figure 5.2: Variable-temperature AFM images of a 180 nm thick MnAs film on GaAs (001): Sequence of images taken during the cooling cycle from above transition temperature (45 °C) to room temperature (20 °C) in steps of 2 °C. The areas labeled '1' and '2' show a branching point and a stripe termination of the ordered stripe array, respectively.

At each temperature, both MFM and topographic scans were taken in order to see the correlation of topography and magnetic contrast. For lower α-MnAs content, the feedback of the MFM gets increasingly unstable and one starts picking up more topographic features. So, in order to be sure to measure the pure topography, all MFM measurements cycles were followed by a contact-mode AFM cycle, as shown in Fig. 5.2). It has to be noticed that for both the VT–MFM and VT–AFM measurements the magnetic history is the same.

In general, magnetic contrast is only observed on the ferromagnetic α-MnAs stripes that appear as ridges in the topography images. Growth-induced features (cf. Fig. 5.2, 42 °C), oriented along the a-axis direction perpendicular to the stripes, have no apparent influence on the magnetic structure. During the cooling cycle, the formation of the α-phase within the β-matrix starts randomly leading to an irregular distribution of ridges at temperatures close to the transition temperature. With increasing α-phase content of the film (at a temperature of 36 °C), an extended stripe structure develops that shows locally a high degree of order. Below 30 °C, the ferromagnetic stripes exhibit a remarkable regularity. There are imperfections in this stripe structure, e.g. Y-shaped branching points (labeled '1' in Fig. 5.2, 26 °C) and terminations of the ferromagnetic stripes (labeled '2' in Fig. 5.2, 26 °C), that resemble edge dislocations and introduced lattice planes in a two-dimensional lattice [DKH$^+$03]. The imperfections are due to the kinetics of the phase transition, as the α-phase starts forming randomly in the β-matrix and a certain degree of disorder is left behind after the formation of the regular stripe array.

5.2 Temperature dependence of the magnetic and structural properties of the MnAs phases

The magnetic as well as the structural properties of the film show a hysteretic behavior with temperature. For a 180 nm thick MnAs film, the temperature difference between the disappearance of the ferromagnetic stripes upon heating and the reappearance upon cooling was determined to be 2 °C. The fraction of the α-phase is larger when the sample has been heated to reach the respective temperature than when it has been cooled in the temperature cycling process.

At 31 °C, the MFM images (top and bottom of Fig. 5.3) show a different domain arrangement depending on the temperature history. In the heating sequence measurement, type (III) domains are the dominant domain configuration, whereas for the cooling sequence, type (II) domains are typical. The α-phase contribution is larger during heating. Also, the ferromagnetic stripes are well-connected. During cooling, when less α-MnAs is present, the much

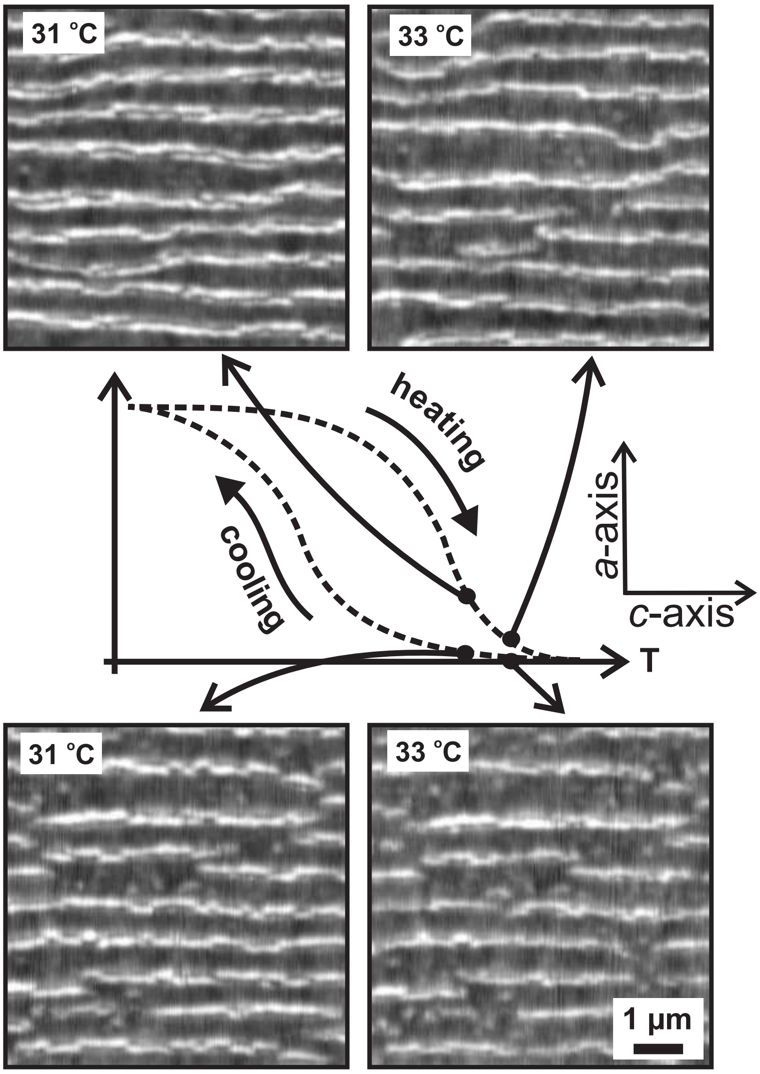

Figure 5.3: Temperature hysteresis of a 180 nm thick MnAs film on GaAs (001) following the heating and cooling cycle as shown in the sketch in the middle.

shorter ferromagnetic stripes are less ordered. For comparison, a qualitative sketch of the temperature hysteresis of the α-to-β-phase ratio is shown in the middle of Fig. 5.3. Contrary to the measurements at 31 °C, the images taken at 33 °C show no significant hysteretic behavior.

Figure 5.4 shows a comparison of the ferromagnetic α-phase content as a function of temperature obtained by different techniques. X-ray diffrac-

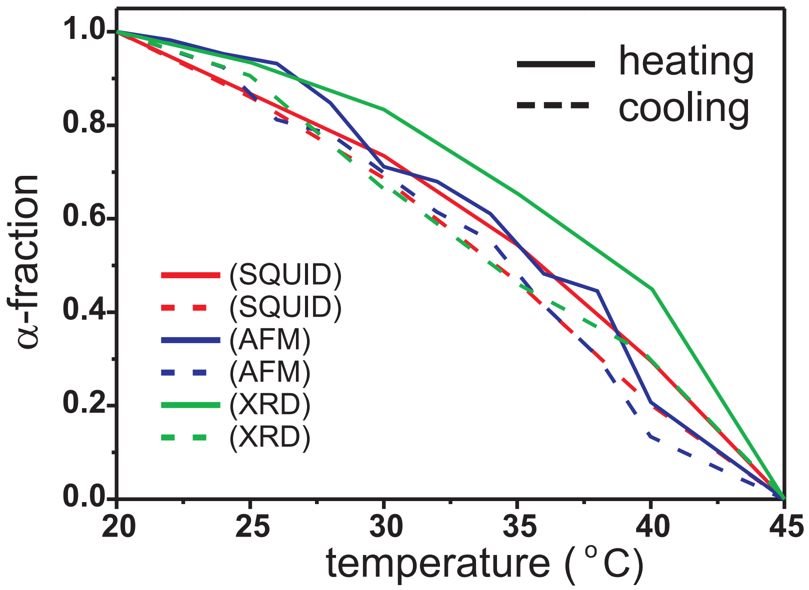

Figure 5.4: Comparison of the temperature hysteresis of the α-fraction of a 180 nm thick MnAs film on GaAs (001) measured by different techniques. Solid and dotted lines are for the heating and cooling cycles, respectively.

tion data [KJS$^+$02] show a larger hysteresis compared to AFM and SQUID magnetometry. However, there exist some irregularity in the measured AFM data, which can be attributed to the error in estimating the α-phase content.

In order to obtain quantitative information about the α- and β-MnAs phase content and the local distribution of the phases as a function of temperature, we performed and analyzed XMCDPEEM measurements. For the analysis of the α-phase content, the areas occupied by individual domains with parallel (white contrast) or antiparallel (black contrast) magnetization are calculated by following two different analysis procedures, namely histogram analysis and particle area analysis. It was observed that for a particular set of data, the histogram analysis overestimates the α-phase content. On the other hand, for the particle analysis it was difficult to consistently set the threshold value for each contrast range. Besides these problems there are striations resulting from synchrotron light beam inhomogeneities which result in a large error for a straight-forward analysis. Now, the details of the image analysis will be discussed.

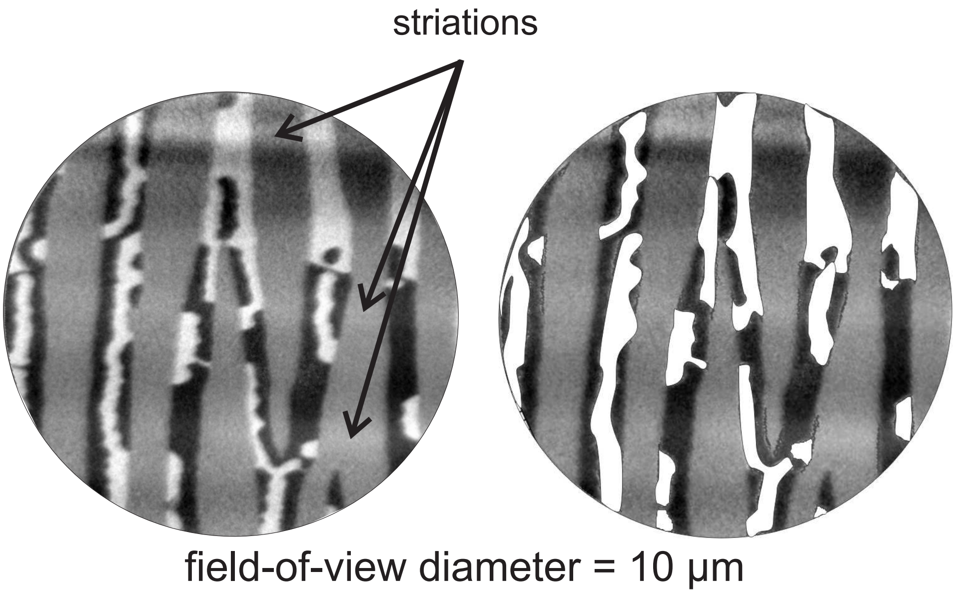

Figure 5.5: XMCDPEEM image of a 500 nm thick MnAs film on GaAs (001) at 34 °C. The left hand side image shows striations resulting from the inhomogeneity of the synchrotron light beam indicated by arrows. The right hand side image shows the areas parallel magnetization (white contrasts) selected for the image analysis.

For obtaining XMCDPEEM images, two measurements are taken at each temperature at positive and negative helicity of the photon beam, respectively. The XMCDPEEM contrast C_{XMCDPEEM} is the defined as:

$$C_{\mathrm{XMCDPEEM}} = (I_+ - I_-)/(I_+ + I_-)\,, \tag{5.1}$$

where I_+ and I_- are the secondary electron intensities due to left and right circular polarized light, respectively. The images are then processed in various steps with the help of a macro using the image analysis software Igor Pro [Igo]. Among the procedures that are necessary to obtain the XMCDPEEM image and which are described in detail in Ref. [Mac], two will be discussed below. The drift correction is an important step in the data processing, as a typical measurement takes about 2.5 minutes, with a pause of 0.5 minutes during the changing of the polarity of the synchrotron beam. For a typical XMCDPEEM contrast, it is advantageous to calculate the image drift of the first derivative of the data. First, the edges in the images are found and the drift vector is calculated via the 2D-correlation of the positive and negative helicity images. The drift is then removed from one of the images before the

XMCDPEEM contrast C_{XMCDPEEM} is calculated. As a next important step, a region of interest is selected (which is slightly smaller than the detector area) and the effects of inhomogeneous illumination are partially corrected. For this purpose, the background of the XMCDPEEM image (third order polynomial fit) is removed.

For a precise analysis of XMCDPEEM images, the inhomogeneities of the synchrotron beam on the sample surface on the micrometer scale have to be dealt with. Figure 5.5 shows these beam inhomogeneities or striations in a XMCDPEEM image of a 500 nm thick MnAs film on GaAs (001) at a temperature 34 °C. On the left hand side of the image, the striations are indicated by arrows. For calculating the areas of white contrast it is difficult to decide on a threshold contrast, as the striations also lead to white contrast regions. In order to perform a consistent particle analysis, the areas affected by the beam striations are carefully subtracted from the total area. On the right hand side of the image, the selected white contrast areas are shown, taking care of the striations. The sum of the areas occupied by white and black contrast give the total ferromagnetic α-content. For calculating the β-phase content, the area occupied by the α-phase is subtracted from the total film area.

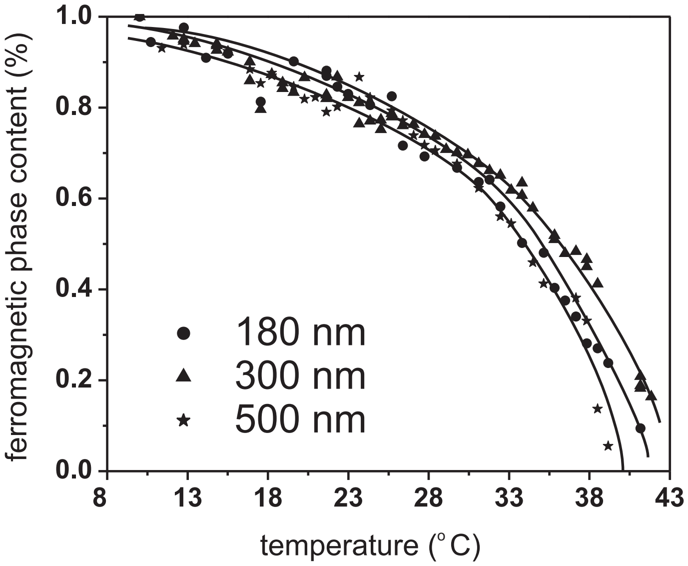

Figure 5.6: Variation of the α-phase content as a function of temperature obtained from XMCDPEEM measurements for three different film thicknesses (180 nm, 300 nm and 500 nm).

The α-phase content in the α-β-coexistence regime from 10 °C to roughly 40 °C is steadily decreasing with increasing temperature. The film thickness has only a minor influence on the temperature dependence of the α-phase content. The measurements for the three investigated thicknesses only differ at higher temperatures close to the phase transition. Figure 5.6 shows the ferromagnetic α-phase content as a function of temperature for films of various thicknesses (180 nm, 300 nm and 500 nm). The data points are obtained by analyzing XMCDPEEM temperature cycles. As the field-of-view for the measurements at different thicknesses has a diameter of 10 μm for the 500 nm thick film and 5 μm for the 180 and 300 nm thick films, local fluctuations of the phase composition may lead to sampling size-induced deviations.

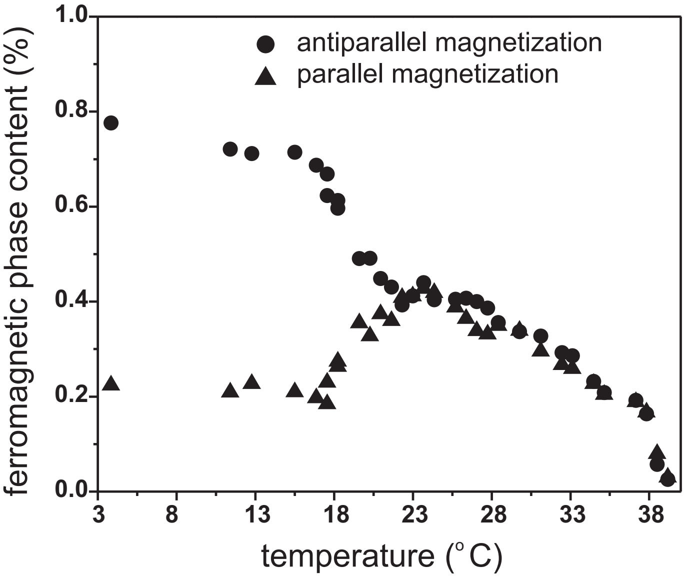

Figure 5.7: Plot of the parallelly and antiparallelly magnetized fraction of the ferromagnetic areas of a 500 nm thick MnAs film on GaAs (001) as a function of temperature.

If one performs the analysis of the α-phase content starting from the completely demagnetized state of the samples, one can expect an equal fraction of parallelly and antiparallelly magnetized areas (with respect to the easy magnetization axis). In the XMCDPEEM set-up, one can not prepare a completely demagnetized state, i.e. that locally an effective net magnetization is observed. Figure 5.7 shows a plot of the magnetization contributions (the sum of these two gives the total ferromagnetic phase content) as a function of temperature for a 500 nm thick MnAs film on GaAs (001). For this measurement, the heating cycle is started at 3 °C and went up to above 40 °C. At lower temperatures, there is a net antiparallel magnetization which decreases slowly as a function of temperature up to 18 °C. At higher temperatures, the slope of the magnetization curve increases until both magnetizations compensate each other at around 22 °C. Above 22 °C, the curves for both magnetization directions follow the same trace and finally vanish at around 40 °C. From this observation it can be concluded that at a temperature of 22 °C it becomes energetically favorable for the individual magnetic stripes to demagnetize. Below this temperature, the inter-stripe coupling via the stronger dipole-dipole interaction favors the parallel orientation of the domains along the *a*-axis direction. This behavior can be observed in the corresponding XMCDPEEM images shown in Fig. 6.10.

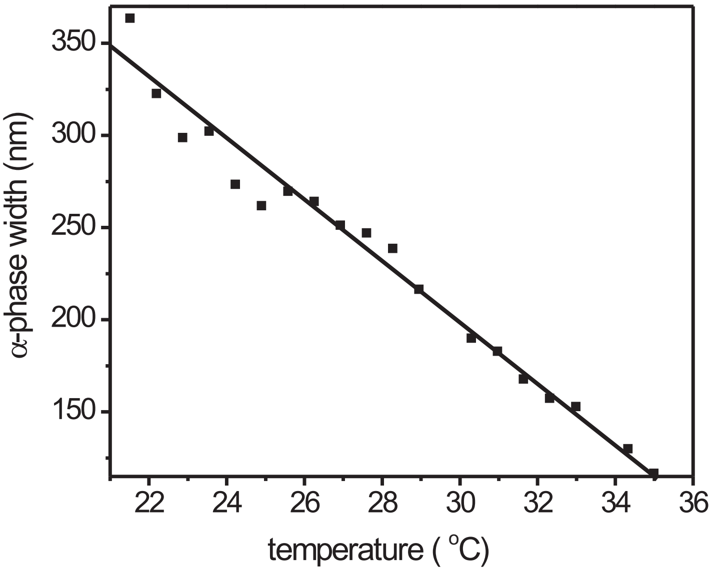

Figure 5.8: Variation of the α-stripe width as a function of temperature for a 120 nm thick MnAs film on GaAs (001).

Next, we analyze the ferromagnetic stripe width and separation. Figures 5.8 and 5.9 show the average α-phase stripe width and the average distance between two stripes (β-phase stripe width) as a function of temperature following a heating cycle for a 120 nm thick MnAs film on GaAs (001). The data are obtained by averaging the width and distance over several stripes in

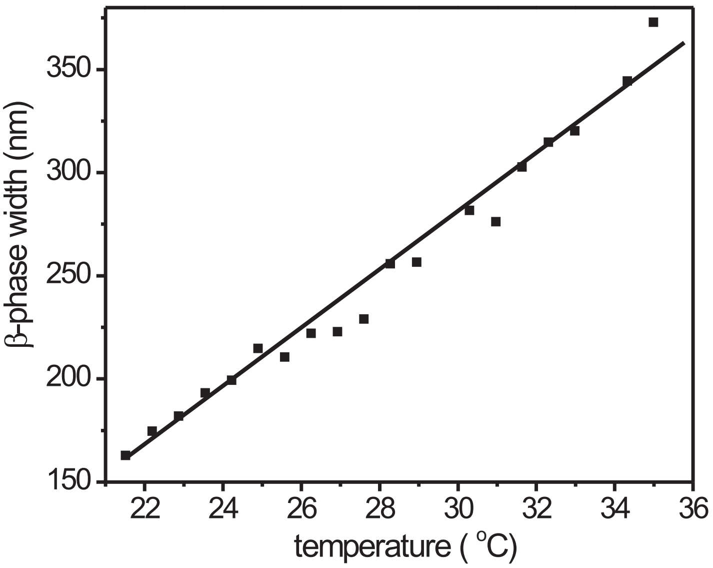

Figure 5.9: Variation of the β-phase stripe width as a function of temperature for a 120 nm thick MnAs film on GaAs (001).

strongly uniform stripe phase areas. The width of a stripe is defined by the full width at half maximum (FWHM). The α-phase stripe width decreases linearly with temperature, starting from about 350 nm for 21 °C and reaching to 120 nm at 35 °C. Similarly, the distance between the α-stripes (β-phase stripe width) is increasing from 170 nm at 21 °C to 350 nm at 35 °C. It has to be noted that for this measurement the starting temperature is higher than room temperature. Therefore, the stripe phase periodicity (i.e. the width of a β-stripe plus the width of a α-stripe) is approximately 10 % less than the one shown in Fig. 4.8(b).

5.3 Effect of strain on the phase transition temperature

The local effect of strain on the structural and magnetic properties of MnAs on GaAs (001) is studied. By performing temperature-dependent measurements of the topography and the magnetic contrast by AFM and MFM, the influence of local strain on the transition temperature is imaged with high lateral resolution in the temperature range from 20 °C to 45 °C.

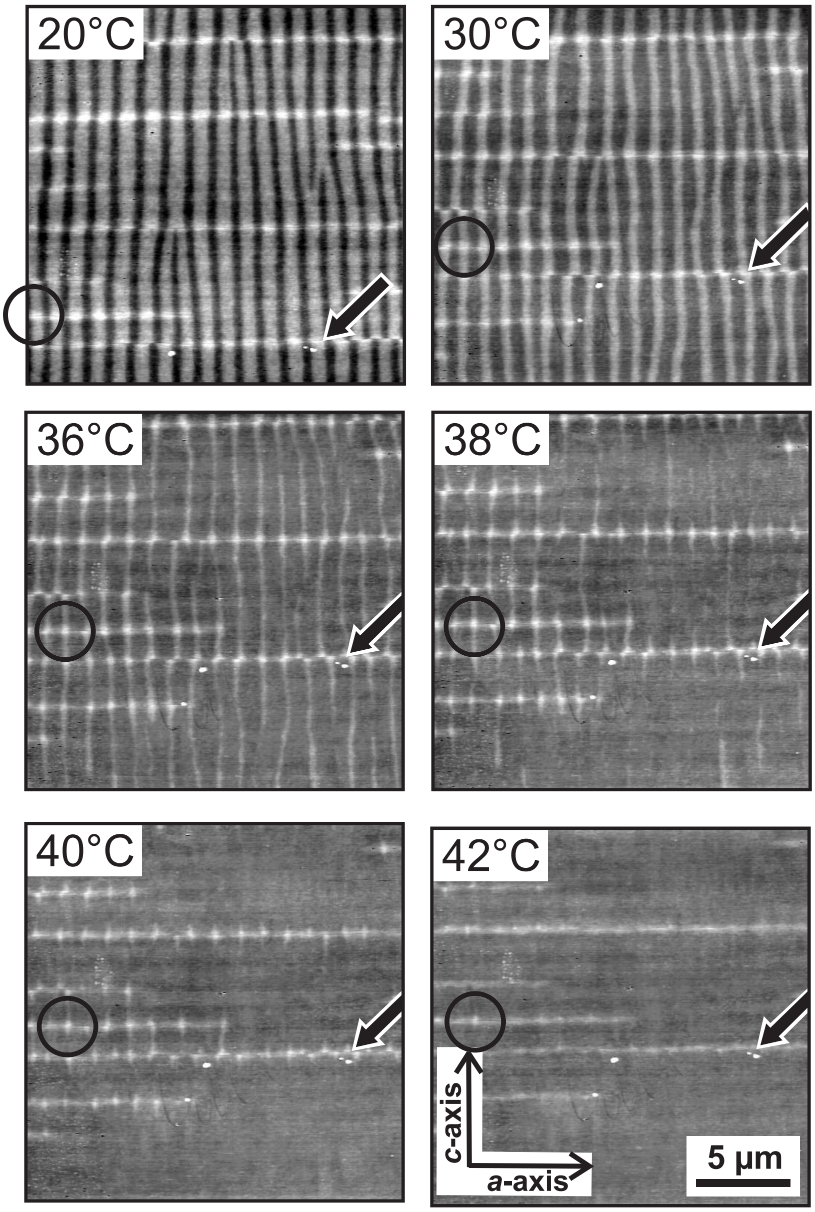

Figure 5.10: Variable-temperature AFM of a cracked 180 nm thick MnAs film on GaAs (001).

By wet-chemical etching of MnAs films at room temperature, the strain is relieved by the formation of cracks running solely along the *a*-axis direction [TWR$^+$03]. Details about the etching and crack formation can be found in Chapter 7. In Figure 5.10, representative topography scans (20×20 μm^2)

of the heating sequence ranging from 20 to 42 °C in areas showing a large number of cracks are shown. Circles and arrows indicate the same spots on the film, as the scan window is drifting upon heating. From 20 °C to above 30 °C, the α-stripes become narrower. However, the stripes are still continuous forming a regular array. Around 36 °C, the stripes decompose into smaller segments that extend from the cracks. Above 40 °C, the stripe segments shrink into isolated features that are pinned by the crack line and even persist at 42 °C. Looking in more detail at the cracks in this temperature range reveals that the surface appearance of the cracks, i.e. their width and length, is not affected by thermal cycling.

To investigate the stripe configuration of the cracked MnAs films in more detail, we performed comparative MFM measurements at 20 °C and 37 °C, i.e. just below the phase transition temperature. Figure 5.11 shows $7 \times 3.5\ \mu\text{m}^2$ AFM and MFM images of two different regions of the sample: a cracked and a strained, i.e. pristine area. The upper half-images show the topography of the respective region and the lower half-images the corresponding magnetic contrast. At 20 °C, the α-β-stripe structure is still predominant and cracks running perpendicular to the stripes are clearly visible in Fig. 5.11(a). The magnetic contrast displays complex features in the ferromagnetic α-stripes. The domain patterns in the cracked and the uncracked areas show no significant differences well below the phase transition temperature.

At 37 °C, just below the phase transition temperature of this particular film, the topography as well as the magnetic scans show surprising differences between the two areas. In the topography of the uncracked film, hardly any α-stripes are visible. In the cracked film, on the other hand, the stripe structure is still present (as well as the perpendicularly oriented cracks). The crossing points of both patterns stick about 6 nm out of the surrounding β-phase material, giving rise to a 2-dimensional network of protrusions. The corresponding magnetic measurements at 37 °C show almost no contrast on the uncracked surface. In case of the cracked surface area, the α-stripes narrow with increasing temperature and the magnetic domain configuration is less complex compared to 20 °C. The in-plane domains extend over the whole stripe in the (a-axis) direction and lead, depending on the parallel or antiparallel alignment of the moments, to segments of bright contrast on either edge of the stripes [cf. Fig. 5.11(c)].

The comparison of the AFM and MFM scans at 20 °C and 37 °C leads to the conclusion that the α-phase persists in the vicinity of the cracks at

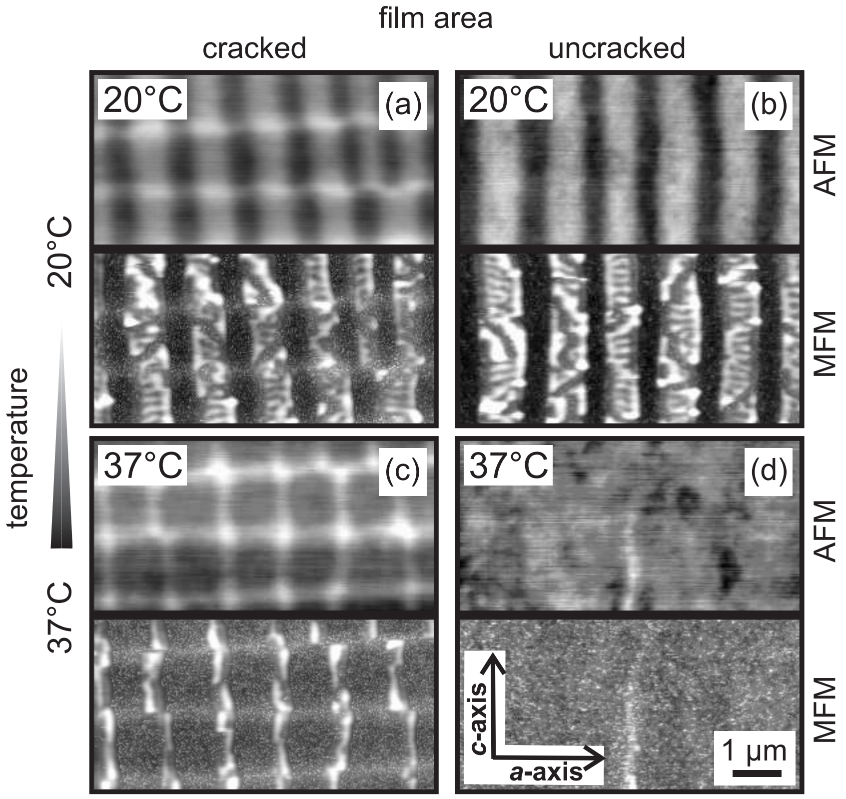

Figure 5.11: Variable-temperature AFM and MFM of locally cracked and uncracked areas of a 180 nm thick MnAs films on GaAs (001).

elevated temperatures (see Fig. 5.10, 40 °C), whereas it disappears in the uncracked areas of the film. According to the MFM scans, the remaining stripes are indeed ferromagnetic α-MnAs with an increased phase transition temperature. From measurements at different temperatures, we estimate a local increase of the phase transition temperature of the order of 5 °C, i.e. almost reaching the α-β-phase transition temperature of bulk MnAs.

The shift of the transition temperature in the vicinity of the cracks can be correlated with the local change of the strain state of the film. According to previous studies of bulk MnAs, the transition temperature decreases under pressure [MKDG69], i.e. with increasing compressive strain, which is attributed to a strain-dependent magnetic exchange energy [BR62]. Whereas the misfit strain is relaxed to a large extend at the MnAs growth temperature of 250 °C [STDP99], a tensile strain arises upon cooling to room temperature since the thermal expansion coefficients of MnAs [WR54] are about one order

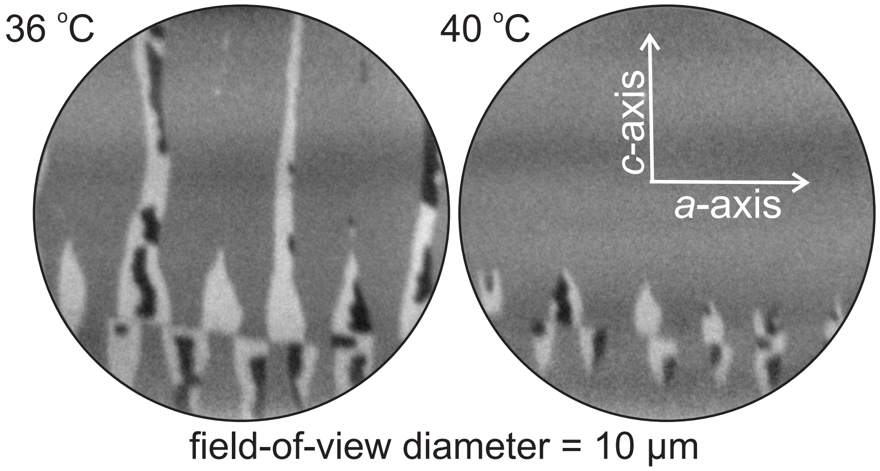

Figure 5.12: Temperature-dependent XMCDPEEM measurements on a 500 nm thick MnAs film on GaAs (001) showing the existence of ferromagnetic material in the vicinity of the cracks.

of magnitude larger than those of the GaAs substrate. In the course of the α-β-phase transition the equilibrium lattice spacing abruptly increases solely along the a-axis, leading to a net compressive stress in the α-phase [WR54]. In the coexistence region, the strain is reduced by the formation of the periodic α-β-stripe pattern. In the perpendicular direction (c-axis), on the other hand, no comparable strain relaxation mechanism exists. This also limits the maximum thickness of the epitaxial MnAs films to roughly 500 nm, above which as-grown films already exhibit cracks aligned in the a-axis direction [DST+01], as shown in Fig. 5.12. As the MnAs film expands in the vicinity of the cracks in height by about 4 nm, and as the distortion of the α-stripe decays over about 500 nm in the c-axis direction away from the crack, the strain in the MnAs film is relaxed in both the c-axis and the a-axis directions. Therefore, the partial strain relief owing to the introduction of cracks can be held responsible for the shift of the transition temperature towards the value of unstrained bulk MnAs.

5.4 Field dependence of the phase transition

In the bulk phase, MnAs shows a strong increase in magnetoresistance [MRR+03], a giant magnetocaloric [WT01, GCdC+04] and magnetoelastic effect [CWMS99], as well as a structural transformation as a result of the applied magnetic field

[IKWW03]. There is indeed experimental evidence that it is possible to influence the phase transition of MnAs by varying external parameters. For example, the phase transition temperature of bulk MnAs is reduced when the external pressure is increased [MKDG69]. Applying strong magnetic fields, on the other hand, leads to an increase of the bulk phase transition temperature [MRR+03, IKWW03]. Also for MnAs films on GaAs (001), there is evidence for an increased phase transition temperature [IKS+05, IKS+03]. The coupled structural and magnetic phase transition of MnAs films is the key for extending ferromagnetic order to higher temperatures by either changing the strain state of the films (Subsect. 4.2.2) or by applying magnetic fields [NHD+05]. The influence of the magnetic field on the phase transition is studied by heating the sample from the striped phase at 22 °C to above the bulk phase transition temperature (≈ 40 °C) in a constant field of 500 Oe.

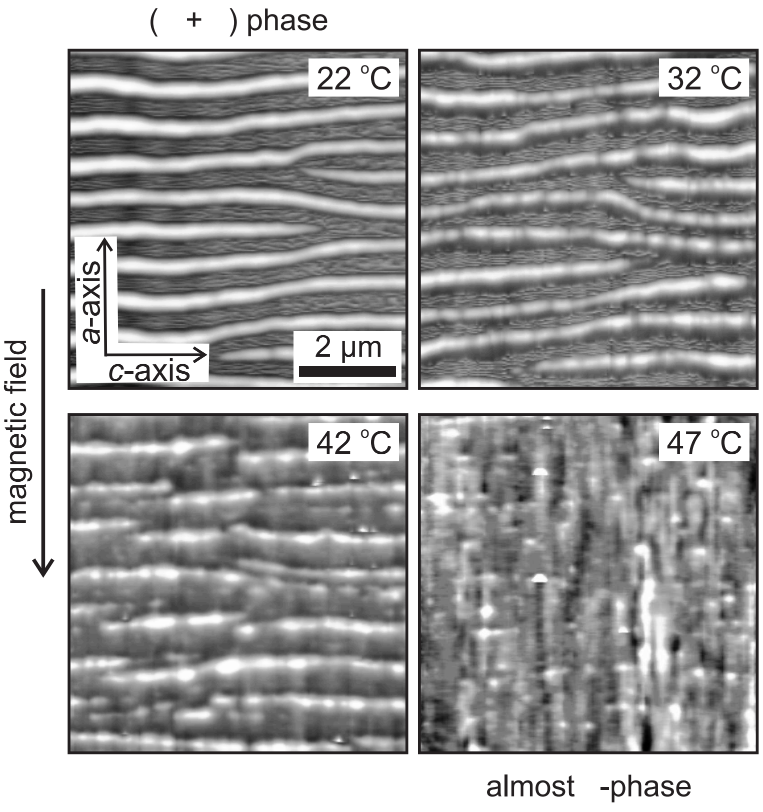

Figure 5.13: Variable-temperature MFM images of a 180 nm thick MnAs film on GaAs (001) taken at a constant field value of 500 Oe: Selected images taken during the heating cycle from room temperature (22 °C) to a temperature (47 °C) above the bulk transition temperature (40 °C).

Figure 5.13 shows selected MFM scans of a 180 nm thick MnAs film on GaAs (001) taken at a constant applied field of 500 Oe. The field is applied along the easy axis (a-axis) of the film as indicated by the arrow in the figure. At 22 °C, which is in the coexistence regime, all the ferromagnetic stripes are in a single domain state, i.e. the magnetization is saturated in accordance with macroscopic magnetization measurements [NHP$^+$03]. As the temperature is increased in a constant magnetic field, the ferromagnetic stripes start breaking up around 40 °C. This means an increase of the break-up temperature of the stripes of roughly 10 °C compared to the 30 °C measured in the zero-field VT–MFM measurements (Fig. 5.1). By heating the sample above the phase transition temperature, most of the ferromagnetic material is transformed into the paramagnetic phase. At 47 °C, i.e. some degrees above the bulk phase transition temperature of MnAs, the ferromagnetic stripes have vanished. However, small spots yielding MFM contrast remain visible. At this temperature, the α-MnAs content is small, therefore the feedback of the MFM gets increasingly unstable and one starts picking up predominantly topographic features.

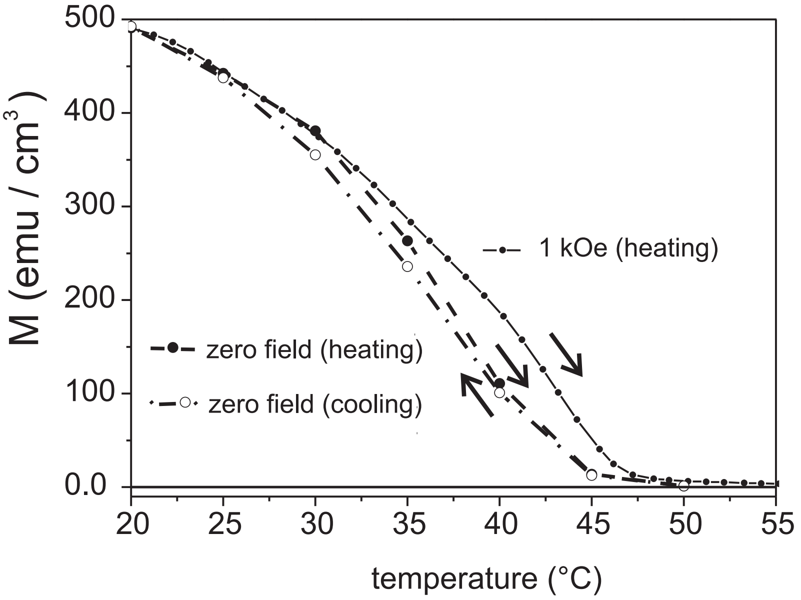

Figure 5.14: Temperature dependence of the magnetization M(T) of a 180 nm thick MnAs film on GaAs (001) measured by SQUID magnetometry at zero field (both heating and cooling) and at 1 kOe (heating). Magnetic field is applied along the easy magnetization axis (a-axis).

The stabilization of ferromagnetic long range order at higher temperatures in an applied magnetic field has its origin in the first order nature of the phase transition. It has already been pointed out by Guillaud [Gui51] that the extrapolation of the temperature dependence of the spontaneous magnetization should lead to a disappearance of the magnetization at about 130 °C. Thus, parts of the paramagnetic phase can be transformed back to the ferromagnetic phase by applying an external magnetic field. At 50 °C and an external magnetic field of 50 kOe, almost 50 % of the magnetization, compared to the saturation value at 0 °C, is recovered [NHD$^+$05].

The increase of the phase transition temperature is also observed on a macroscopic scale by SQUID magnetometry measurements. Figure 5.14 shows the temperature dependence of the magnetization $M(T)$ for an applied of 1 kOe and, for comparison, for zero field. The measurements at an applied field of 1 kOe shows higher magnetization values below the phase transition temperature as compared to the zero field measurements. It has to be noted that the $M(T)$ curves show a temperature hysteresis, i.e. a different magnetization depending on whether the measurement is taken during heating or cooling, independent of the applied field. The hysteresis is most prominent for zero field. The zero field measurements show a temperature hysteresis in the temperature range from 25 to 42 °C.

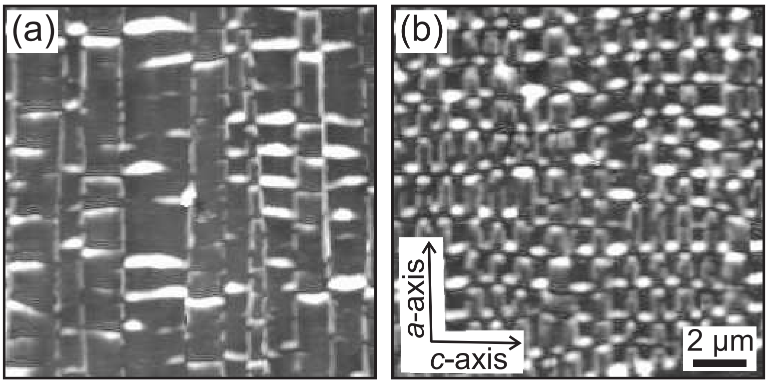

Figure 5.15: MFM images measured at room temperature for a 180 nm thick MnAs sample on GaAs (001): Sample is taken out of refrigerator and the MFM scan is performed at room temperature (a). (b) Shows the MFM image of the same location after a heating cycle, when the sample is heated above the transition temperature and then cooled down to the measurement temperature.

Magnetic films often show metastable features which are either an effect of time, temperature or the magnetic field. In MnAs films, a metastability of the domain structures is observed for samples that were stored for extended times in a refrigerator.

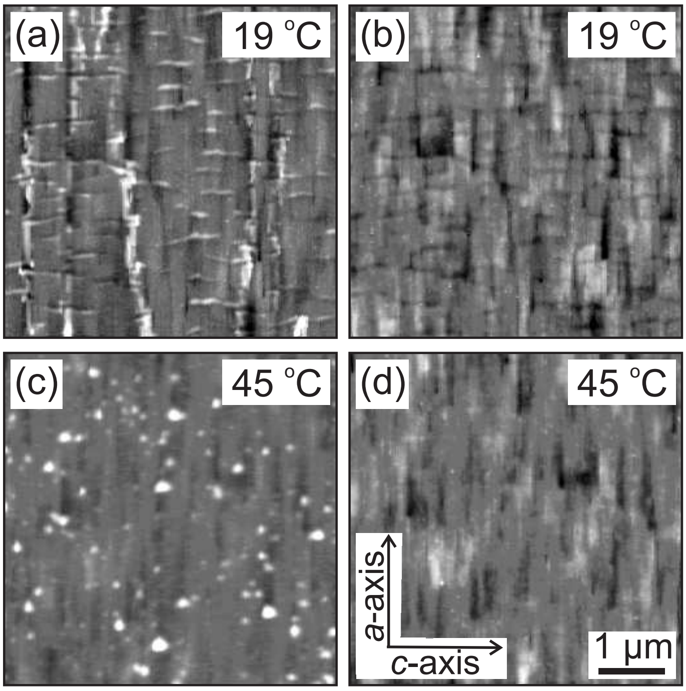

Figure 5.16: SPM images of a 60 nm thick MnAs film on GaAs (001): (a) and (c) are the MFM images, where as (b) and (d) are the corresponding AFM images taken at 19 °C and 45 °C, respectively.

Figure 5.15 shows measurements on a 180 nm sample. This sample was kept in the refrigerator for more than three months. On the day of the measurement, the sample was taken out of the refrigerator and kept at room temperature for 2-3 hours before the measurements are performed. Figure 5.15(a) shows a first MFM scan of the sample. It is clear that the domains are unusual compared to the previously observed patterns in the film of the same thickness. There are features along the easy axis (a-axis) direction that are clearly visible, which look like a continuation of the domain walls across many ferromagnetic stripes. The film behaves like the type (I) domains in single domain state. These structures last for many days. In order to demonstrate the effect of temperature, the sample is then heated to above the transition temperature and cooled down to the room temperature again. The MFM scan in Fig. 5.15(b) shows the typical type (I) domains.

Furthermore, a thinner film (60 nm) is studied, where the stripes are very thin. Figure 5.16 shows selected AFM and MFM images of the heating cycle. Similar features along the *a*-axis are also observed for this film [cf. Fig. 5.16(a)]. The film is also in a striped single domain state. The corresponding topographic scan (b) shows growth-related elongated defects along the *a*-axis direction. However, this features are not correlated with the micromagnetic domain structure. By increasing the temperature, the defects vanish at around 30 °C (not shown). Increasing the temperature further, dot-like magnetic contrast is seen at a higher temperature compared to the normal film, as shown in (c), where (d) presents the corresponding topographic contrast. It has also been found that the ferromagnetic content at higher temperatures is larger compared to a "standard" film of the same thickness. Finally, it can be concluded that MnAs films do show some metastabilities which can be removed by temperature cycling.

Chapter 6

Field and Temperature Dynamics of Magnetic Domains

So far, the effect of temperature (changing the width of the ferromagnetic stripes) and the influence of an external magnetic field on the magneto-structural phase transition was discussed. Understanding the evolution of the magnetic domain structures in an external applied field gives important information about the stability of the domains, as well as the magnetization reversal process [SUL$^+$03]. Furthermore, the growth of domains depending on the stripe width as well as the nucleation of domains will discussed in this Chapter.

6.1 Micromagnetics of uniaxial MnAs wires

The strong uniaxial anisotropy, as well as the wire-like periodic arrangement of the ferromagnetic phase separated by the paramagnetic phase, is a true realization of structured microwires. So far, the micromagnetic domain structure of MnAs films magnetized *ex situ* was investigated by Schippan *et al.* [SBD$^+$00]. In order to study the influence of the magnetic field on the domain structure of MnAs wires, an external field was applied *in situ* along the easy axis (a-axis) direction. Figure 6.1 shows a series of MFM images acquired at different field values as indicated in each image. For these measurements, a 180 nm thick MnAs film was used. The measurements were performed first at zero field (in the demagnetized state) and then the field was slowly increased in steps of 10 Oe until all stripes were in the single domain state which occurs at 150 Oe. At 0 Oe, the film shows different domain structures as explained in Chapters 4 and 5.

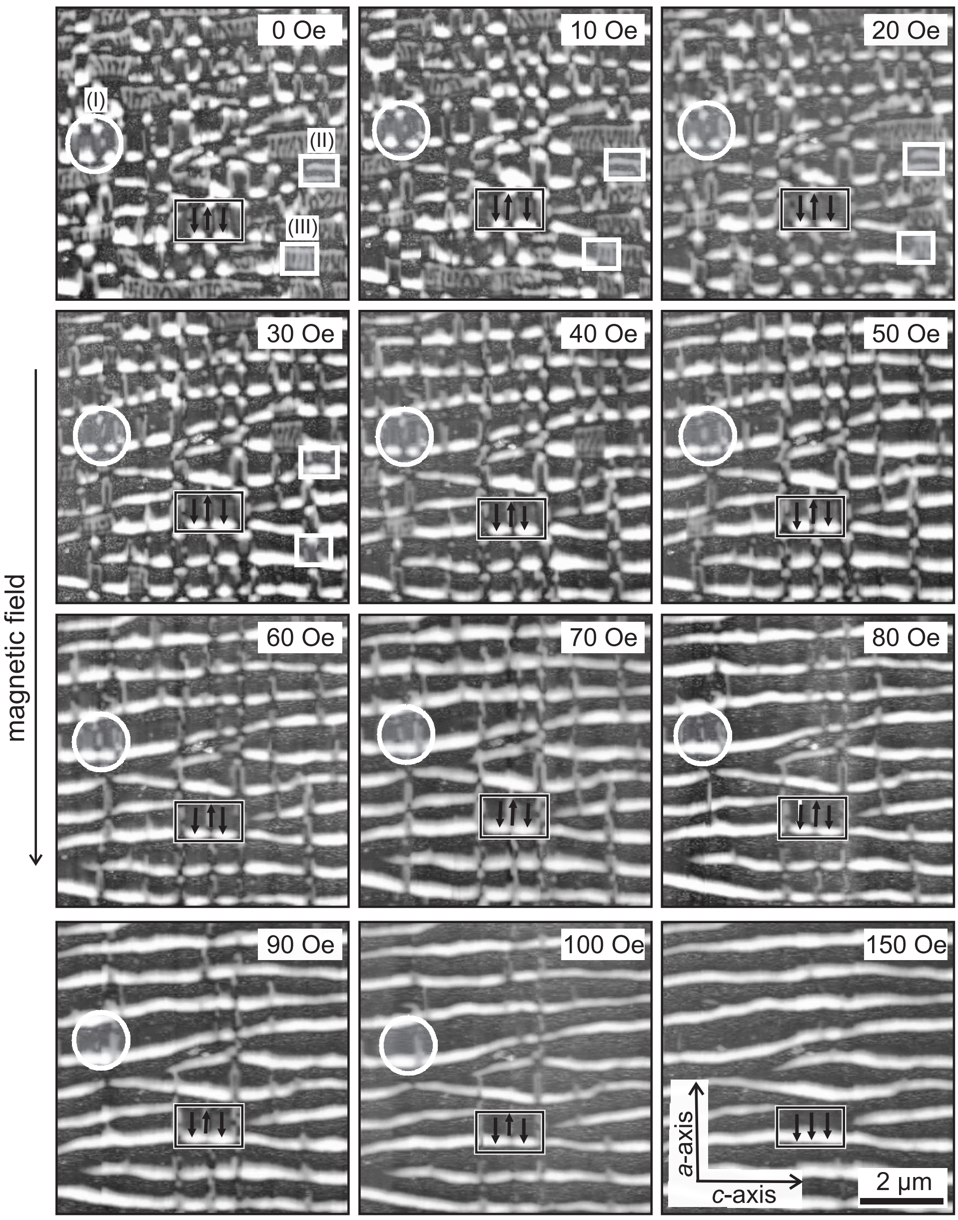

Figure 6.1: Field dependent MFM measurements at room temperature on a 180 nm thick MnAs film grown on GaAs (001). The field is applied along the easy axis (a-axis) of magnetization as indicated by the arrow on the left hand side. White circular and rectangular markers indicate areas of different domain types. Inside the black/white rectangular box the arrows show the local orientations of magnetization.

In order to follow the dynamics of the three major domain types more easily, selected areas are highlighted by light-white circular, as well as rectangular, outlines. Furthermore, the white rectangle shows the relative orientations of the in-plane magnetization vector for the selected areas. At 10 Oe, part of the type (III) domains and combinations of domains transform into type (I) domains. The type (III) domain which is highlighted in the figure transforms completely into a type (I) domain at an applied field of 30 Oe. Type (II) domains show the same behavior. Up to 40 Oe, there exist some type (III) domains. From 50 Oe on, there is no signature of type (II) or type (III) domains.

For increasing fields, an increasing fraction of the type (I) domains align with the applied field direction. Complete saturation is reached at a field of 150 Oe at room temperature. The MFM image is now showing single domains as extended white stripes along the *c*-axis. As the domain walls are driven out of the film at increasing magnetic fields, the type (II) and type (III) domains that exhibit a large number of domain walls, are transformed into type (I) domains.

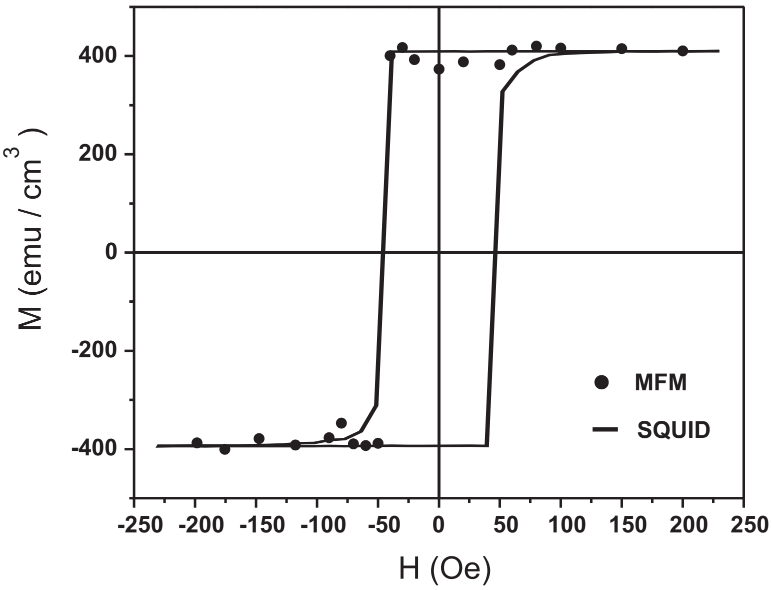

Figure 6.2: Microscopic hysteresis loop of a 180 nm thick MnAs film on GaAs (001) measured at room temperature by field-dependent MFM. The field was applied along the easy magnetization axis. MFM measurements (black dots) show good agreement with the SQUID magnetometry data (solid black line) obtained for the same film.

For comparison, the magnetic hysteresis of the entire film has been measured by SQUID magnetometry. Field-dependent MFM measurements allow a detailed insight into the microscopic domain evolution. Figure 6.2 shows the magnetization curve $M(H)$ measured by SQUID magnetometry (solid line) and the data points obtained from MFM measurements (black dots) for a 180 nm MnAs film. The analysis of MFM images results in a relative value for the magnetization of the scanned film area, as explained in the next paragraph. By taking the saturation magnetization per film area as measured by SQUID magnetometry into account, magnetization values can be obtained for the areas scanned by MFM. The MFM hysteresis loop data were obtained from measurements of the maximum to the minimum applied field, after an initial virgin curve scan. As the hysteresis curve is symmetric in the applied field, it is sufficient to measure a half-cycle of the hysteresis loop for a single component magnetic system. The MFM data points fit well with the SQUID magnetometry measurements. The coercive field was found to be 50 Oe from both measurements.

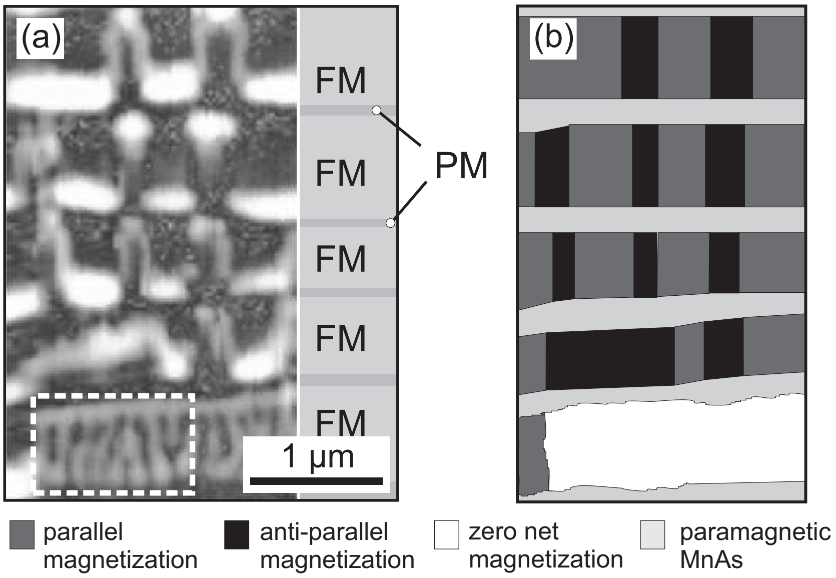

Figure 6.3: (a) MFM image at zero external field for a 180 nm thick film. The paramagnetic and ferromagnetic stripes are indicated on the right hand side of the figure. (b) Corresponding magnetization distribution showing areas of parallel, antiparallel, and zero net magnetization. Paramagnetic β-phase areas show grey contrast.

The details of the MFM data analysis are shown in Fig. 6.3. The ferromagnetic and paramagnetic stripes are shown schematically on the right hand side of Fig. 6.3(a). The sketch in Fig. 6.3(b) illustrates the distribution of the magnetization that corresponds to the MFM image on the left hand side [Fig. 6.3(a)]. For the estimation of the magnetization, the width of the ferromagnetic wires and the net magnetization as a result of the domain structure are taken into consideration. As the MFM contrast from the ferromagnetic wires extends into the paramagnetic regions, the real width of the stripe has been determined from the topographic image. The type (II) domains (not shown) and the comb-like combination domains, marked as a dotted rectangle in Fig. 6.3(a), possess no net magnetization, which is indicated by white areas in (b). The simulation of the comb-like domain structure revealed that the individual antiparallelly-oriented subdomains almost cancel completely out. Type (I) domains with parallel and antiparallel magnetization are shown in (b) as dark-gray and black areas, respectively. Only these domains account for the net magnetization.

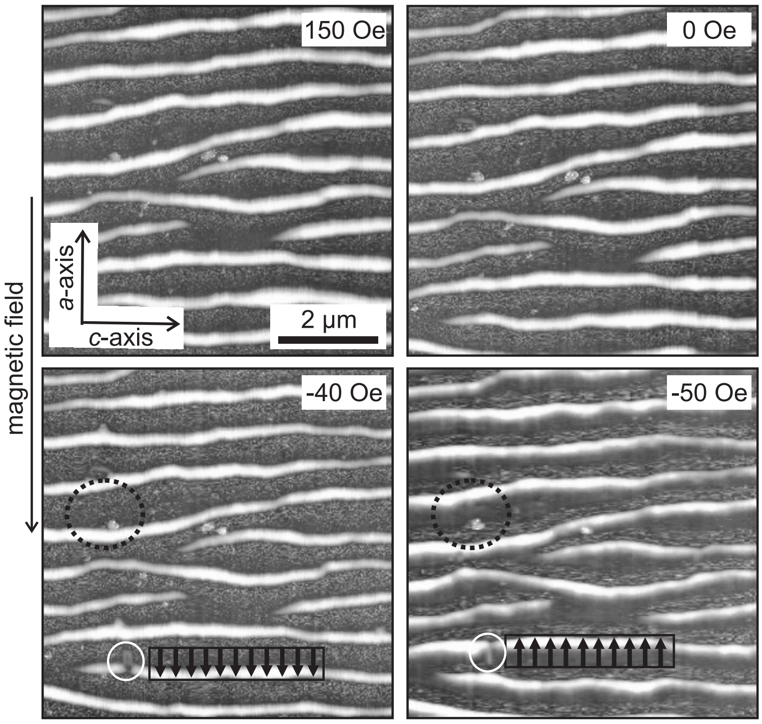

Figure 6.4: Magnetization reversal in 180 nm thick MnAs film on GaAs (001) measured by field-dependent MFM at room temperature. The selected MFM images were measured at different field values of the hysteresis cycle.

In Figure 6.2 it was shown that the coercive field is 50 Oe, in agreement with the SQUID magnetometry measurements. Next, we took a closer look at the magnetization reversal. Figure 6.4 shows selected MFM scans measured in the hysteresis cycle.

At 150 Oe (saturation field), the film shows a complete single domain behavior. As we decrease the field to 0 Oe, no significant change can be seen. From the SQUID hysteresis curve shown in Fig. 6.2 it is known that the ratio of remanent and saturation magnetization is nearly equal to one. Next, the field was increased slowly in the reverse direction. No large difference in contrast can be observed up to a field of -40 Oe. Suddenly, at -50 Oe, all the stripes flip to the opposite magnetization direction. In order to visualize the effect more clearly, two distinguished features were identified for the scans at -40 Oe and -50 Oe. One is dotted black circle, which indicates a defect on the surface. The second is a small feature along the *a*-axis which is marked by a white circle. The rectangle illustrates a location where the flipping can be easily seen. The black arrows indicate the orientation of the magnetic moments of the sample for the particular area. Hence, by variable-field MFM measurements, the microscopic hysteresis loop can be reproduced through point-by-point mapping of the domain structure.

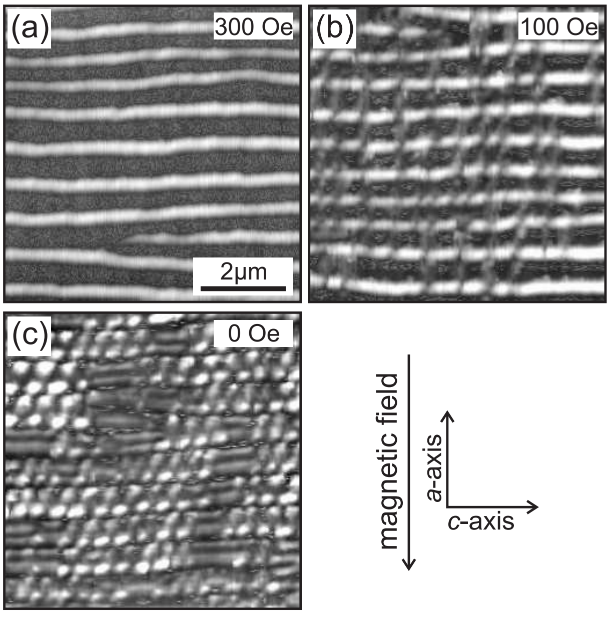

Figure 6.5: Selected field-dependent MFM images of the hysteresis cycle of an unusual sample measured at room temperature (180 nm thick MnAs film).

Furthermore, another sample of the same thickness was investigated which shows a quite different behavior compared to the previous sample. Following the same measurement procedure for the hysteresis loop, we obtained the images shown in Fig. 6.5. Above 150 Oe, the film is completely saturated. Figure 6.5(a) shows a scan taken at a field of 300 Oe, where the single domain behavior is evident. According to the previous measurement, it is expected that no change should occur when lowering the field down to 0 Oe. However, this sample behaves completely different. Already at 100 Oe [Fig. 6.5(b)], the film partially reduces its remanent magnetization by introducing antiparallelly-oriented type (I) domains. Surprisingly, at 0 Oe, the film shows the usual domain structures as one would see in the completely demagnetized state with evenly distributed type (I) domains of opposite magnetization and magnetization compensated type (II) domains. From this behavior, it is clear that the film does not have a significant remanent magnetization (the remanent magnetization is 24 emu/cm^3 compared to 400 emu/cm^3 for the standard MnAs film of the same thickness).

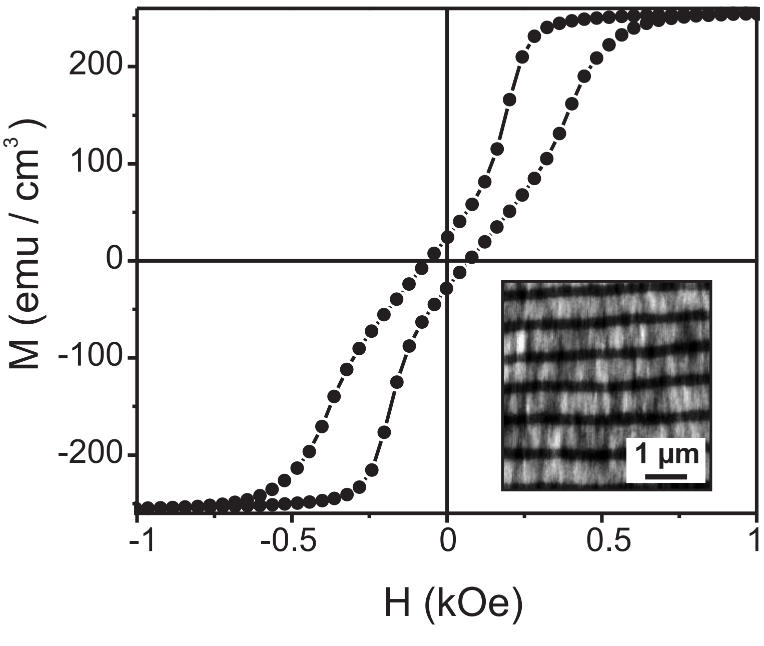

Figure 6.6: Hysteresis loop measured by SQUID magnetometry at 30 °C along the easy axis of the unusual MnAs film. The inset shows an AFM scan of the same film taken at room temperature.

Figure 6.6 shows the SQUID magnetometry hysteresis loop measured on the unusual sample at room temperature, which shows a similar behavior as observed by MFM. The unusual behavior could have its origin in the defects present in this sample. The AFM scan shown as an inset in the plot of the hysteresis loop indicates the presence of unusual surface defects.

6.2 Nucleation and growth of domains

The domain structures in the coexistence regime of the MnAs on GaAs (001) system show dramatic differences depending on the width of the ferromagnetic α-MnAs stripes. For a detailed study, films of four different thicknesses (120 nm, 180 nm, 300 nm, 500 nm) were investigated. Before every measurement, the film was first cooled down to its complete ferromagnetic phase and then it was slowly heated up to a temperature close to the transition temperature. Selected XMCDPEEM images from the heating cycle for each film thickness are presented in Figs. 6.7, 6.8, 6.9 and 6.10.

Figure 6.7 shows the measurements on a 120 nm thick film. At 4 °C, in the complete ferromagnetic phase, the film is made up of large magnetically single domain areas giving rise to black and white contrast. As the temperature is increased, the β-phase starts to nucleate as a dot-like structure, which grows into stripes. In the beginning of the nucleation of the paramagnetic phase, the ferromagnetic domains are extended type (I) (along the stripe) domains. Upon further increasing the width of the β-stripes, type (II) domains appear. At 26 °C, all major domain types are visible as shown in the figure. By analyzing the data in detail, it was found that in the temperature range between 10-22 °C mainly different domains appear, whereas between 22-37 °C the domain structures remain the same and only the width of the ferromagnetic stripe decreases. Up to 35 °C, the stripes are still perfectly connected along the stripe direction. It is also interesting to note that at the branching points (Y-shaped structure), where two stripes branch out from a single stripe, type (I) domains are always present. At higher temperatures, close to the phase transition, the ferromagnetic phase stripes are disconnected and mostly elongated type (I) domains are observed. For the 180 nm thick film the domain structures behave quite similar as in the case of the 120 nm thick film, except that the domains are more ordered. The growth and rearrangement of domains occur in the temperature range between 10-25 °C. At higher temperatures, between 25-37 °C, the width of the ferromagnetic stripes decreases, but the domain types remain initially the same. The stripes remain connected up to 35 °C. After that, elongated

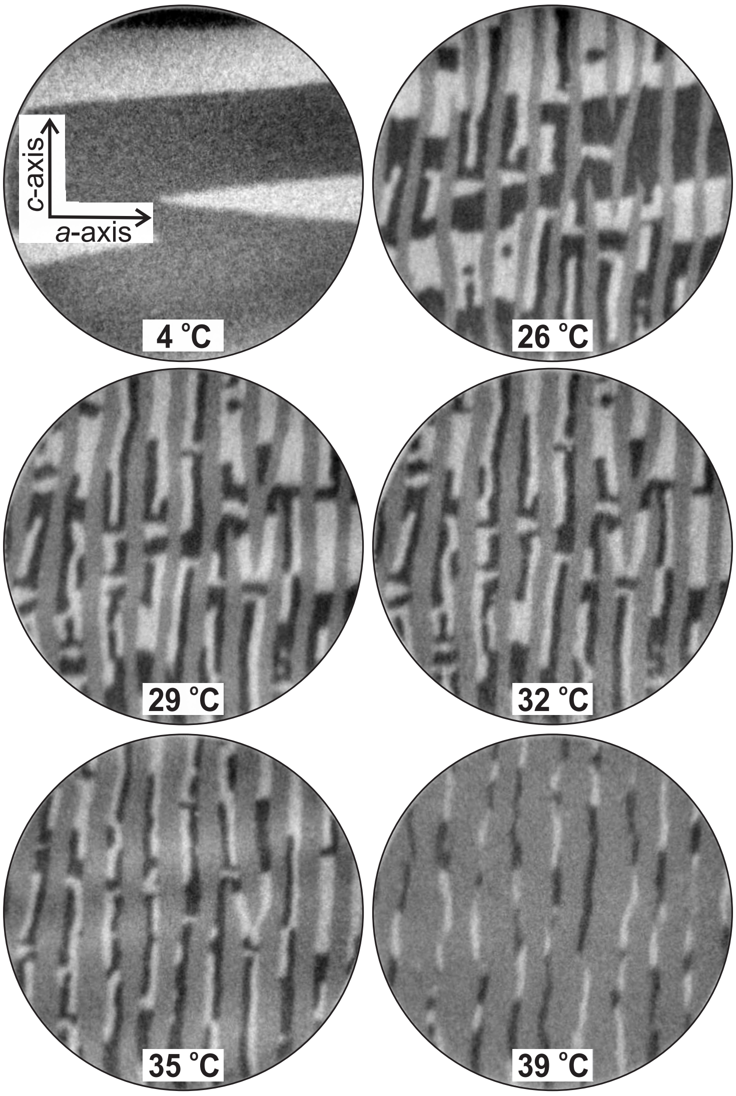

Figure 6.7: Stripe width-dependent domain structures of a 120 nm thick MnAs film on GaAs (001) imaged by XMCDPEEM. Field-of-view diameter: 5 μm.

structures of type (I) and (II) domains are dominant. A few degrees above 38 °C, the film completely transforms into the β-phase.

As the film thickness increases, the stripe periodicity and hence the width of the ferromagnetic stripes increases. Therefore different domain structures

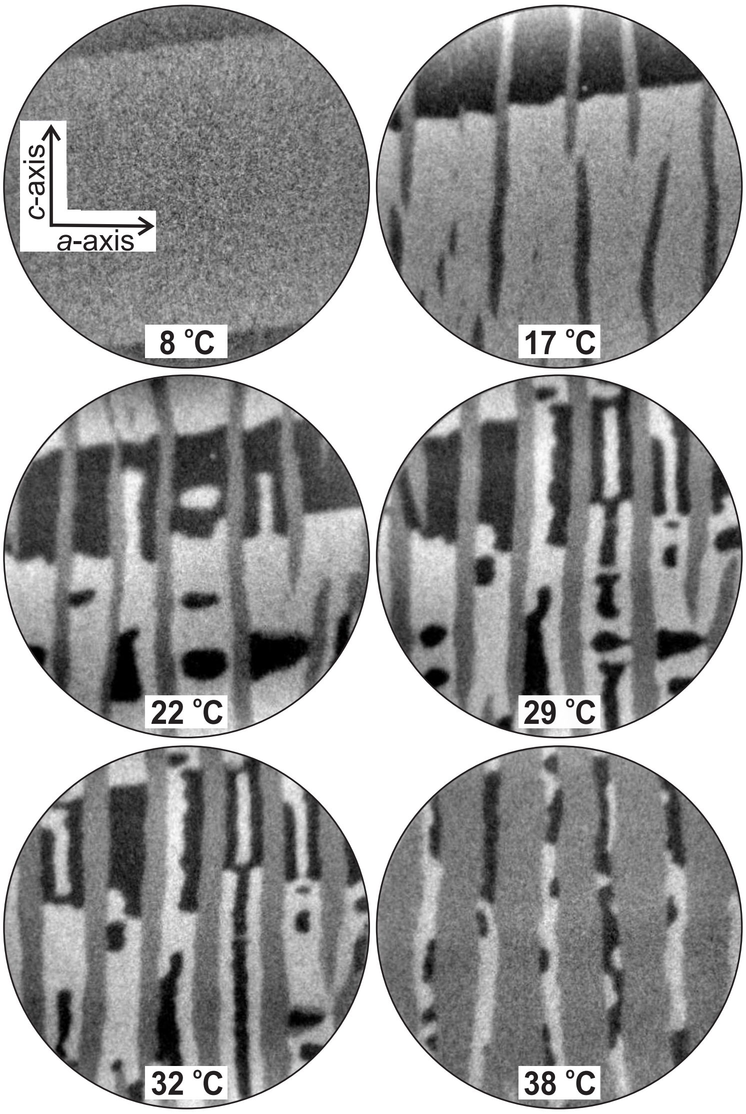

Figure 6.8: Stripe width-dependent domain structures of a 180 nm thick MnAs film on GaAs (001) imaged by XMCDPEEM. Field-of-view diameter: 5 μm.

were observed for thicker films (300 and 500 nm). Figures 6.9 and 6.10 show selected XMCDPEEM images taken from the heating sequence of MnAs films of a thickness of 300 and 500 nm. Besides the usual domain structures, i.e. type (I), (II), (III), more complicated domains (cf. scans at 19 and 24 °C in Figs. 6.9 and 6.10) are observed. A decreasing width results in the transfor-

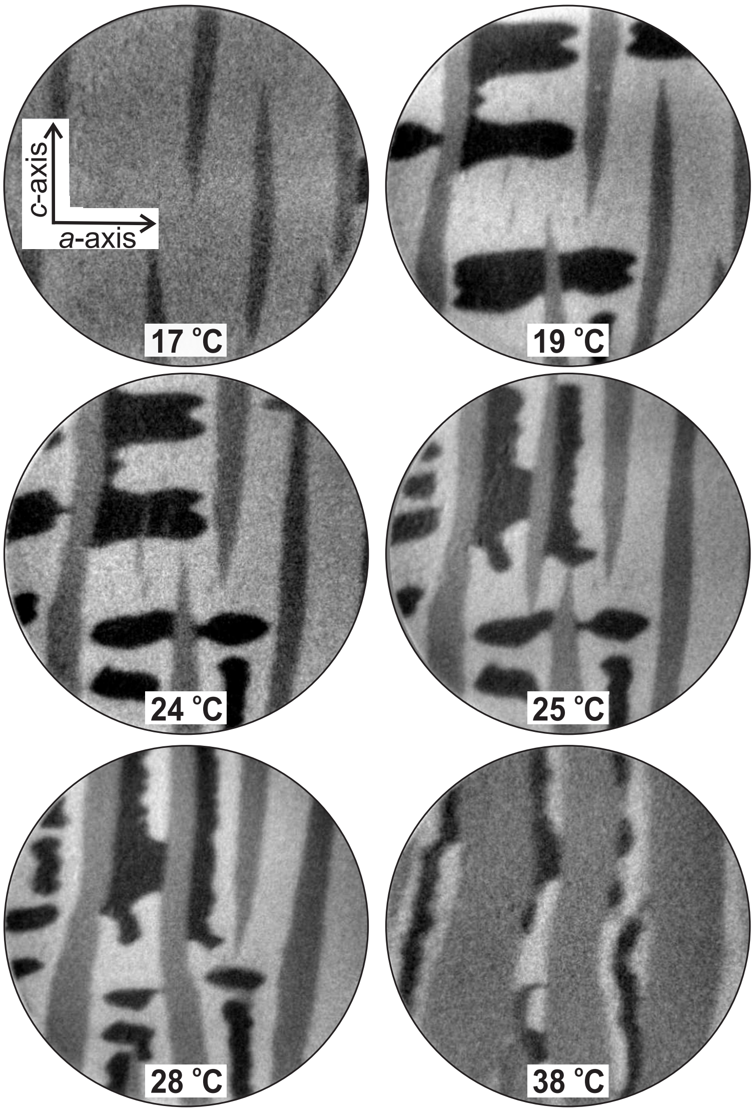

Figure 6.9: Stripe width-dependent domain structures of a 300 nm thick MnAs film on GaAs (001) imaged by XMCDPEEM. Field-of-view diameter: 5 μm.

mation of these domains into more complicated domains. At the branching points (Y-junction) of the ferromagnetic stripes, the more complicated domains are seen instead of the typical type (I) domains observed for the other two thicknesses of 120 and 180 nm. A further decrease of the ferromagnetic fraction of the film results in disconnected elongated stripe consisting of type (I) and type (II) domains. The appearance of different domain structures

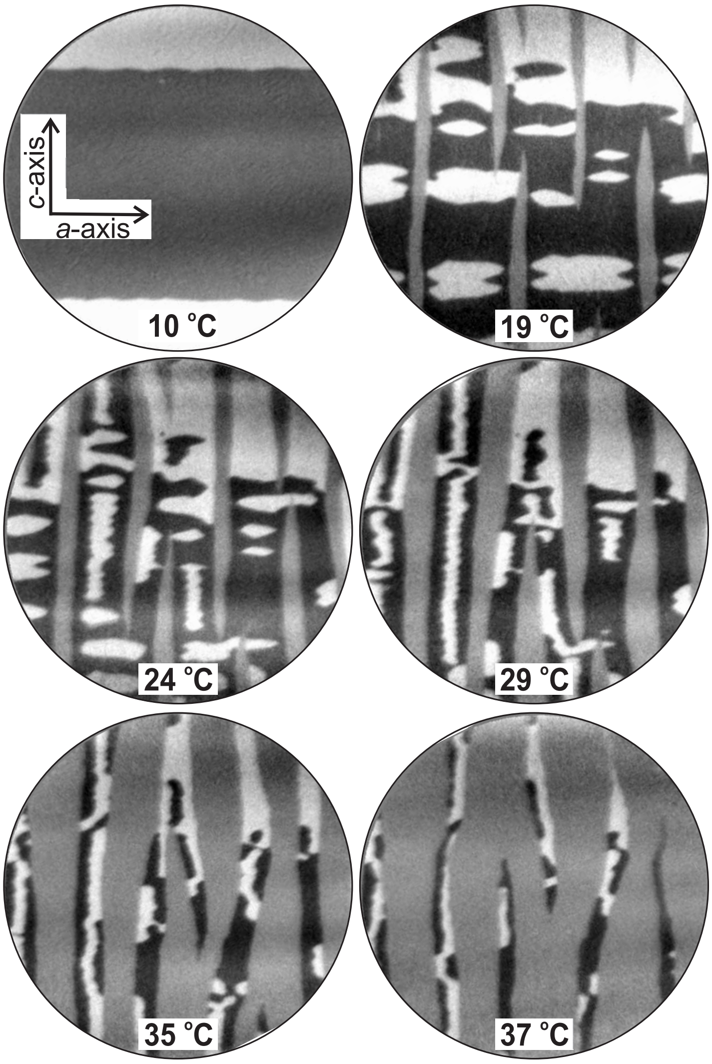

Figure 6.10: Stripe width-dependent domain structures of a 500 nm thick MnAs film on GaAs (001) imaged by XMCDPEEM. Field-of-view diameter: 10 μm.

for all these four thicknesses at different temperatures are summarized in Tab. 6.1.

The higher order domain structures, e.g. the type (III) domains, cost a lot of energy as the stray field is not minimized. From a micromagnetics standpoint, the existence of such domains is quite unlikely. Also, the dipole

Table 6.1: Appearance of domain structures as a function of temperature and film thickness for MnAs films on GaAs (001).

film thickness	**0–10 °C**	**10–37 °C**	**37–40 °C**
120 nm	type (I) *stripe formation*	type (I),(II),(III) *separated stripes*	type (I) *width decreases*
180 nm	type (I) *stripe formation*	type (I),(II),(III) *separated stripes*	type (I),(II) *width decreases*

film thickness	**0–18 °C**	**18–37 °C**	**37–40 °C**
300 nm	type (I) *stripe formation*	type (I),(II),(III) *separated stripes*	type (I),(II),(III) *width decreases*
500 nm	type (I) *stripe formation*	type (I),(II),(III) *separated stripes*	type (I),(II) *width decreases*

interaction between neighboring stripes should lead to more organized magnetic areas than it is observed in the measurements. One possible explanation could be the strain distribution in the film that affects the magnetic properties via magnetoelastic coupling.

Chapter 7

Patterning of MnAs Films

The strain state of epitaxial MnAs films on GaAs can be exploited for the self-organized structuring of the films by employing etching techniques. Etching alters the strain state of the film and leads, in certain cases, to the formation

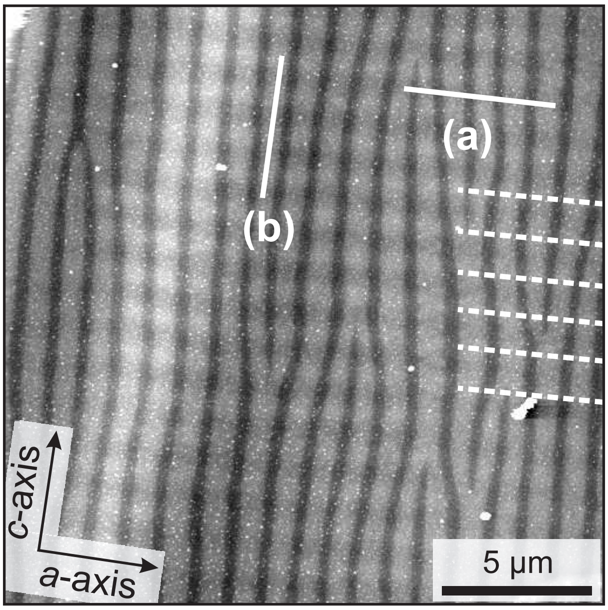

Figure 7.1: Two-dimensional strain pattern of a 215 nm thick MnAs films on GaAs (001). The period of the stripe structure measured along the line indicated by (a) is 1.25 μm with a peak-to-valley height modulation of roughly 3 nm. The second array perpendicular to the stripe structure (parallel dotted lines on the right hand side) has a periodicity of 1.28 μm with a height modulation of 1 nm measured along the *a*-axis, as indicated by (b).

of cracks. This has direct consequences on the structural as well as magnetic properties of the film. Details about the etching procedure and the pattern formation will discussed in this Chapter. Furthermore, by using AFM nanolithography, the film surface can be locally oxidized.

7.1 Etching of MnAs

MnAs films on GaAs (001) in the α-β-phase coexistence regime exhibit ordered stripes of the two phases, hereby relaxing the built-up strain along the a-axis direction. However, the smaller strain along the c-axis remains intact. Due to the volume difference of α- and β-MnAs of roughly 2%, α-MnAs can be identified as ridges, separated by β-MnAs grooves, stretching along the c-axis direction [KJS$^+$00, KJS$^+$02, PRK$^+$02]. The ordered array of stripes stretching along the c-axis direction can be easily identified in the AFM micrograph in Fig. 7.1. The period measured along a line indicated by (a) is 1.25 μm with a peak-to-valley height modulation of roughly 3 nm. Perpendicular to this structure, the remaining strain along the c-axis direction also results in a weaker film height modulation. This second modulation is easily visible close to the film edge, however, the strain is present throughout the entire film. The parallel dotted lines on the right hand side of the figure help to identify the second stripe array. The periodicity of this modulation, measured along the a-axis indicated by (b), is 1.28 μm and exhibits a height modulation of around 1 nm. This kind of structures are often observed as wrinkles or periodic structures at the boundary of clamped elastic sheets [CRCM02].

In general, the period of the α-β-stripe structure was found to be a function of the film thickness as shown in Sect. 4.3. Upon changing the temperature of a film with a given thickness, the period remains the same, while the phase content ϕ is a function of temperature and ranges from the purely α-phase film ($\phi = 1$) at the onset of the striped phase to the purely β-phase film ($\phi = 0$) at the phase transition temperature. This tunable periodic two-dimensional structure can be employed in the sense of a latent image. When a phase-selective etchant is applied to the surface, the pattern is transferred permanently into the film.

7.1.1 Selective etching of the MnAs phases

Etching has been widely used in semiconductor research as a tool to make defects visible [Das56]. By employing suitable etchants, wet chemistry can be the basis for the formation of self-organized magnetic island structures in MnAs thin films [TWH+03]. It was found that virtually all GaAs etchants do also react with MnAs. Even water shows some reaction with MnAs. The selective etching of α and β-MnAs was demonstrated with both hydrochloric acid-based and sulphuric acid-based solutions [TWR+03]. Before etching, defined areas of the film were protected with polymethylmethacrylate (PMMA), patterned by electron beam lithography, as indicated by black squares in the checkerboard-like pattern of Fig. 7.2. The resulting regular island structure is visible in the etched areas [cf. e.g. white circle in Fig. 7.2(a)]. The dotted square in the etch pattern indicates the position where the AFM micrograph [(Fig. 7.2(a)] was recorded. Moreover, the etch solution creeps under the protective resist layer during the etching leading to irregular MnAs edges. This effect is more pronounced for *c*-axis oriented edges than for *a*-axis oriented edges. Note also the formation of cracks along the *a*-axis direction that penetrate deep under the resist mask. The MFM image shows a regular domain pattern of antiparallely magnetized domains in the ferromagnetic stripes. Details of the MFM contrast and the micromagnetic properties have been explained in Fig. 4.2.

Almost all wet etchants used for etching GaAs also react with MnAs and even the prolonged exposure of MnAs samples to water leads to a phase-selective etching process. On the other hand, MnAs does not react with alcohols, thus allowing standard lithography processes for the film patterning. Our goal was to choose an etchant that has a high MnAs-phase selectivity. A hydrochloric acid based solution, $HCl:H_2O_2:H_2O$ with a ratio of 4:1:12, yielded the best results [TWH+03]. The etching process does not proceed in a layer-by-layer manner, but the etch solution selectively removes Mn atoms, as no Mn could be detected in the etched areas by energy-dispersive X-ray analysis [TWR+03]. Subsequent Raman measurements revealed a broad peak at $200 - 230$ cm^{-1} that is associated with amorphous arsenic which is left behind after the initial stage of the etching process [TWR+03]. Further exposure to the etch solution then leads to a slow dissolution of the amorphous arsenic. It has to be noted that, in contrast to the fast etching properties of MnAs in wet etchants, MnAs withstands reactive ion etching (RIE) for extended times. In this way, MnAs has been used as a RIE etch mask for GaAs [TWH+03].

Before exposing the MnAs film to the etch solution, the surface corrugation due to the two coexisting phases of MnAs can be easily measured by AFM. During the etching process, the sole information about the evolution of the surface corrugation does not give sufficient information about the etching rates of the two phases. The reason for this is that if the phase that occupies a larger volume (in this case α-MnAs) etches faster than the other phase, the corrugation will first vanish and then invert with respect to the initial corrugation. Thus, we make use of the fact that the two phase have distinctly different magnetic properties. Employing MFM in conjunction with AFM enables us to follow precisely the etching process in MnAs.

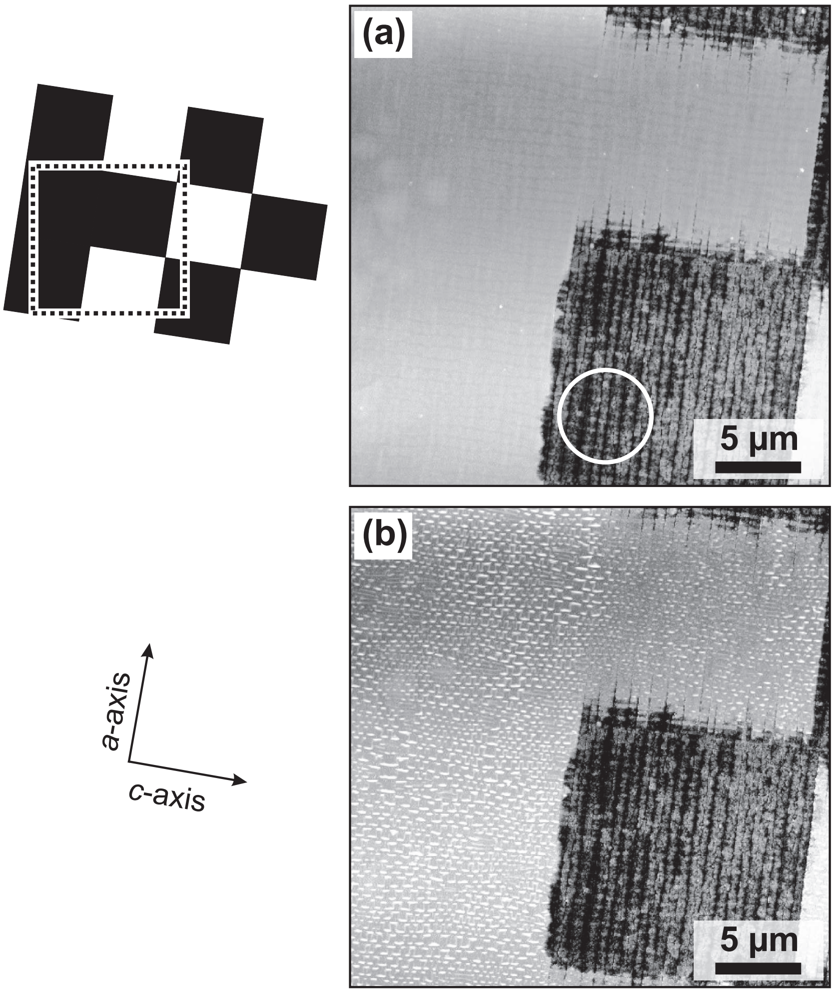

Figure 7.2: AFM (a) and MFM (b) images of a partially wet-etched MnAs film on GaAs (001). The selected white rectangle out of the checkerboard-like pattern shows the areas (black) that were protected by resist during the wet etching performed at room temperature. Self-organized magnetic islands are found in the etched areas (see white circle).

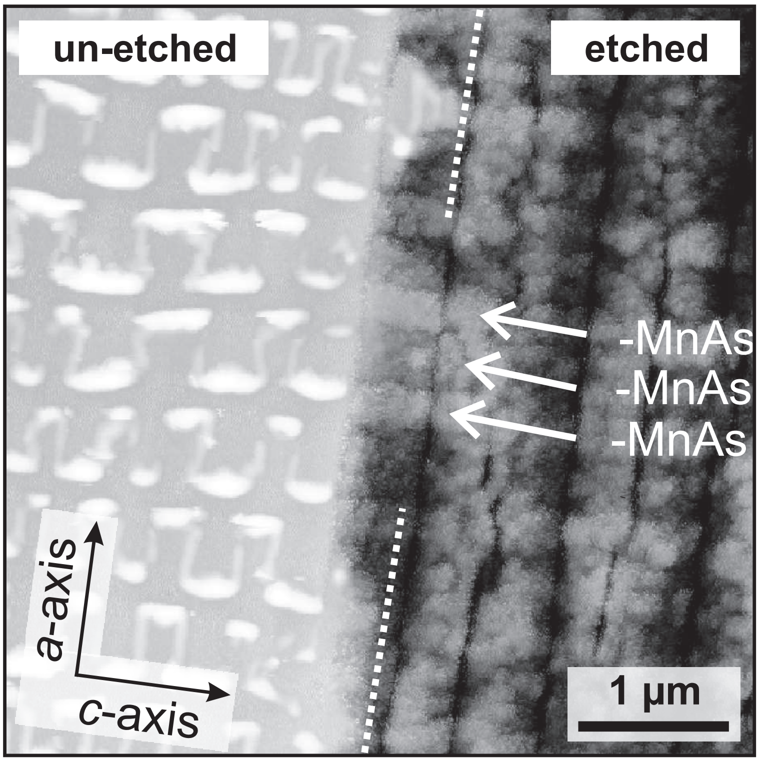

Figure 7.3: Phase-selective etching of a 215 nm thick MnAs film. In the unetched area, the magnetic contrast is predominant showing the typical type (I) domains (MFM), whereas in the etched area, the topographical features are visible (AFM). The white arrows mark the partially etched MnAs film. By correlating their position with the magnetic contrast of the α-stripes on the unetched film, it can be concluded that α-MnAs etches faster than β-MnAs.

The dominant micromagnetic contrast of demagnetized MnAs samples in the α-β-stripe phase stems from oppositely magnetized domains (oriented along the easy a-axis direction) that line up along the ferromagnetic stripes (oriented along the c-axis direction), as it is sketched in Fig. 4.2. The details about the magnetic contrast were explained previously in Sect. 4.1. Figure 7.3 presents the MFM contrast obtained for an etched film (as described above). The MFM image was recorded close to the boundary between an etched and a nominally unetched region (indicated by the dotted line). It predominantly shows alternatingly magnetized domain across the etch-protected parts of the film. The topographic contrasts are seen on the right hand side of the MFM scan. Two areas of this film are of particular interest and will be discussed in more detail. The first is located close to the a-axis oriented edge of the etch mask. This area allows to get a deeper insight into the etch rates for the two phases. The other is located close to the c-axis oriented edge of the etch mask and illuminates the formation of the cracks and the influence of strain on the micromagnetic properties.

Taking a closer look on the a-axis oriented edge, shown in Fig. 7.3, allows to determine the etch selectivity towards α- and β-phase MnAs. On the left hand side, the MFM image of the unetched area clearly shows the typical micromagnetic contrast of the ferromagnetic α-stripes discussed before. The dotted white line indicates the edge of the protective etch mask that was removed before the MFM scan. It is obvious that the etchant creeps underneath the mask and slowly etches from the side into the film. The underetching stops at a crack that runs along the a-axis direction slightly to the left from the dotted line. The unprotected area shows no magnetic contrast and the GaAs substrate is still covered with amorphous arsenic, as confirmed by Raman spectroscopy. Extending now the ferromagnetic stripes found on the left hand side of the image into the underetched area clearly proves that the α-phase etches faster than the β-phase (see arrows indicating the two phases).

One further remark has to be made about the etching process in terms of the dependence of the stripe structure period on the film thickness. If we assume a layer-by-layer etching process, the more material is removed from the film, the narrower the period gets in the course of the etching. This could be a problem in terms of phase selectivity, as the initially α-phase stripes transform into β-phase stripes periodically during the etching process. For example, assuming an initial film thickness of 100 nm associated with a stripe period of roughly 480 nm, a removal of 33 nm will lead to a stripe period of 320 nm and thus a strain-induced local phase inversion. The fact that the period does hardly change during the etching process (roughly 10 %, cf. [TWH$^+$03]) leads to the conclusion that the initial etching quickly destroys the strain balance and leaves the initial α-β-period, as it is determined by the etching temperature, intact. It has to be noted that increasing the temperature of the remaining α-stripes will of course lead to a phase coexistence within the stripes again.

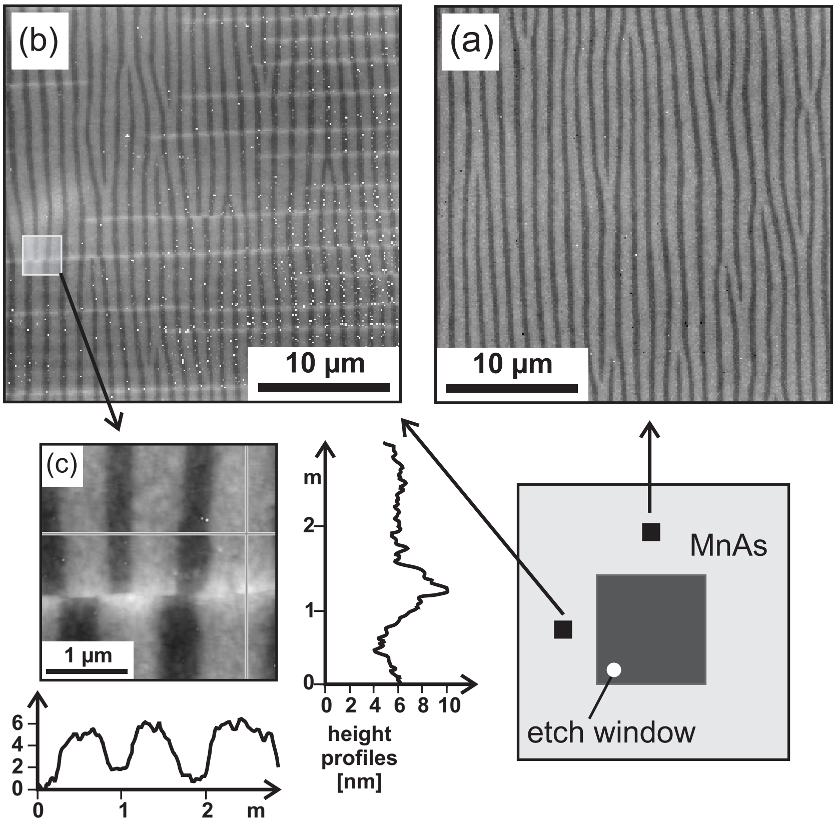

Figure 7.4: AFM topography images of the uncracked (a) and cracked (b) MnAs surface. The 215 nm thick MnAs film was wet etched through a window (see dark grey area) leading to a regular row of cracks running along the MnAs $[11\bar{2}0]$ direction. The zoom of the cracked surface area (c) shows a shift of the periodic α-/β-MnAs stripe structure across the crack. The line scan across the crack reveals that MnAs is piling up upon crack formation.

7.1.2 Crack formation in MnAs films

Once the Mn atoms are selectively removed from the MnAs layer, the strain balance of the film breaks down which results in the formation of regularly spaced cracks running along the c-axis direction. This phenomenon can be observed in areas located close to the c-axis oriented edge of the etch mask in Fig. 7.5. In general, the formation of cracks is observed for film thicknesses above 90 nm. Epitaxially grown films above a thickness of 500 nm exhibit cracks already in the as-grown state [DST^{+}01].

Figure 7.4(a) shows the topography of the α-/β-MnAs ridge-groove structure of a 215 nm thick MnAs film. Upon etching at room temperature, already at the early stages, the strain is relieved by the formation of cracks running solely along the $[11\bar{2}0]$ direction [Fig. 7.4(b)]. These cracks usually exhibit a regular distance from each other and laterally penetrate deep under the resist defining the etch window. Figure 7.4 shows an AFM scan of the MnAs surface close to the etch window. Higher magnification images [Fig. 7.4(c); position indicated in (b)] reveal very narrow cracks with a width beyond the resolution limit of the instrument. Corresponding line scans below and on the right hand side of the image provide further insight into the crack structure. First, the regular ridge-groove stripe pattern is decoupled across a crack. This becomes obvious near a defect in the regular stripe structure, where the stripes are free to rearrange after a crack is introduced to the system [cf. Fig. 7.4(c)]. MFM images further reveal that there is no magnetic domain correlation within a stripe across the crack. Second, the line scan along an α-MnAs stripe shows that the film bulges out at the position of the crack. The width of the distortion extends over roughly 1 μm and leads to an increase in height by about 4 nm. The cracks extend about 80 μm into the film in the a-axis direction, whereas they only extend about 15 μm into the film in the perpendicular direction.

The generation of cracks is the result of the accumulated strain along the c-axis direction. Whereas the strain along the a-axis direction due to the lattice mismatch between MnAs and GaAs and the large difference of the thermal expansion coefficients is relieved by the formation of the α-β-stripe structure, no such relaxation mechanism exists along the c-axis direction. Figure 7.5 shows an AFM micrograph recorded at the edge of the etch window oriented along the c-axis direction. In the lower part of the figure, all MnAs is removed from the sample and the blank GaAs substrate becomes visible. Closer to the etch front, i.e. already underneath the protective etch mask that was removed before taking the AFM scan, amorphous As islands are found. Right at the etch front, cracks are clearly visible at the surface. These cracks penetrate deep into the etch-protected film area, indicated by arrows labeled '1'. The cracks exhibit a defined periodicity. Further away from the etch front, the cracks (indicated by arrows labeled '2') are very narrow at the surface and exhibit the same lateral spacing as in the two-dimensional strain modulation pattern shown in Fig. 7.1. It is very likely that the etchant penetrates deep into the film directly at the MnAs-GaAs interface, leading to cracks that are found even 80 μm away from the edge. The local delamination that is typical for strained layers then allows the etchant to slowly open the cracks up to the

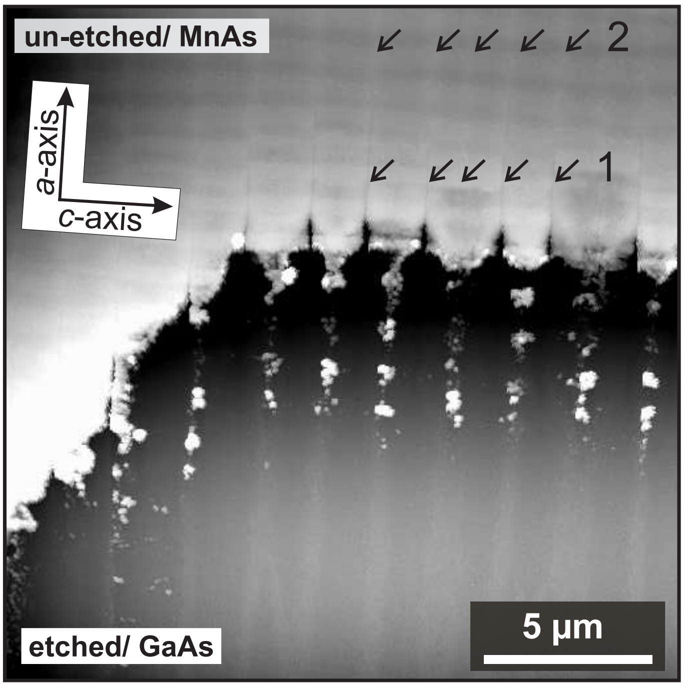

Figure 7.5: AFM image at the border between the etched and unetched areas of a 215 nm thick MnAs film. The film was etched at room temperature, i.e. in the α-β-stripe phase, again showing a large underetching. The unetched parts of the film show the coexisting phases oriented along the c-axis and, perpendicular to them, regularly spaced bright stripes (see arrows labeled '2') that originate from cracks at the etch front (see arrows labeled '1').

surface. It should be noted that MnAs can be etched without the formation of cracks employing $KOH/H_2O_2/H_2O$ [TWR$^+$03].

7.2 Temperature dependence of the etching process

In order to clarify the origin of the crack formation in further detail, we performed etching experiments at different temperatures. Figure 7.6 shows MFM measurements of three samples etched in the pure α-phase (a), the α-β-stripe phase (b), and the pure β-phase (c). Cracks (see arrows) are observed whenever α-phase material is present in the MnAs film. In the pure β-phase, no cracks are generated (c). This behavior is independent of the film thickness (for the investigated thickness range of 100 to 215 nm) [TWM$^+$04].

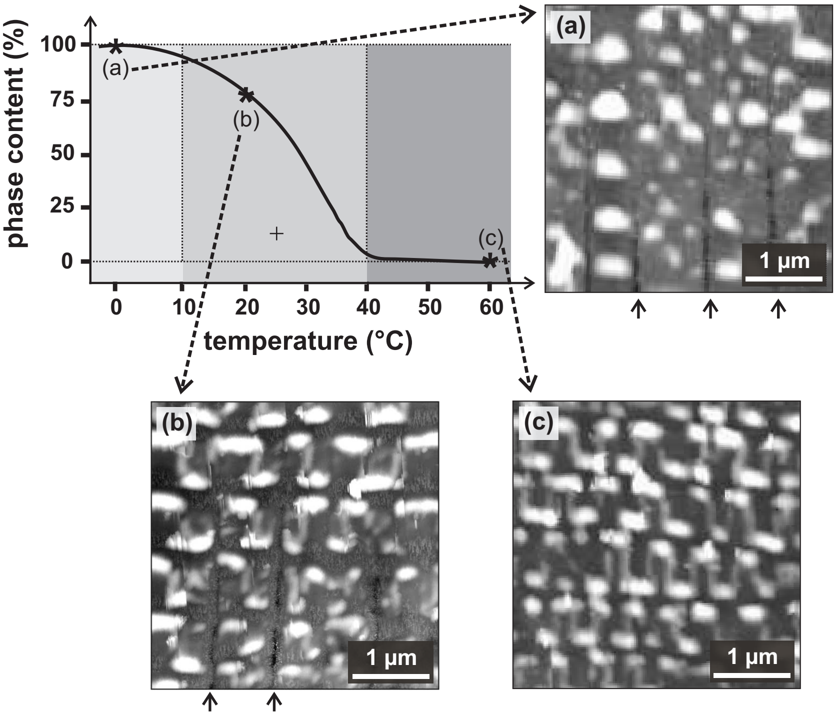

Figure 7.6: Variation of the α-phase content over temperature of the heating cycle measured by X-ray diffraction (upper left graph, see Ref. [KJS$^+$02]). Below 10 °C, the film is completely in its ferromagnetic α-phase (a), whereas above 40 °C (c), it is in its paramagnetic β-phase. The MFM scans (a-c) were recorded at room temperature in the etch-protected areas of the film, some μm away from the etch window.

The upper left graph in Fig. 7.6 shows the measured data of the α-phase content as a function of temperature obtained from X-ray diffraction experiments [KJS$^+$02]. The stars denote the phase compositions at which the etching experiments (a), (b), and (c) were performed. If strain along the c-axis alone would be the sole cause of the crack generation, the thicker MnAs films that have accumulated more stress should crack independent of the etching temperature. An analysis of the extension of the cracks into the unetched areas revealed that with decreasing α content, i.e. increasing etching temperature, the cracks get shorter, however, the distance between the cracks remains the same [TWM$^+$04]. Thus, we can conclude that it is the existence of the α-phase that is essential for the generation of cracks. The presence of the α-phase is associated with two phenomena. First, the formation of the α-β-stripe structure leads to a drastically altered strain state of the film

[DPN$^+$03]. Second, the present etching process has a high affinity to α-phase MnAs that possibly leads to the observed combination of interfacial etching, delamination, and crack formation.

7.3 Etch-induced stress release and its influence on the magnetic properties

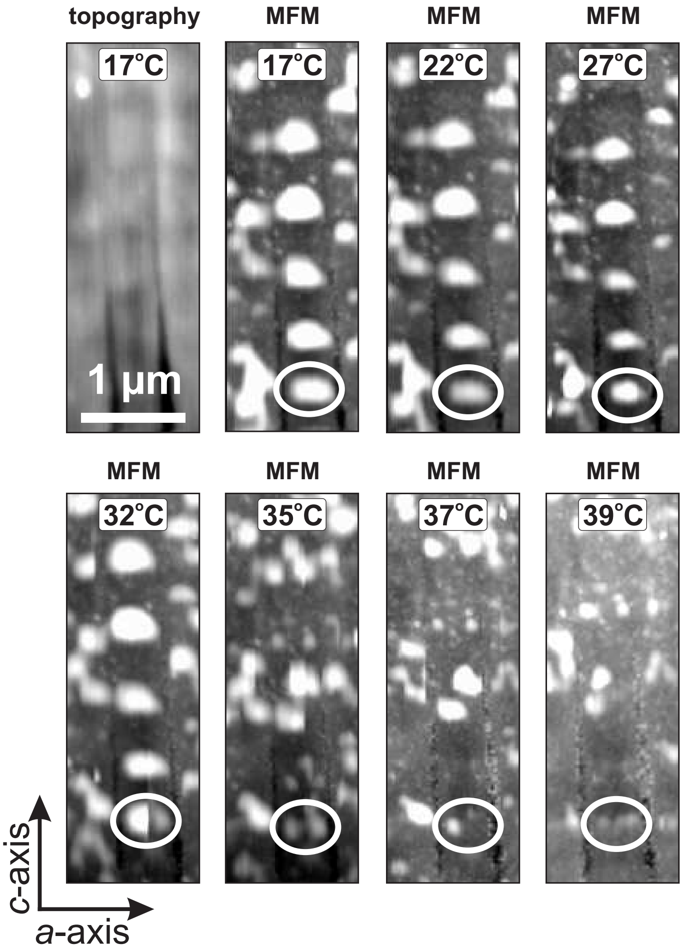

Figure 7.7: Variable-temperature MFM scans of a 215 nm thick MnAs film etched at 0 °C, i.e. in the complete α-phase. At 17 °C, a complementary AFM scan was taken in order to locate the exact position of the cracks.

As the first order phase transition in bulk MnAs can be strongly influenced by external pressure [BR62, MKDG69], one can expect that the magnetic properties are depending on the strain state of the MnAs-on-GaAs system.

It has been demonstrated that the transition temperature decreases when the volume is reduced due to hydrostatic pressure, i.e., compressive strain [MKDG69]. Therefore, MFM is not only very useful for determining the phase-selectivity of the etching process through the identification of the remaining material, it is also an indirect probe for the strain state of the (partially) relaxed MnAs film in the course of the etching process. The domain structure of a film exhibiting periodic cracks was studied as a function of temperature. Figure 7.7 shows selective area scans of a 215 nm thick MnAs film etched at 0 °C. The top left image displays the topography (AFM scan) obtained at 17 °C for finding the exact position of the cracks. The MFM scan to the right was also obtained at 17 °C and allows for a clear identification of the two phases. In the areas or compartments that are separated by two cracks, the α-stripes are in a single domain state. Upon heating the film, the stripes narrow and at 32 °C, the single domain state becomes unstable and the α-stripe confined in the compartment starts splitting up in two oppositely magnetized domains (see white ellipses). This trend continues and finally, at 39 °C, i.e. close to the phase transition temperature of the unetched and thus uncracked film, the ferromagnetic material still exists in the vicinity of the cracks. In Section 5.3, we found a shift of the phase transition temperature to higher values in locally strain-relaxed areas of up to 5 °C.

7.4 Nano-oxidation of MnAs

AFM nanolithography [WIC$^+$96, AHM97, AMHS98, IKLK97, SKX$^+$98, LDS02, DBBS98, HAH$^+$98, WTSS04, KOL$^+$98] is an exploratory research tool for obtaining sub-100 nm feature sizes, which conventional optical lithography techniques can not easily produce. AFM-based lithography techniques employ electrically conductive tips to apply an electric field across the tip-sample contact. In the case of MnAs, the thin water film present in ambient AFM experiments provides a source of oxygen for the oxidation of MnAs. Due to the small size of the AFM tip, this results in nanoscale-sized features which are of interest, e.g. for tunneling barriers. Using the lithography software [PSI] the structures (e.g. poly-lines or squares) can be drawn and written on the scanned sample area of the film. For our experiments a 25 nm thick MnAs film was used.

Figure 7.8(a) shows AFM images of the area after the lithography was performed using W_2C coated tips. For this experiment, a saw-tooth like pat-

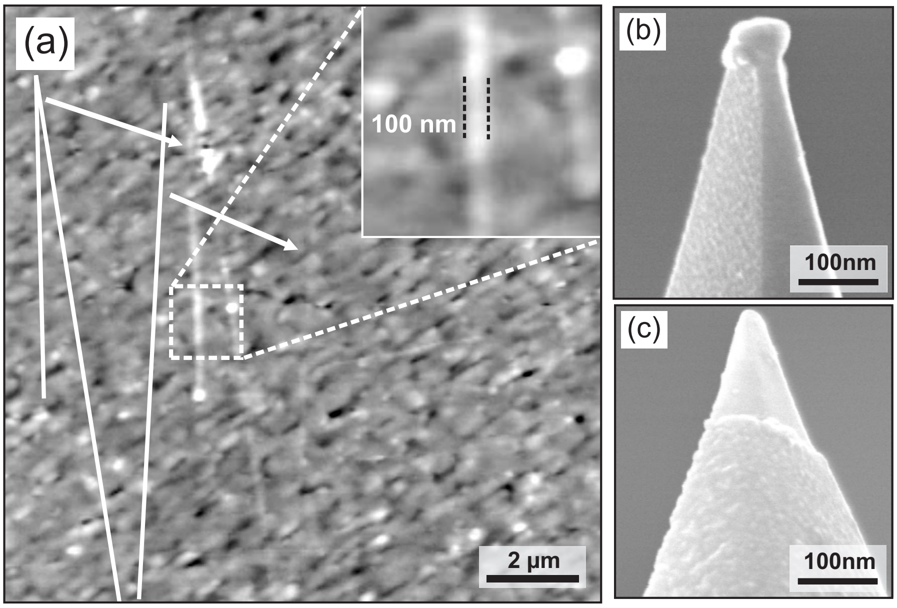

Figure 7.8: Oxidation of a MnAs film by AFM nanolithography. (a) Topography measured in contact mode. White lines and arrows indicate the structure as well the position of the written lines. SEM micrographs of the AFM tips with conductive coatings of tungsten carbide (W_2C) (b) and Au (c), respectively, after the measurement.

tern is defined. The white lines and arrows show the location and the shape of the written structure. Only a section of the total saw-tooth structure is written. The width of the written line is 100 nm, as can be seen in the inset in Fig. 7.8(a). The lithography parameters were as follows: force 200 nN, scan rate 10 μm/sec., and applied tip bias 10 V. After writing a small portion of the desired structure, the tip got contaminated and no further structures could be written. Different cantilevers with conductive coatings, e.g. W_2C, Au, Pt-Ir and heavily doped diamond, were used for the experiments. Figures 7.8(b) and (c) show scanning electron micrographs of the W_2C and Au coated tip, respectively, after the lithography experiment. The W_2C coated tip has some material on the tip apex. On the other hand, the Au coating is worn off of the tip apex. The tip reliability, compromised by wear and contamination, is found to be strongly dependent on the sample and the experimental conditions. Furthermore, a network of cracks is formed during the lithography process which disappears after some minutes. Nevertheless, the film remains unusable for electronic transport studies. In conclusion, nano-oxidation by AFM does not allow for the fabrication of insulating barriers in MnAs films.

Chapter 8

Summary

Ferromagnetic MnAs on semiconducting GaAs is an interesting III-V hybrid material system. The sharp interface of MnAs on GaAs along with its room temperature ferromagnetism shows potential for spin injection [RHK$^+$02], as well as magneto-logic [PDN$^+$03, NPKP03] applications. MBE-grown epitaxial MnAs films on GaAs (001) and (311)A show a periodic stripe structure of the coexisting ferromagnetic α- and paramagnetic β-phase over a wide temperature range of 10–40 °C as a consequence of the involved strain. The strain is mainly due to the mismatch of the thermal expansion coefficients of the hetero-epitaxial system [PRK$^+$02, KJS$^+$02]. In these films, a strong magnetic uniaxial anisotropy is observed, where the magnetic easy axis is aligned along the in-plane a-axis of MnAs. Furthermore, the hard axis of magnetization also lies in the film plane, which is unusual for a hexagonal system. The confinement of the magnetic domains within the ferromagnetic stripes of MnAs is a true realization of a structured uniaxial magnetic system. In order to make a device based on MnAs, the magnetic properties of the film have to be known in detail.

The magnetic domain structure of the system is determined by the minimization of the total energy consisting of the exchange energy, the anisotropy, the self-field, the applied field and the energy due to magnetostriction. In order to obtain a spatially resolved picture of the magnetization vector, suitable imaging techniques have to be employed. MFM [MW87], a common tool in magnetic research, is used for magnetic domain imaging with sub-μm resolution. MnAs undergoes a first-order phase transition around 40 °C, which is a coupled magneto-structural transition. As the separation between the phases changes with temperature, the coupling between the domains consequently depends on the temperature. Furthermore, as the width of the α-stripes shrinks with increasing temperature, the most prominent domain configuration is a function of temperature. The α-β-stripe structure shows a defined periodicity, which increases with the film thickness. Therefore, films of various thicknesses, starting from films measurable by MFM to a maximum thickness determined by the epitaxial growth, were studied. Mainly three domain types are seen, which are classified according to the number of subdivision of the magnetization along the easy axis within the width of the α-stripe. Thicker films show generally more complicated domain patterns.

In order to understand the magnetization reversal process, an external magnetic field has to be applied *in situ*, i.e. during the MFM measurements. The strength of the magnetic coupling between the stripes depends on the distance between neighboring domains. Besides the self-field of individual domains, the interaction field between the domains plays an important role for the effective orientation of the magnetization vector within a domain. Hence, the inter- and intra-domain (stray field minimization) coupling and its dynamics gives a deeper insight into this magnetic system. Furthermore, the distance between the ferromagnetic stripes can be tuned with temperature, therefore a combined variable-magnetic field and temperature MFM set-up is employed. For a 180 nm thick MnAs film on GaAs (001), a field of 150 Oe along the easy axis direction is needed for achieving the complete saturation of the magnetization, whereas the coercive field needed to reverse the magnetization is 50 Oe. Upon applying a magnetic field, the more complex magnetic domain structures vanish at smaller fields compared to the type (I) domains. Furthermore, we observe a shift of the ferromagnetic order temperature to higher values by applying a magnetic field.

As it is difficult to analyze MFM measurements in the sense of extracting the true magnetization distribution, a quantitative analysis of the MFM contrast using a simulation based on magnetostatics is performed. The extracted domain configurations are verified by complementary micromagnetic XMCDPEEM measurements. For obtaining a complete picture of the domain structure, the resolution as well as the sensitivity of both the methods have to be taken into account. Whereas MFM detects the out-of-plane component of the magnetic stray field of the sample and has thereby a depth sensitivity, XMCDPEEM is only sensitive to the magnetization of the uppermost atomic layers. From the comparison of measurements done by both methods on the same film, it can be concluded that thicker MnAs films (> 300 nm) show an in-depth domain structure.

MnAs on GaAs exhibits strain as a result of epitaxial constraints, which can be different for different orientations of the substrate. Therefore, epitaxial MnAs films on different GaAs substrate orientations are studied in detail. MnAs films on GaAs (111)B show a higher transition temperature of 56 °C compared to films on GaAs (001) and (311)A. The strain state of the film is further studied using an etchant that selectively etches the MnAs phases. It is found that the α-MnAs etches faster than β-MnAs. Local strain relaxation and its effect on the magnetic properties is studied in detail in order to understand the interplay of strain and the magnetic properties of the film. A strain relaxation leads to the formation of regularly spaced cracks that are oriented perpendicular to the stripe structure. The transition temperature increases locally in the vicinity of the cracks in accordance with the results obtained by pressure-dependent measurements in bulk MnAs.

Bibliography

[ACL98] Altman, M. S.; Chung, W. F.; Liu, C. H.: In: *Surf. Rev. Lett.*, volume 5:p. 1129, 1998. 22

[AHM97] Avouris, P.; Hertel, T.; Martel, R.: In: *Appl. Phys. Lett.*, volume 71:p. 285, 1997. 86

[AMHS98] Avouris, P.; Martel, R.; Hertel, T.; Sandstrom, R.: In: *Appl. Phys. A*, volume 66:p. 1, 1998. 86

[ASBW87] Allenspach, R.; Sallemik, H.; Bischof, A.; Weibel, E.: In: *Z. Phys. B-Condensed Matter*, volume 67:p. 125, 1987. 9

[ATUN95] Akeura, K.; Tanaka, M.; Ueki, M.; Nishinaga, T.: In: *Appl. Phys. Lett.*, volume 67:p. 3349, 1995. 4

[AWW88] Abraham, D. W.; Williams, C. C.; Wickramasinghe, H. K.: In: *Appl. Phys. Lett.*, volume 53:p. 1446, 1988. 9

[Bau94] Bauer, E.: In: *Rep. Prog. Phys.*, volume 57:p. 895, 1994. 21, 22

[Bau98] Bauer, Ernst: In: *Surf. Rev. Lett.*, volume 5:p. 1275, 1998. 21, 22

[Bau01] Bauer, E.: In: *J. Phys.: Condens. Matter*, volume 13:p. 11391, 2001. 20

[BCD$^+$02] Bauer, E.; Cherifi, S.; Daeweritz, L.; Kaestner, M.; Heun, S.; Locatelli, A.: In: *J. Vac. Sci. Technol. B*, volume 20:p. 2539, 2002. 19, 42

[BR62] Bean, C. P.; Rodbell, D. S.: In: *Phys. Rev.*, volume 126:p. 104, 1962. 4, 42, 55, 85

[BR63] Blois, R. W. De; Rodbell, D. S.: In: *Phys. Rev.*, volume 130:p. 1347, 1963. 4

[CA98] Chung, W. F.; Altman, M.S.: In: *Ultramicroscopy*, volume 74:p. 237, 1998. 22

[Cla94] Clarke, J.: In: *Scientific American*, volume 271:p. 46, 1994. xiv, 17

[CRCM02] Cerda, E.; Ravi-Chander, K.; Mahadevan, L.: In: *Nature (London)*, volume 419:p. 579, 2002. 76

[CWMS99] Chernenko, V. A.; Wee, L.; McCormick, P. G.; Street, R.: In: *J. Appl. Phys.*, volume 85:p. 7833, 1999. xiii, 5, 56

[Das56] Dash, W. C.: In: *J. Appl. Phys.*, volume 27:p. 1193, 1956. 76

[DBBS98] Dobisz, E. A.; Brandow, S. L.; Bass, R.; Shirey, L. M.: In: *J. Vac. Sci. Technol. B*, volume 16:p. 3695, 1998. 86

[DKH$^+$03] Däweritz, L.; Kästner, M.; Hesjedal, T.; Plake, T.; Jenichen, B.; Ploog, K. H.: In: *J. Cryst. Growth*, volume 251:p. 297, 2003. 29, 45

[DPN$^+$03] Das, A. K.; Pampuch, C.; Ney, A.; Hesjedal, T.; Däweritz, L.; Koch, R.; Ploog, K. H.: In: *Phys. Rev. Lett.*, volume 91:p. 087203, 2003. xxi, 7, 42, 85

[DSK$^+$02] Däweritz, L.; Schippan, F.; Kästner, M.; Jenichen, B.; Kaganer, V. M.; Ploog, K. H.; Dennis, B.; Neumann, K. U.; Ziebeck, K. R. A.: In: *Inst. Phys. Conf. Ser. No*, volume 170:p. 269, 2002. 1, 5

[DST$^+$01] Däweritz, L.; Schippan, F.; Trampert, A.; Kästner, M.; Behme, G.; Wang, Z. M.; Moreno, M.; Schützendübe, P.; Ploog, K. H.: In: *J. Cryst. Growth*, volume 227-228:p. 834, 2001. 29, 32, 36, 56, 81

[DWJ$^+$04] Däweritz, L.; Wan, L.; Jenichen, B.; Herrmann, C.; Mohanty, J.; Trampert, A.; Ploog, K. H.: In: *J. Appl. Phys.*, volume 96:p. 5056, 2004. 29, 30, 34

[EEDDO02] Etgens, V. H.; Eddrief, M.; D. Demaille, Y. L. Zheng; Ouerghi, A.: In: *J. Cryst. Growth*, volume 240:p. 64, 2002. 32

[EHMN$^+$04] Engel-Herbert, R.; Mohanty, J.; Ney, A.; Hesjedal, T.; Däweritz, L.; Ploog, K. H.: In: *Appl. Phys. Lett.*, volume 84:p. 1132, 2004. 40

[EHon] Engel-Herbert, R.: Ph.D. thesis, Humboldt University Berlin, under preparation. 15, 16, 36, 37

[Ele] `http://www.elettra.trieste.it/experiments/beamlines/nano/index.html`. 18

[Fe] Armco soft iron, see `http://www.remag.de/`. 13

[FKD03] Friedland, K. J.; Kästner, M.; Däweritz, L.: In: *Phys. Rev. B*, volume 67:p. 113301, 2003. 32

[GB96] Grzelakowski, K.; Bauer, E.: In: *Rev. Sci. Instrum.*, volume 67:p. 642, 1996. 21

[GCdC+04] Gama, Sergio; Coelho, Adelino A.; de Campos, Ariana; Carvalho, A. Magnus G.; Gandra, Flávio C. G.; von Ranke, Pedro J.; de Oliveira, Nilson A.: In: *Phys. Rev. Lett.*, volume 93:p. 237202, 2004. 56

[GK69] Goodenough, J. B.; Kafalas, J. A.: In: *Phys. Rev.*, volume 157:p. 389, 1969. 2

[GMH+88] Grütter, P.; Meyer, E.; Heinzelmann, H.; Rosenthaler, L.; Hidber, H. R.; Güntherodt, H. J.: In: *J. Vac. Sci. Technol. A*, volume 6:p. 279, 1988. 9

[GSEFW70] Grønvold, F.; Snildal, S.; E. F. Westrum, Jr.: In: *Acta Chem. Scand.*, volume 24:p. 285, 1970. 6

[Gui51] Guillaud, C.: In: *J. Phys. Radium*, volume 12:p. 223, 1951. 4, 59

[HAH+98] Hu, S.; Altmeyer, S.; Hamidi, A.; Spangenberg, B.; Kurz, H.: In: *J. Vac. Sci. Technol. B*, volume 16:p. 1983, 1998. 86

[Har88] Hartmann, U.: In: *J. Appl. Phys.*, volume 64:p. 1561, 1988. 15

[Har90] Hartmann, U.: In: *J. Vac. Sci. Technol. A*, volume 8:p. 411, 1990. 15

[HBvS+02] Hoffmann, R.; Bürgler, D. E.; van Schendel, P. J. A.; Hug, H. J.; Martin, S.; Güntherodt, H. J.: In: *J. Magn. Magn. Mater.*, volume 250:p. 32, 2002. 34

[Igo] `http://www.wavemetrics.com/Products/IGORPro/igorpro.htm`. 48

[IKLK97] Irmer, B.; Kehrle, M.; Lorenz, H.; Kotthaus, J. P.: In: *Appl. Phys. Lett.*, volume 71:p. 1733, 1997. 86

[IKS+03] Iikawa, F.; Knobel, M.; Santos, P. V.; Adriano, C.; Couto, O. D. D.; Brasil, M. J. S. P.; Giles, C.; Magãlhaes-Paniago, R.; Däweritz, L.: In: *J. Magn. Magn. Mater.*, volume 272-276:p. 1154, 2003. 57

[IKS+05] Iikawa, F.; Knobel, M.; Santos, P. V.; Adriano, C.; Couto, O. D. D.; Brasil, M. J. S. P.; Giles, C.; Magãlhaes-Paniago, R.; Däweritz, L.: In: *Phys. Rev. B*, volume 71:p. 045319, 2005. 57

[IKWW03] Ishikawa, Fumihiro; Koyma, Keiichi; Watanabe, Kazuo; Wada, Hirofumi: In: *Jpn. J. Appl. Phys.*, volume 42:p. L918, 2003. 57

[ISKK02] Imada, S.; Suga, S.; Kuch, W.; Kirschner, J.: In: *Surf. Rev. Lett.*, volume 9:p. 877, 2002. xiv, 18, 19

[JKK+03] Jenichen, B.; Kaganer, V. M.; Kästner, M.; Herrmann, C.; Däweritz, L.; Ploog, K. H.: In: *Phys. Rev. B*, volume 68:p. 132301, 2003. 33

[KDP02] Kästner, M.; Däweritz, L.; Ploog, K. H.: In: *Surf. Sci.*, volume 511:p. 323, 2002. 32

[KHDP02] Kästner, M.; Herrmann, C.; Däweritz, L.; Ploog, K. H.: In: *J. Appl. Phys.*, volume 92:p. 5711, 2002. 36

[KJS+00] Kaganer, V. M.; Jenichen, B.; Schippan, F.; Braun, W.; Däweritz, L.; Ploog, K. H.: In: *Phys. Rev. Lett.*, volume 85:p. 341, 2000. 1, 5, 76

[KJS+02] Kaganer, V. M.; Jenichen, B.; Schippan, F.; Braun, W.; Däweritz, L.; Ploog, K. H.: In: *Phys. Rev. B*, volume 66:p. 045305, 2002. xx, 1, 5, 41, 47, 76, 84, 88

[KOL+98] Kim, J.; Oh, Y.; Lee, H.; Shin, Y.; Park, S.: In: *Jpn. J. Appl. Phys.*, volume 37:p. 7148, 1998. 86

[LDS02] Legrand, B.; Deresmes, D.; Stiévenard, D.: In: *J. Vac. Sci. Technol. B*, volume 20:p. 862, 2002. 86

[Mac] `http://www.elettra.trieste.it/nanospectroscopy/igor/igormanual.html`. 48

[Mag] `http://www.ibs-magnet.de/`. 13

[MHP+03] Mohanty, J.; Hesjedal, T.; Plake, T.; Kästner, M.; Däweritz, L.; Ploog, K. H.: In: *Appl. Phys. A*, volume 77:p. 739, 2003. 38, 42, 43

[MKDG69] Menyuk, N.; Kafalas, J. A.; Dwight, K.; Goodenough, J. B.: In: *Phys. Rev.*, volume 177:p. 942, 1969. 34, 55, 57, 85, 86

[MMR] Micro miniature refrigerator with a K-20 temperature controller, `http://www.mmr.com`. 12, 43

[MRR+03] Mira, J.; Rivadulla, F.; Rivas, J.; Fondado, A.; Guidi, T.; Caciuffo, R.; Carsughi, F.; Radaelli, P. G.; Goodenough, J. B.: In: *Phys. Rev. Lett.*, volume 90:p. 097203, 2003. 56, 57

[MRS+88] Mamin, H. J.; Rugar, D.; Stern, J. E.; Terris, B. D.; Lambert, S. E.: In: *Appl. Phys. Lett.*, volume 53:p. 1563, 1988. 9

[MRW88] Martin, Y.; Rugar, D.; Wickramasinghe, H. K.: In: *Appl. Phys. Lett.*, volume 52:p. 244, 1988. 9

[MW87] Martin, Y.; Wickramasinghe, H. K.: In: *Appl. Phys. Lett.*, volume 50:p. 1455, 1987. 2, 9, 88

[NHD+05] Ney, A.; Hesjedal, T.; Däweritz, L.; Koch, R.; Ploog, K. H.: In: *J. Magn. Magn. Mater.*, volume 288:p. 173, 2005. 42, 57, 59

[NHP+03] Ney, A.; Hesjedal, T.; Pampuch, C.; Mohanty, J.; Das, A. K.; Däweritz, L.; Koch, R.; Ploog, K. H.: In: *Appl. Phys. Lett.*, volume 83:p. 2850, 2003. 58

[NPFB00] Ney, A.; Poulopoulos, P.; Farle, M.; Baberschke, K.: In: *Phys. Rev. B*, volume 62:p. 11336, 2000. 37

[NPKP03] Ney, A.; Pampuch, C.; Koch, R.; Ploog, K. H.: In: *Nature*, volume 425:p. 485, 2003. 1, 88

[OME+03] Ouerghi, A.; Marangolo, M.; Eddrief, M.; Guyard, S.; Etgens, V. H.; Garreau, Y.: In: *Phys. Rev. B*, volume 68:p. 115309, 2003. 32

[PAR] Park Scientific Instruments, Autoprobe CP-Research user's guide part-II: advanced techniques. xiii, 10

[PDN+03] Pampuch, C.; Das, A. K.; Ney, A.; Däweritz, L.; Koch, R.; Ploog, K. H.: In: *Phys. Rev. Lett.*, volume 91:p. 147203, 2003. 1, 88

[PHM+03] Plake, T.; Hesjedal, T.; Mohanty, J.; Kästner, M.; Däweritz, L.; Ploog, K. H.: In: *Appl. Phys. Lett.*, volume 82:p. 2308, 2003. 42, 43

[PHRL91] Pesekt, A.; Hingerl, K.; Riesz, F.; Lischka, K.: In: *Semicon. Sci. Technol.*, volume 6:p. 705, 1991. 30

[Pri90] Prinz, G. A.: In: *Science*, volume 250:p. 1092, 1990. 1

[Pri95] Prinz, G. A.: In: *Phys. Today*, volume 48:p. 58, 1995. 1

[PRK+02] Plake, T.; Ramsteiner, M.; Kaganer, V. M.; Jenichen, B.; Kästner, M.; Däweritz, L.; Ploog, K. H.: In: *Appl. Phys. Lett.*, volume 80:p. 2523, 2002. 1, 5, 41, 76, 88

[PS03] Phaneuf, Raymond J.; Schmid, Andreas K.: In: *Phys. Today*, volume 56:p. 50, 2003. 21, 22

[PSI] XE-100, see `http://www.psia.co.kr/Product/Research_100_01.asp`. 86

[REM+98] Rose, K. C.; Engel, W.; Meißen, F.; Patchett, A.J.; Bradshaw, A. M.; Imbihl, R.: In: *Surf. Rev. Lett.*, volume 5:p. 1233, 1998. 22

[RHK+02] Ramsteiner, M.; Hao, H. Y.; Kawaharazuka, A.; Zhu, H. J.; Kästner, M.; Hey, R.; Däweritz, L.; Grahn, H. T.; Ploog, K. H.: In: *Phys. Rev. B*, volume 66:p. 081304(R), 2002. 1, 88

[RME+88] Rugar, D.; Mamin, H. J.; Erlandsson, R.; Stern, J. E.; Terris, B. D.: In: *Rev. Sci. Instrum.*, volume 59:p. 2337, 1988. 9

[SBD+00] Schippan, F.; Behme, G.; Däweritz, L.; Ploog, K. H.; Dennis, B.; Neumann, K. U.; Ziebeck, K. R. A.: In: *J. Appl. Phys.*, volume 88:p. 2766, 2000. 24, 62

[Sch00] Schippan, F.: Ph.D. thesis, Humboldt University Berlin, 2000. 7

[SGG+87] Sáenz, J. J.; Gracía, N.; Grütter, P.; Meyer, E.; Heinzelmann, H.; Weisendanger, R.; Rosenthaler, L.; Hidber, H. R.; Güntherodt, H. J.: In: *J. Appl. Phys.*, volume 62:p. 4293, 1987. 9, 15

[SGS88] Sáenz, J. J.; Gracía, N.; Slonczewski, J. C.: In: *Appl. Phys. Lett.*, volume 53:p. 1449, 1988. 9

[SHS+98] Schmidt, Th.; Heun, S.; Slezak, J.; Diaz, J.; Prince, K. C.; Lilienkamp, G.; Bauer, E.: In: *Surf. Rev. Lett.*, volume 5:p. 1287, 1998. 2, 19

[SKIJ00] Sadowski, J.; Kanski, J.; Ilver, L.; Johansson, J.: In: *Appl. Surf. Sci.*, volume 166:p. 247, 2000. 32

[SKM+98] Sakai, Y.; Kato, M.; Masuda, S.; Harada, Y.; Ichinokawa, T.: In: *Surf. Rev. Lett.*, volume 5:p. 1199, 1998. 21

[SKX+98] Schuster, R.; Kirchner, V.; Xia, X. H.; Bittner, A. M.; Ertl, G.: In: *Phys. Rev. Lett.*, volume 80:p. 5599, 1998. 86

[SPA+98] Stöhr, J.; Padmore, H. A.; Anders, S.; Stammler, T.; Scheinfein, M. R.: In: *Surf. Rev. Lett.*, volume 5:p. 1297, 1998. 20

[SQU] MPMS from Quantum Design, see `http://www.qdusa.com/products/mpms.html`. 17

[SS02] Schneider, Claus M; Schönhense, Gerd: In: *Rep. Prog. Phys.*, volume 65:p. R1785, 2002. 20

[ST01] Sugahara, Satoshi; Tanaka, Masaaki: In: *J. Appl. Phys.*, volume 89:p. 6677, 2001. 32

[STD+99] Schippan, F.; Trampert, A.; Däweritz, L.; Ploog, K. H.; Dennis, B.; Neumann, K. U.; Ziebeck, K. R. A.: In: *J. Cryst. Growth*, volume 201-202:p. 674, 1999. 1, 7

[STDP99] Schippan, F.; Trampert, A.; Däweritz, L.; Ploog, K. H.: In: *J. Vac. Sci. Technol. B*, volume 17:p. 1716, 1999. 1, 4, 7, 55

[STDP00] Schippan, F.; Trampert, A.; Däweritz, L.; Ploog, K. H.: In: *Appl. Phys. Lett.*, volume 76:p. 834, 2000. 1, 7

[SUL+03] Sorop, T. G.; Untiedt, C.; Luis, F.; Kröll, M.; Raşa, M.; de Jongh, L. J.: In: *Phys. Rev. B*, volume 67:p. 014402, 2003. 62

[Tan02] Tanaka, M.: In: *Semicon. Sci. Technol.*, volume 17:p. 327, 2002. 1

[Tes] Digital teslameter FM 2002, `http://www.projekt-elektronik.com`. 14

[THP$^+$94] Tanaka, M.; Harbison, J. P.; Park, M. C.; Park, Y. S.; Shin, T.; Rothberg, G. M.: In: *J. Appl. Phys.*, volume 76:p. 6278, 1994. 1, 4, 7

[Tip] `http://www.spmtips.com/products/cantilevers/datasheets/co-cr/` and `http://www.anfatec.de/special_tips.htm`. 11

[TMR$^+$98] Tromp, R. M.; Mankos, M.; Reuter, M. C.; Ellis, A. W.; Copel, M.: In: *Surf. Rev. Lett.*, volume 5:p. 1189, 1998. 21

[Tra02] Trampert, Achim: In: *Physica E*, volume 13:p. 1119, 2002. 5, 7, 30

[Tro00] Tromp, R. M.: In: *IBM J. Res. Dev.*, volume 44:p. 503, 2000. 21

[TSDP99] Trampert, A.; Schippan, F.; Däweritz, L.; Ploog, K. H.: In: *Inst. Phys. Conf. Ser. No*, volume 164:p. 305, 1999. 5

[TSDP01] Trampert, A.; Schippan, F.; Däweritz, L.; Ploog, K. H.: In: *Appl. Phys. Lett.*, volume 78:p. 2461, 2001. 5, 7

[TWDP04] Takagaki, Yukihiko; Wiebicke, Edith; Däweritz, Lutz; Ploog, Klaus H.: In: *Jpn. J. Appl. Phys.*, volume 43:p. 2791, 2004. 34

[TWH$^+$03] Takagaki, Y.; Wiebicke, E.; Hesjedal, T.; Kostial, H.; Herrmann, C.; Däweritz, L.; Ploog, K. H.: In: *Appl. Phys. Lett.*, volume 83:p. 2895, 2003. 77, 80

[TWM$^+$04] Takagaki, Y.; Wiebicke, E.; Mohanty, J.; Hesjedal, T.; Däweritz, L.; Ploog, K. H.: In: *Physica E*, volume 24:p. 115, 2004. 83, 84

[TWR$^+$03] Takagaki, Y.; Wiebicke, E.; Ramsteiner, M.; Däweritz, L.; Ploog, K. H.: In: *Appl. Phys. A*, volume 76:p. 837, 2003. 53, 77, 83

[WIC$^+$96] Wendel, M.; Irmer, B.; Cortes, J.; Kaiser, R.; Lorenz, H.; Kotthaus, J. P.; Lorke, A.; Williams, E.: In: *Superlattices and Microstructures*, volume 20:p. 349, 1996. 86

[WK64] Wilson, R. H.; Kasper, J. S.: In: *Acta Cryst.*, volume 17:p. 95, 1964. 4

[WR54] Willis, B. T. M.; Rooksby, H. P.: In: *Proc. Phys. Soc. (London) B*, volume 67:p. 290, 1954. 4, 55, 56

[WT01] Wada, H.; Tanabe, Y.: In: *Appl. Phys. Lett.*, volume 79:p. 3302, 2001. 56

[WTSS04] Watanabe, K.; Takemura, Y.; Shimazu, Y.; Shirakashi, J.: In: *Nanotechnology*, volume 15:p. S566, 2004. 86

[ZNG99] Zharnikov, M.; Neuber, M.; Grunze, M.: In: *J. Electr. Spectr. Rel. Phen.*, volume 98-99:p. 25, 1999. 20

1

---

[1] The numbers at the end of each citation denote the pages where the citations occur.

Acknowledgement

This thesis could not have been performed without the support of many people who I would like to thank at this point.

First of all, I would like to thank Prof. Dr. Klaus H. Ploog for giving me the chance to carry out this thesis work. Especially, I would like to thank him for giving me the opportunity to attend conferences and to get to know the magnetic research community, and finally for his comments and suggestions for this manuscript.

I thank Prof. Dr. Kurt R. A. Ziebeck and Prof. Dr. W. Ted Masselink for agreeing to referee my thesis.

I wish to express my profound gratitude to Dr. Thorsten Hesjedal for his help and guidance throughout this work. I will never forget his precise help during the experiments and problems with the scanning probe microscope, which was very crucial for my last important measurements. Besides that, I sincerely thank him for all his humble help for my pleasant stay and so on.

I would like to thank Dr. Lutz Däweritz for his inspiring support throughout this work. I especially thank him for giving me a chance to do XMCDPEEM and LEEM measurements at ELETTRA. I sincerely express my deepest gratitude to him for his comments and suggestions and finally for the careful proofreading of this thesis.

I sincerely thank Dr. Reinhold Koch for many fruitful discussions and for his help in attending schools as well as conferences.

I would like to thank Dr. Yukihiko Takagaki for the etching experiments as well as many interesting discussions. I would also like to thank Dr. Holger Pforte for his help in AFM lithography measurements and Mrs. A. Bluhm for the SEM measurements.

I would like to thank my friend Mr. Roman Engel-Herbert for the MFM simulation. We had very good time together sharing the same office and many more interesting discussions. I enjoyed my stay here and Roman has many, many contributions to many of my good old times. At this point I would also thank his girlfriend Mandy for sharing many great times.

I would like to thank Dr. Daniel Schaadt and Dr. Martin Bowen for many fruitful discussion on magnetism, physics and for sharing many good old Friday evenings.

I would like to thank Prof. Ernst Bauer, Dr. Stefan Heun, Dr. Andrea Locatelli and Dr. Salia Cherifi of Nanospectroscopy beamline facility at ELLETRA for their help during the measurements and the discussion afterwards. I sincerely thank once more Dr. Andrea Locatelli for his help in the data analysis using his macro.

I would like to thank Dr. Denis Kolovos-Vellianitis for many discussions. Especially, I thank him for his help during the shifting of my apartment.

I would like to thank Mrs. Claudia Herrmann, Dr. Martin Kästner and Dr. Li Wan for providing MnAs samples.

I would like to thank Dr. Jens Herfort for his help during SQUID measurements and Dr. Bernd Jenichen for providing X-ray data of the MnAs films.

I would also like to thank Dr. Helmar Kostial, Mr. Werner Seidel, Mrs. Edith Weibicke, Mr. Bernd Drescher, Ms. A. Schönrock and Mrs. Sabine Krauß for their help.

I would like to thank our machine shop people for their strong support for the variable field magnet construction and many other things. In particular, I would like to thank Mr. Jörg Pfeiffer for his help.

I would like to thank our librarians Mrs. D. Dormeyer, Mrs. S. Räther for their help in getting old articles and books. Both of them are very kind, also in cases where I forget to bring back the books.

I sincerely thank Mrs. P. Grasnick for her help for everything starting from my arrival until now. I would like to thank Mrs. Ilka Schuster for the poster printing for the conferences and Mr. Joachim Schönberg for his help with computers.

I thank my Ph.D. colleagues, namely Mr. Tommy Eve, Mr. Fabian Jachmann, Mr. Yue-Jun Sun, Mr. Tian-Yu Liu, Ms. Donghi Hu and finally Dr. Gregor Mußler for many discussions. I enjoyed many discussions during the Ph.D. talks by all my friends and especially the presence of Dr. Oliver Brandt, Dr. Manfred Ramsteiner, Dr. Paulo Santos and Dr. Carsten Hucho.

I would like to thank the former group members Dr. Amal Kumar Das, Dr. Andreas Ney and Dr. Carsten Pampuch for many discussions.

I would like to thank my so called 'Indian connection', Dr. Amal Kumar Das and his family, Dr. Subhabrata Dhar and his family, Mr. Pranob Misra and finally my near and dears Mr. Dillip Kumar Satapathy and Mr. Pranaba Kishor Muduli for giving me extra enjoyment and "truly Indian" excitements.

Finally, I would like to thanks my parents, relatives and friends for their encouragements.

Curriculum Vitae

Name:	Jyoti Ranjan Mohanty
Geburtstag:	20. März 1976
Geburtsort:	Tirtol, Orissa (Indien)

Seit 1.3.2002	Promotionsstudent an der Humboldt-Universität zu Berlin und am Paul-Drude Institut für Festkörperelektronik in der Arbeitsgrupe von Herrn Priv.-Doz. Dr. R. Koch unter Betreuung von Herrn Prof. Dr. K. H. Ploog
11.08.2001	Master of Technology (M.Tech.) Indian Institute of Technology, Delhi, Indien Thema: ”Optimization of silicon nitride and study of Metal-Insulator-Semiconductor (MIS) structure”
01. – 04.2001	Department of Physics, Indian Institute of Technology, Delhi, Indien Project Assistant, Thema: ”Study of I-V characteristics of copper oxide nano-thin film Schottky barriers using different metal electrodes for solar cell applications”, Betreuer: Dr. B. R. Mehta
06.1999 – 12.2001	Studium der Festkörperphysik Indian Institute of Technology, Delhi, Indien
06.1999 – 12.2001	Teaching Assistant Department of Physics, Indian Institute of Technology, Delhi, Indien
03.02.2000	Master of Science (M.Sc.) in Physik Sambalpur University, Orissa, Indien
06.1996 – 04.1998	Studium der Physik Sambalpur University, Orissa, Indien
26.11.1997	Bachelor of Science (B.Sc.) Utkal University, Orissa, Indien
03.1993 – 04.1996	Studium der Physik, Chemie und Mathematik Utkal University, Orissa, Indien

Selbständigkeitserklärung

Hiermit erkläre ich, die vorliegende Arbeit selbständig und nur unter Verwendung der gemäß §6 Absatz (3) angegebenen Hilfen und Hilfsmittel angefertigt zu haben.

Ich habe mich an keiner anderen Universität um einen Doktorgrad beworben und besitze auch keinen entsprechenden Doktorgrad.

Ich erkläre die Kenntnis der dem Verfahren zugrunde liegenden Promotionsordnung der Mathematisch-Naturwissenschaftlichen Fakultät I der Humboldt-Universität zu Berlin.

Jyoti Ranjan Mohanty
18.03.2005